PARTICLE-SCALE MECHANISMS CONTROLLING THE RESPONSE OF GRANULAR AND CLAYEY GEOMATERIALS AT VERY SMALL STRAINS

Arianna Gea Pagano

Thesis submitted to the Department of Civil and Environmental Engineering, University of Strathclyde, Glasgow, in fulfilment of the requirements for the degree of

Doctor of Philosophy

in

Civil and Environmental Engineering

March 2018,

Glasgow, UK

Declaration of authenticity and author's right

This thesis is the result of the author's original research. It has been composed by the author and has not been previously submitted for examination which has led to the award of a degree.

The copyright of this thesis belongs to the author under the terms of the United Kingdom Copyright Acts as qualified by University of Strathclyde Regulation 3.50. Due acknowledgement must always be made of the use of any material contained in, or derived from, this thesis.

Signed:

Date: 29 March 2018

ABSTRACT

Soil stiffness at very small strains is a fundamental parameter for a wide range of geotechnical applications. The correct evaluation of the soil stiffness parameters at very small strains is essential for the realistic prediction of ground deformations occurring around geotechnical structures under operational conditions (serviceability limit state design) and is used to derive the stiffness degradation curve with increasing strain.

The aim of this research is to explore the behaviour of granular and clayey geomaterials at very small strains in cases where the macroscopic response observed experimentally cannot be easily interpreted. In these cases, existing models commonly adopted for the evaluation of the small strain stiffness fail to capture the soil response and may in turn lead to erroneous estimations of ground deformations.

Two examples were analysed in this research. Firstly, the stiffness at very small strains of unsaturated granular materials was investigated. Despite a number of recent studies confirming the dependency of the shear modulus at very small strains on suction and degree of saturation, no existing models are able to capture the different trends of variation observed experimentally. Since this dependency has to be accounted for in the design of infrastructure interacting with the atmosphere, there is scope to investigate the effect of these two variables further.

Secondly, the macroscopic response at very small strains of saturated clayey geomaterials was explored. Studies on the one-dimensional compression of saturated non-active clays demonstrated how the processes occurring at the particle scale may significantly affect the response observed at the macroscale. Since the evaluation of soil responses in terms of the

soil stiffness is generally based on the assumption that soil can be treated as a continuum medium, an attempt was made to take into account the mechanisms occurring at the microscale and their effect on the macroscopic response observed at very small strains.

The thesis goals were achieved by carrying out two separate experimental investigations on unsaturated well-graded sand specimens, and on kaolin clay specimens saturated with different pore-fluids. The shear modulus at very small strains, G_0, was inferred from the measurement of the velocity of propagation of shear waves through the specimens using the bender element technique.

The interpretation of the experimental results was based on the analysis of the micro-mechanisms underlying the macroscopic response. For the case of unsaturated sand, a microscale-based model relating the small strain stiffness with the suction-induced intergranular stress was derived by analysing the stiffness at the contact between sand particles in the presence of water menisci and in the bulk water. The model was successfully validated against the experimental data, and was able to capture the different trends of variation of G_0 along a drying or a wetting path observed in the literature. For the case of saturated clay, a DEM model with newly-designed contact laws (accounting for the mechanical and electro-chemical interactions occurring between clay particles) was first introduced. The DEM model was able to reproduce basic aspects of the macroscopic compression behaviour of kaolin clay specimens at a qualitative level. Then, the results of the DEM simulations and the quantitative analysis of the stiffness of the different particle-to-particle interactions were successfully used to elucidate the microscopic mechanisms affecting the velocity of propagation of shear waves, in turn related to the small strain stiffness.

List of Journal papers:

'A microscale-based model for small-strain stiffness in unsaturated granular geomaterials.' *A.G. Pagano, A. Tarantino, V. Magnanimo* − Submitted for publication to Géotechnique (under revision).

'A DEM investigation of the micromechanics of non-active clays.' *A.G. Pagano, A. Tarantino, T. Weinhart and V. Magnanimo* − Submitted for publication to Géotechnique.

'Micromechanical interpretation of mechanical wave propagation in saturated non-active clay.' *A.G. Pagano, A. Tarantino* − Submitted for publication to Géotechnique.

AKNOWLEDGEMENTS

Firstly, I would like to express my deep gratitude to my supervisor Prof. Alessandro Tarantino for his guidance, advice and support throughout my PhD, and for his enthusiastic attitude towards research. A very special thanks also goes to Dr Vanessa Magnanimo for her kind and constructive support over the last 2 years of my PhD.

I would like to thank Derek McNee and the other technicians for their assistance during my experimental work. I am also grateful to the MSM group at the University of Twente for their support during my stay with them.

My gratitude goes to my examiners, Dr Erdin Ibraim and Dr Stella Pytharouli, who had the patience to read through this thesis and gave me valuable and constructive feedback.

Vorrei ringraziare la mia famiglia per il supporto che mi ha dato in questi anni, da vicino e a distanza. Un ringraziamento speciale va ai miei genitori, Livia e Nicola, e a mia sorella Teresa. La mia casa è dove siete voi.

Grazie agli amici: Giuseppe, Jacopo, Francesca e Milly, per essermi ancora vicini nonostante il tempo (tanto!) e la distanza; Alessia e Brunella, Riccardo, Elena e Carolina, per avermi fatto da seconda famiglia in un posto così lontano da casa.

Thanks to all the other friends among the PhD students and postdocs I met during these years in the Civil & Environmental Engineering Department. A list would be too long, but I still want to thank you all for making the journey much easier.

Finally, a special thanks to Ian for all the joyful, awful and perfectly ordinary moments we have shared over the last 2 and a half years. Thank you for being the person who is always there for me.

TABLE OF CONTENTS

1. BACKGROUND

1.1. LITERATURE REVIEW

1.1.1. Soil stiffness: the engineering problem

The stiffness of a body is defined as the resistance of the body to deformation under applied force (Clayton 2011). Soil stiffness is a fundamental parameter in the study of soil mechanics and its applications to geotechnical design. The prediction of soil response under static and dynamic loading conditions requires the knowledge of the deformation characteristics of the soil, which is in turn dependant on soil stiffness. The correct evaluation of soil stiffness is therefore essential for the efficient design of geotechnical infrastructure.

The parameter commonly used to describe soil stiffness in geotechnical engineering practice is the shear modulus G, relating the shear stress τ with the shear strain γ. It is well known that the shear modulus exhibits a strong non-linear behaviour with the strain level. In particular, G has been widely observed to decrease in a non-linear fashion with increasing shear strain (*Figure 1.1* – Atkinson, 2000). The evolution of the shear modulus with the shear strain, usually referred to as the shear modulus degradation curve, is commonly used for the evaluation of ground deformations around different types of geotechnical structures resulting from soil-structure interactions and mobilisation of structural loads.

The maximum value of the shear modulus, referred to as G_0 or G_{max}, is attained at the onset of shearing. For practical purposes, the parameter G can be considered constant and equal to G_0 in the very small strain range, i.e. below $\gamma=0.001\%$ (Clayton & Heymann 2001,

in Clayton 2011). Within this range, soil can be assumed to exhibit a linear stress-strain behaviour.

The correct evaluation of the shear modulus at very small strains is essential for the efficient design of a number of structures in terms of the serviceability limit state. The deformations induced by loading (or unloading) around well-designed geotechnical structures (e.g. retaining walls, foundations) under operational conditions are generally small, lying between 0.01% and 0.1% (Clayton, 2011) as shown in *Figure 1.2*. Existing methods are able to derive the shear modulus degradation curve starting from the value of small strain stiffness (Hardin & Drnevich, 1972; Matasovic & Vucetic, 1995; Ramberg-Osgood 1944). Therefore, the reliable evaluation of soil stiffness at very small strain levels, together with the factors controlling the evolution of the stiffness with increasing strain, appears to be an essential component of the design phase.
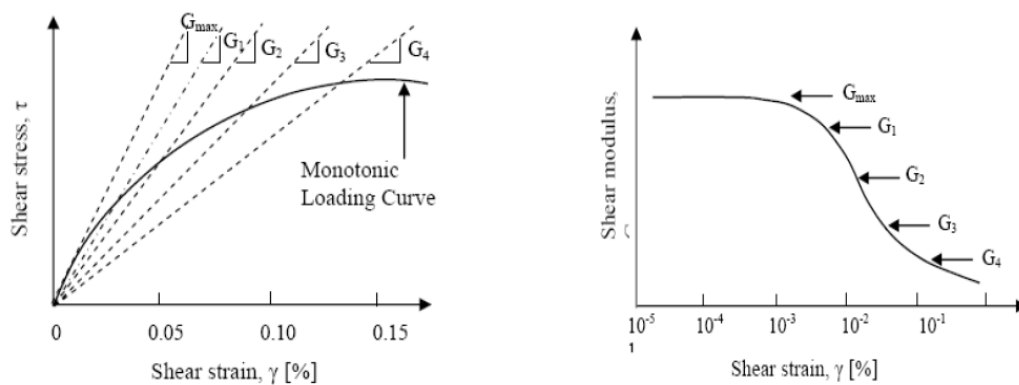
Figure 1.1. Non-linear behaviour of stiffness (Atkinson 2000)
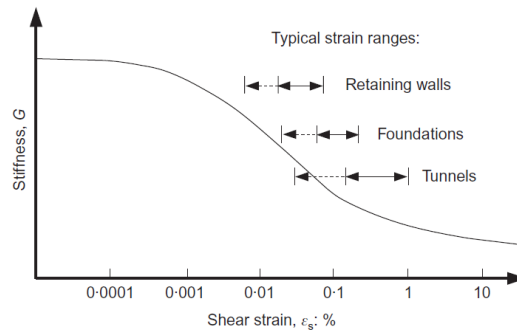
Figure 1.2. Typical stiffness variation and strain ranges for different structures

(redrawn from Mair 1993, in Clayton 2011)

1.1.2. Assessment of soil stiffness at very small strains: general overview

The assessment of soil stiffness at very small strains can be carried out using a number of field and laboratory methods, where static or dynamic measurements of physical quantities are taken in order to infer the shear modulus. Except for the case of static laboratory tests (cyclic triaxial tests with local strain measurement, cyclic simple shear tests and cyclic torsional shear tests), most of the existing field and laboratory techniques are based on the interpretation of mechanical shear wave propagation through the soil. When using these methods, a mechanical wave is transmitted through the soil, generating a dynamic motion in the very small strain range. By identifying the travel time of the shear wave and the corresponding velocity, the shear modulus is calculated.

Two main classes of tests based on the propagation of mechanical waves should be considered:

a) field geophysics, including: continuous surface wave testing (SW), down-hole geophysics (DH), cross-hole geophysics (CH);

b) laboratory methods, including: bender element testing, resonant column testing.

The relative advantages and disadvantages of field and laboratory methods for the evaluation of the shear modulus at very small strains have been well investigated in the past years (e.g. Dyer et al., 1986; Clayton et al., 1995b). For the case of field geophysics techniques, the background noise may significantly affect the interpretation of the travel time arrival. However, these techniques are very effective in determining the geometry and heterogeneity of the ground, and can test large volumes of soil at the current in-situ stress level. For the case of laboratory methods, the background noise may once again affect signal interpretation, and the testing procedures may be extremely time consuming. On the other hand, laboratory tests are carried out under controlled conditions, and can therefore be used to obtain a wider range of parameters than field techniques (Clayton 2011).

The fundamentals of the bender element technique, which is the laboratory method used in this work to assess the velocity of propagation and infer the shear modulus at very small strains, are shortly described in the following section.

1.1.2.1. **Bender element technique**

The bender element method, first developed by Shirley and Hampton (1978), is a simple technique to obtain the shear modulus at very small strains, G_0, by measuring the velocity of propagation of shear waves through soil specimens. The versatility in the installation method of bender element sensors in conventional laboratory apparatuses have led to the wide use of the bender element method in the past years (Yamashita et al., 2009), particularly in the triaxial test apparatus (Clayton 2011, Takkabutr 2006).

The bender element technique is based on the use of double-layer piezoelectric transducers. Piezoelectric materials are capable of converting an electrical signal into a mechanical wave. When subjected to an applied voltage, the two layers deform in different

directions, causing the element to bend. Vice-versa, the layers are able to generate an electric voltage when bent (*Figure 1.3*). Thus, two piezoelectric sensors can be inserted into a soil specimen, with one acting as a source and the other as a receiver of mechanical waves. The direction of polarization of the two layers of a piezoelectric sensor affects the amount of voltage/motion generated by the excitation of the sensor. Two possible configurations may be used: series (or x-poled) configuration, where the directions of polarization of the two layers point in opposite directions and the excitation voltage is applied to the outer electrodes (*Figure 1.4b*); parallel (or y-poled) configuration, where the two piezoelectric layers have the same poling directions and the excitation voltage is applied to the centre metal shim (*Figure 1.4c*). Since the parallel configuration provides twice the motion of the series configuration for the same applied voltage, the x-poled element is commonly used as a receiver and the y-poled element as a source (Lee and Santamarina 2005, Yamashita et al., 2009).
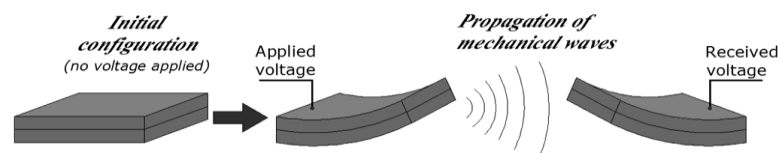
Figure 1.3. Basics of Piezoelectricity
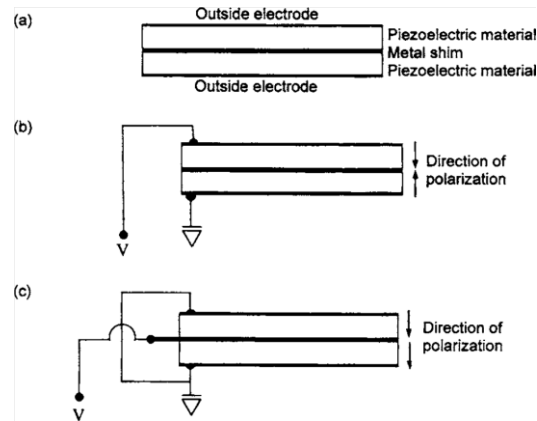
Figure 1.4. Bender elements: a) schematic representation of bender element, b) series type, and c) parallel type (Lee and Santamarina, 2005)

Depending on the type of installation and the resulting mode of deformation induced by the piezoelectric transducer, the velocity of propagation of shear waves (bender elements) or compression waves (extender elements) can be measured (Lings & Greening 2001).

Bender element testing is based on the assumption that at very small strain levels (i.e. within the context of soil's elastic response in terms of the stress-strain relationship) the shear modulus can be determined from the Theory of Elasticity as $G_0 = \rho \, V_s^2$, where ρ is the total density of the soil specimen and V_s is the velocity of the shear wave propagating through the sample. The shear wave velocity value is given by $V_s = L/\Delta t$. The term L represents the travel length, which is usually taken as the tip-to-tip distance between the source and the receiver (Dyvik and Madshus 1985, Viggiani and Atkinson 1995a, Fernandez 2000). The term Δt represents the travel time of the shear wave. The evaluation of the travel time of the wave is somewhat controversial. Different suggestions are presented in the literature dependent upon sensor installation, type of application and used input signals (Dyvik and Madshus 1985, Viggiani and Atkinson 1995a,b; Jovicic and Coop 1997; Santamarina and Fam 1997). However, there is still no agreement regarding the most

reliable method for travel time interpretation. The methodologies proposed over the years for the evaluation of the travel time range from simple methods based on the direct observation of the time interval between characteristic points of the input and output signals, to more complex techniques supported by signal processing and spectrum analyses tools. Existing interpretation techniques can be briefly resumed as follows:

I. Time domain interpretation (*Figure 1.5*): the first arrival is identified from the voltage − vs − time graph of input and output signals. Different approaches can be adopted in the time domain, for instance:

- *Time interval between characteristic points of the input and output signals*: the travel time corresponds to the time distance between two characteristic points in the graphs, e.g. first peak, first deflection, first bump etc (Lee and Santamarina 2005).

- *Cross correlation of the input and output signals*: the first arrival is derived from the cross-correlation function, which is a measure of the degree of correlation of two signals (Viana da Fonseca et al 2009). The peak of the cross-correlation function can be considered as an estimation of the travel time.
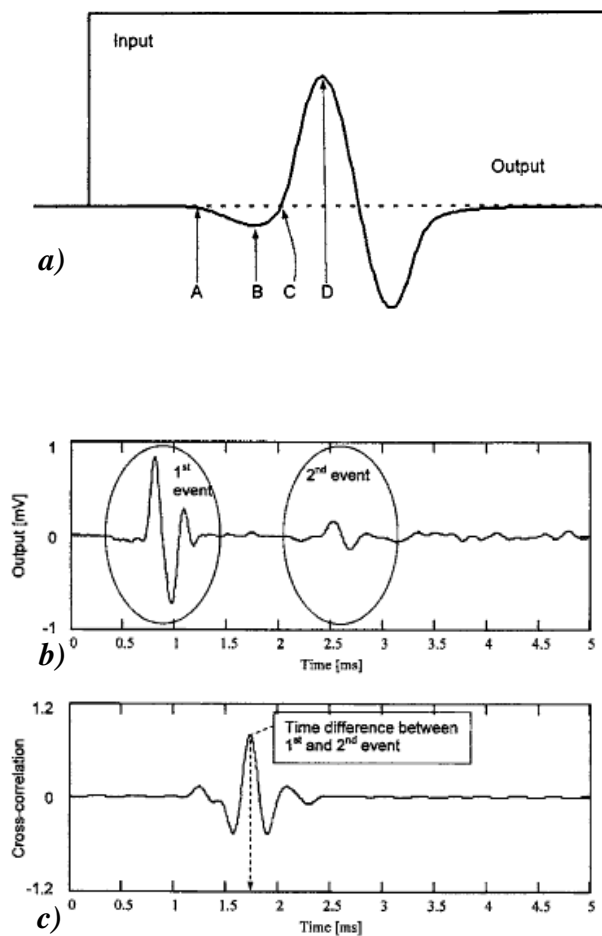
Figure 1.5. Examples of time domain analysis (Lee and Santamarina, 2005): a) time distance between characteristic points (A: first deflection; B: first bump; C: first zero-crossing; D: first main peak); b) output signals corresponding to two separate events (arrival of input wave and reflected wave); c) cross-correlation function the two events in b)

II. Frequency domain interpretation (*Figure 1.6*): the first arrival is identified from the analysis of the voltage – vs – frequency graph of input and output signals and from the coherence function (correspondent to the cross-correlation function in the frequency domain) and the phase shift between the recorded signals (Greening & Nash 2004).
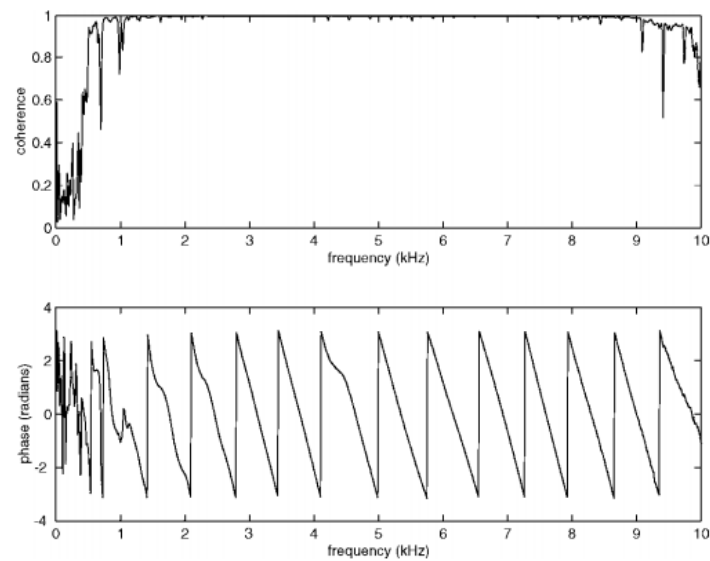
Figure 1.6. Example of coherence and raw phase plot. The arrival time is proportional to the slope of the phase shift-versus-frequency graph (Greening and Nash, 2004)

Another critical aspect of the use of bender elements regards the choice of the waveform and frequency of the input wave in order to guarantee a reliable measurement of the arrival time. Among a number of possible waveforms, the sinusoidal waveform was observed to cause smaller ambiguity in the detection of the arrival time than other types of waveform, such as square-shaped signals (Leong et al. 2005, Viana da Fonseca et al 2009). As regards the wave frequency, the first arrival is in principle not affected by the selected input frequency. However, the choice of the input frequency may significantly affect the ability to detect the first arrival of the wave (Lee and Santamarina, 2005) as the bender element output signal is enhanced when the input frequency is close to the resonant frequency of the bender element-soil system (Lee and Santamarina, 2005, Jovicic et al. 1996; Kawaguchi et al. 2001). Furthermore, the first arrival of the shear wave might be difficult to detect due to the propagation of additional transverse P-waves (so-called 'near-field effect') that may be recorded by the receiver bender element under certain conditions

(Viggiani and Atkinson 1995; Jovicic et al. 1996; Brignoli et al. 1996). Near-field effects can be quantified in terms of the ratio between the travel length of the wave and the wavelength (Sanchez-Salinero et al. 1986). An optimal value of travel length to wavelength ratio for soils has been suggested by Leong et al. (2005) as being at least equal to 3.33. This value is in agreement with Sanchez-Salinero et al. 1986, Arulnathan et al. 1998, Arroyo et al. 2003, and ASTM recommendations (ASTM D 2845, 1997 a).

1.1.3. Small strain stiffness of unsaturated soils

The prediction of soil behaviour and soil-structure interactions for the case of infrastructure interacting with the atmosphere (shallow foundations, road and railway embankments, earth dams, riverbanks etc) is a major challenge. For instance, soils used to construct earth structures are unsaturated during construction and, in several cases, during operational conditions. Their behaviour is thus affected by the simultaneous presence of water and air in the pore spaces, which makes the pore-fluid mixture compressible and influences the stress state (Mancuso et al. 2002).

All the processes linked to the soil-atmosphere interaction may have significant effects on the hydraulic behaviour of shallow soils, in turn affecting soil stiffness. A practical example of the variation of soil stiffness in unsaturated conditions may be observed during the phenomenon of shrinkage induced by evaporation. Evaporation causes the soil to de-saturate, which means that part of the pore space once filled with water becomes gradually filled with air (or with a mixture of air and water vapour). It has been observed that the drying process, which gradually moves from saturated to unsaturated conditions, causes the soil to decrease its volume, i.e. to shrink. It also appears that most of the shrinkage occurs during the early phase of the drying process, when the soil can still be considered

saturated. Shrinkage in the unsaturated phase is much smaller, which is in agreement with the general perception that unsaturated soils have a much higher stiffness than saturated soils. There are several factors influencing shrinkage properties, such as the soil structure, the initial water content, the clay content, the organic matter content, the kind and concentration of the cations in the pore-water, the drying conditions etc. It can be concluded that the deformation occurring in earth structures or soils interacting with shallow geotechnical structures is not only induced by loading under operational conditions, but also by the effects of the soil-atmosphere interactions. Therefore, a better knowledge of the influence of the unsaturated condition is required in order to make realistic predictions of the ground movements.

When the soil is unsaturated, the effect of matric suction and degree of saturation on G_0 for a given net confining pressure has a key role in the interpretation of the mechanisms occurring during hydraulic hysteresis. A large number of experimental investigations have been carried out over the years in order to study the influence of suction and degree of saturation on G_0 using different techniques. Qian et al. (1993) showed the effect that the degree of saturation has on the small-strain shear modulus of unsaturated sands from a dry condition to complete saturation (wetting path) in a resonant column apparatus, obtaining a non-monotonic variation of G_0 with the degree of saturation. Similar results have been reported by other researchers (Marinho et al. 1995; Senthilmurugan and Ilamparuthi 2005; Weidinger et al. 2009). An example of non-monotonic variation of G_0 with suction is shown in *Figure 1.7* (left-hand side). Mancuso et al. (2002) measured G_0 for unsaturated silty sand specimens with increasing suction (drying path only), using a suction-controlled resonant column - torsional shear apparatus. They reported an increase of G_0 at a reducing rate with increasing suction, in a monotonic trend. Asslan and Wuttke (2012) obtained the

small-strain stiffness of unsaturated sand specimens by measuring the velocity of propagation of shear waves (bender element technique) in a specially designed cell using the axis translation technique. They measured a monotonic increase of shear wave velocity with matric suction along a drying path for two values of the net stress. The increase of G_0 with increasing matric suction was also confirmed by other researchers (Picornell & Nazarian 1998, Alramahi et al. 2008), although it has been found that the maximum value of G_0 does not necessarily correspond with the maximum matric suction (i.e., the small strain stiffness does not necessarily vary monotonically with suction).

Other authors investigated the effect of wetting-drying cycles on G_0. Ng et al. (2009) focused on the effect of hydraulic hysteresis under constant isotropic net stress states on the anisotropic small-strain shear modulus of a completely decomposed tuff using a modified triaxial cell equipped with bender elements. The soil appeared to be stiffer during wetting, and exhibited an increase in G_0 with increasing matric suction in a monotonic trend for both drainage and imbibition. The same behaviour during hydraulic hysteresis has been observed by several authors (Khosravi and McCartney 2001; Khosravi et al. 2016; Ng and Xu 2012). An example of the monotonic variation of G_0 with suction is shown in *Figure 1.7* (right-hand side). Contrarily, further experiments on an unsaturated sandy soil using bender elements and axis translation technique showed that G_0 varied in a non-monotonic manner with respect to matric suction, and was observed to be smaller upon wetting (Khosravi et al. 2016).
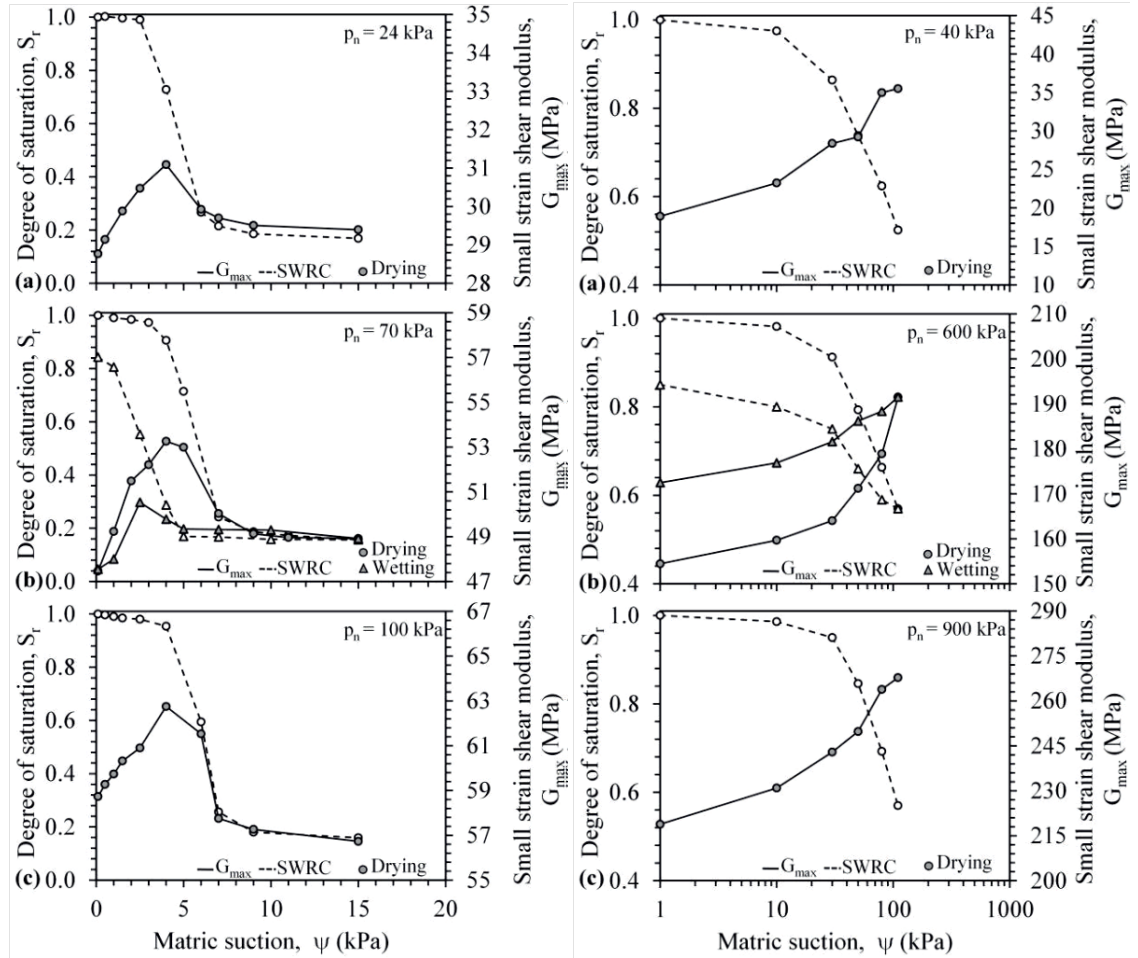
Figure 1.7. Examples of non-monotonic (left-hand side) and monotonic (right-hand side) variation of G_0 (Khosravi et al. 2016)

1.1.3.1.   **Models for G_0 in saturated and unsaturated soils**

A large number of models have been proposed over the past decades in order to predict the small-strain shear modulus of saturated granular and clayey geomaterials. The effects of variables such as confining stress, void ratio, overconsolidation ratio, strain rate etc. for the case of dry and fully saturated soils have been widely investigated by many researchers (Hardin and Richart 1963; Hardin and Black, 1978; Hardin and Drnevich 1972; Hardin 1978; Iwasaki et al. 1978; Viggiani and Atkinson 1995; Stokoe et al. 1995; Rampello et. al. 1997; Sorensen et al. 2010). In such conditions, the macroscale small-strain stiffness is

usually fitted by a power equation form containing empirical functions of the aforementioned variables (e.g. void ratio, e, and effective stress, σ'):

$$G_0 = A\, f(e)(\sigma')^n.$$

More recently, a number of models have been proposed to quantify G_0 for the case of unsaturated soils (Mancuso et al. 2002; Mendoza et al. 2005; Ng et al. 2009; Sawangsuriya et al. 2009; Khosravi et al. 2012; Oh and Vanapalli 2014; Wong et al. 2014; Dong et al. 2016). A common approach adopted by several authors (Oh and Vanapalli 2014; Sawangsuriya et al. 2009) is to derive empirical or semi-empirical relationships of G_0 using the concept of average skeleton stress (Jommi, 2000), starting from the concept of Bishop's effective stress for unsaturated soils (1959). According to Bishop, Terzaghi's effective stress principle can be extended to the case of unsaturated soils by introducing the contribution of the air-water pressure difference $(u_a - u_w)$ as follows:

$$\sigma' = \sigma - u_a + \chi\,(u_a - u_w)$$

where σ' is the effective stress, σ is the total stress, u_a and u_w are the air and water pressure respectively and χ is a soil property directly dependent on the degree of saturation. By substituting the term χ with the degree of saturation, a stress variable for unsaturated soils known as 'average skeleton stress' is obtained.

For instance, the expression of G_0 in unsaturated soils proposed by Sawangsuriya et al. (2009) is the following:

$$G_0 = A\, f(e)[(\sigma - u_a) + S^m(u_a - u_w)]^n$$

where S is the degree of saturation, and m and n are empirical fitting parameters. Similarly, Oh and Vanapalli (2014) proposed the following non-linear relationship for the prediction of G_0 in unsaturated soils:

$$G_0^{uns} = G_0^{sat}[1 + n(u_a - u_w)S^m]$$

where G_0^{uns} and G_0^{sat} are the shear moduli at very small strains in unsaturated and saturated conditions.

In both expressions, the shear modulus at very small strains in unsaturated soils is directly proportional to the product of suction and degree of saturation, which is in agreement with the effective stress for unsaturated soils proposed by Bishop. Using this principle involves the implicit assumption that the 'effective' stress state increases with an increase of degree of saturation, which would theoretically lead to higher values of G_0 along a drying path rather than a wetting path at given suction. Nevertheless, the experimental investigations presented in the previous section carried out on many different types of soils often showed an opposite trend in the variation of G_0 during hydraulic hysteresis, with the soil being significantly stiffer during imbibition rather than during drainage. This evidence shows how the mechanisms underlying the variation of G_0 with changes of matric suction and in degree of saturation are not yet fully understood.

Other proposed models for the evaluation of unsaturated soils (e.g. Dong et al. 2016) are based on the concept of suction stress (Lu & Likos, 2006), which combines the effect of interparticle forces dependent on matric suction and degree of saturation and is intrinsically related to the soil water retention curve:

$$\sigma^s = -S_e(u_a - u_w) = -(S_e/\alpha)\left[S_e^{n/(1-n)} - 1\right]^{1/n}$$

where σ^s is the suction stress, S_e is the effective degree of saturation equal to $(S - S_r)/(1 - S_r)$, and α and n are the empirical fitting parameters in the van Genuchten model (1980). This approach mainly focuses on the effect of suction in the bulk water, but does not account for the effect of suction from the presence of menisci.

It can be concluded that there is no agreement regarding the role of degree of saturation and matric suction on the variation of the small strain shear modulus of unsaturated soils. The majority of the existing models fail to predict the macroscopic response at very small strains of unsaturated soils, even at a qualitative level.

1.1.4. The micromechanical approach

In the classical approach for the study of the macroscopic response of geomaterials, soil is generally treated as a continuum medium, with constitutive relations based on the theory of Continuum Mechanics. However, due to the discrete nature of granular geomaterials (e.g. sands) and clayey geomaterials, an understanding of the processes occurring at the particle scale can represent a useful tool for the correct interpretation and prediction of soil behaviour at the macroscale. Thus, a micromechanical approach may be conveniently adopted when studying the response of such materials. The main objective of the micromechanical approach is to predict the macroscopic response of particle aggregates and their constitutive relationships (e.g. the relationship between the macroscopic stress tensor and strain tensor) based on the microscopic constitutive relationship (relating the forces developing at the contacts between particles with the relative displacement at the contact point) by using suitable averaging techniques. The micromechanical approach can be applied analytically and numerically. Numerical micromechanical analyses are mainly performed using the Discrete Element Method.

1.1.4.1. Discrete Element Method

The Discrete Element Method (DEM) or Discrete Particle Method (DPM), first proposed by Cundall and Strack (1979), is a powerful numerical technique that has been successfully

used in the past decades for achieving a better understanding of the macroscopic response of discrete materials, as well as for predicting their behaviour by starting from the microscopic information at the particle scale. DEM has been proven to accurately capture the macroscale response of granular materials, and can therefore be used as a virtual laboratory to investigate fundamental aspects of the behaviour of granular materials (O'Sullivan et al., 2006). Many examples can be found in the literature regarding the application of the DEM to industrial processes, including the flow of granular particles in hoppers (Langston et al. 2004), centrifugal mill charge motion and granular flow in mixing processes (Cleary & Hoyer, 2000), underground excavation processes (Labra et al., 2008) and so on. DEM applications to geotechnical and geomechanical problems include strain localisation (Kawamoto et al., 2017; Iwashita & Oda, 1997), soil particle crushing (Thornton et al., 1996 ; Cheng et al. 2003; Bolton et al., 2008), stress-induced anisotropy (Guo & Zhao, 2012), wave propagation (Mouraille, 2009; O'Donovan & O'Sullivan, 2012) etc.

In DEM models, the components of the motion of each particle in a given particle assembly is derived from the forces acting on the particle using Newton's second law for the translational motion and Euler's equations for the rotational motion. In 3-D space, the following equations describe the translation and the rigid rotation of a spherical particle of mass m respectively:

$$\begin{cases} F_1 = m(\ddot{x}_1 - g_1) \\ F_2 = m(\ddot{x}_2 - g_2) \\ F_3 = m(\ddot{x}_3 - g_3) \end{cases}, \quad \begin{cases} M_1 = I_1\ddot{\omega}_1 \\ M_2 = I_2\ddot{\omega}_2 \\ M_3 = I_3\ddot{\omega}_3 \end{cases}$$

where F_i is the force applied in the i-direction, $\ddot{x}_i$ is the linear acceleration of the particle in the i-direction, g is the acceleration of gravity, M_i is the moment of the particle in the i-

direction, I_i is the moment of inertia of the particle in the i-direction, and $\ddot{\omega}_i$ is the angular acceleration of the particle in the i-direction. The dynamic motion of each particle is determined by identifying the values of F_i and M_i acting on the particle at each time step, and then calculating the resulting positions, velocities and rotations by time-integrating the linear and angular acceleration appearing in Newton's and Euler's laws. The time integration is performed by implementing a finite-difference approach in the DEM code. The most common time-integration algorithm implemented in DEM codes is the Verlet explicit integration. The velocity-Verlet algorithm is implemented in the DEM code used in this study (MercuryDPM, www.mercurydpm.org).

1.1.4.2. Contact laws for DEM in granular materials

The resultant forces and moments acting on each particle at each time step are derived by implementing constitutive relations in the DEM code, commonly referred to as force-displacement laws at the contact (Cundall and Strack, 1979), or contact laws. Contact laws link the force (/moment) developing at the contact between two particles with the relative translation (/rotation) associated with that force (/moment). Linear and non-linear contact laws can be selected. Linear contact laws are easy to implement and result in efficient computational times. However, there are cases where linear contact laws are not suitable due to the non-linearity of the real behaviour of grains interacting with each other. In these cases, the use of non-linear contact laws in DEM codes enables the user to better capture/reproduce the behaviour of granular materials, at the cost of a significantly increased computational burden.

A contact force F developing between a particle i and a particle j can be decomposed in its normal component and tangential component, F_n^{ij} and F_t^{ij} respectively. For the case of linear contact laws, these forces can be calculated as:

$$F_n^{ij} = \begin{cases} 0, & \delta_{ij}^n \leq 0 \\ k_n \delta_{ij}^n, & \delta_{ij}^n > 0 \end{cases}, \quad \text{and} \quad \Delta F_t^{ij} = \begin{cases} 0, & \delta_{ij}^n \leq 0 \\ k_t \Delta \delta_{ij}^t, & \delta_{ij}^n > 0 \\ \mu f_{ij}^n, & |k_t \Delta \delta_{ij}^t| > \mu f_{ij}^n \end{cases}$$

where δ_{ij}^n is the normal overlap between particle i and particle j taken on the line connecting the centres of the spheres, k_n is the normal stiffness at the contact, k_t is the tangential stiffness at the contact, δ_{ij}^t is the tangential overlap, and μ is the friction coefficient. For the case of non-linear contact laws, the Hertzian contact model for the calculation of normal contact forces is widely used:

$$F_n^{ij} = \begin{cases} 0, & \delta_{ij}^n \leq 0 \\ \dfrac{4}{3} E^* r^{1/2} \delta_{ij}^{n\ 3/2}, & \delta_{ij}^n > 0 \end{cases}$$

where E^* is the equivalent Young modulus of the particles, and r is the equivalent radius. The extension of the Hertzian theory to the case of tangential contact forces can be found in Mindlin (1949).

When tangential contact forces are applied, particle rotations occur and a moment is developed at the contact. Two types of rotations may develop following the application of a tangential force: a rotation about axes belonging to the contact plane (usually referred to as rolling) and a rotation about the normal at the contact (referred to as torsion or spin). The rolling moment M_r^{ij} and torsion moment M_{to}^{ij} can be calculated as follows:

$$\Delta M_r^{ij} = \begin{cases} 0, & \Delta F_t^{ij} = 0 \\ k_r \Delta \omega_{ij}^r, & \Delta F_t^{ij} \neq 0 \end{cases}, \quad \text{and} \quad \Delta M_{to}^{ij} = \begin{cases} 0, & \Delta F_t^{ij} = 0 \\ k_{to} \Delta \omega_{ij}^{to}, & \Delta F_t^{ij} \neq 0 \end{cases}$$

where k_r is the rolling stiffness at the contact, k_{to} is the torsional stiffness at the contact, ω_{ij}^r is the rolling angle, and ω_{ij}^{to} is the torsional angle.

Additional components of the contact laws accounting for the energy loss at the contact are represented by damping coefficients, proportional to the particle velocity.

1.1.4.3. **DEM simulation of non-contact forces**

Although traditional contact models only account for the mechanical interaction developing between particles in contact, some attempts have been made in the past years to include other types of interactions occurring between particles not yet in contact. Van der Waals cohesion between small dry particles (diameters ranging from 1 to 100 µm), wet cohesion due to the formation of liquid bridges between particles, sinter bridges etc have been simulated in DEM models by adding attractive forces to the contact laws, developing at negative values of the particle overlap (Luding 2008, Willett et al. 2000, Roy et al. 2016). This approach is relevant for industrial applications to simulate the response of wet and dry powders.

However, there are other cases where the simulation of non-contact forces is crucial to capture the macroscopic behaviour. For the case of clayey materials, inter-particle forces are both mechanical and electro-chemical in nature, in contrast to the conventional mechanical interactions that characterise granular materials. The relevant role of electro-chemical interactions in clayey geomaterials, including double-layer repulsive interactions, is well established (Bolt, 1956; Olson & Mesri, 1970; Moore & Mitchell, 1974).

The use of DEM models to simulate the response of clayey geomaterials has been very little explored in the literature. A major contribution to the DEM modelling of clays has been given by Anandarajah and his co-workers (Anandarajah, 1997; Anandarajah & Chen, 1997; Anandarajah, 2000; Yao & Anandarajah, 2003; Anandarajah & Amarasinghe, 2012). The authors developed rational methods for computing the double-layer repulsive force and the van der Waals attractive force occurring between arbitrarily oriented rectangular (2D) or cuboid (3D) elements. By adding these contributions to the conventional mechanical inter-particle interaction, they obtained numerical results that compared reasonably well with the soil behaviour observed in the laboratory. In the DEM analysis, Anandarajah and co-workers assumed that particles possess a uniform negative charge, and that attraction between particles is driven by the short-range van der Waals force only. A criticism to this assumption is that interparticle force-displacement constitutive laws are built on a purely theoretical basis, with no direct experimental evidence of their validity at the microscale. Furthermore, the 'activation' of van der Waals forces is difficult to justify for the average inter-particle distances occurring in natural clays. There is, therefore, a need to design and implement new contact laws able to reproduce accurately the interaction between clay particles.

1.1.5. Micromechanical analysis of small strain stiffness and wave propagation

An example of the successful application of the micro-mechanical approach and micro-macro transition concerns the study of the elastic moduli and mechanisms of wave propagation in granular assemblies. The stiffness parameters of particle assemblies have been derived analytically and numerically (the latter using DEM simulations) for the case of ordered or random packings under different conditions (Kruyt, 2010; Liao & Chang,

1997; Luding, 2005; Mouraille, 2009; O'Donovan & O'Sullivan, 2012; O'Donovan, et al., 2016). In both cases the influence of macroscopic state variables largely investigated experimentally, e.g. confining pressure and void ratio (Hardin & Richart, 1963; Hardin, 1978; Iwasaki & Tatsuoka, 1977; Prange, 1981; Kokusho & Esashi, 1981), was successfully reproduced by changing particle arrangements at the micro-scale, thus proving the suitability of the micro-macro approach for the case of granular geomaterials.

The analytical evaluation of the stiffness tensor can be carried out by applying different averaging techniques. An example is given by Luding (2005) who derived the expression of the stress and stiffness tensors of a an assembly of equal spherical particles using the particle-in-volume averaging technique. The macroscopic tensors were first derived by pre-averaging over single particle contacts, and then calculated an average over all the pairs of particles interacting within an averaging volume V. The expressions of the stress and the elastic strain (and, hence, stiffness) for a single contact were derived from the principles of virtual displacements and virtual stress-change respectively. Once the tensor elements based on single contacts were known, the overall macroscopic variables could be obtained. The following expressions were obtained:

$$\sigma_{\alpha\beta} = \frac{1}{V} \sum_{p \in V} \sum_{c=1}^{Z} l_{\alpha}^c f_{\beta}^c$$

$$C_{\alpha\beta\gamma\phi} = \frac{1}{V} \sum_{p \in V} \left(k_n \, (l^2/2) \sum_{c=1}^{Z} n_{\alpha}^c n_{\beta}^c n_{\gamma}^c n_{\phi}^c + k_t \, (l^2/2) \sum_{c=1}^{Z} n_{\alpha}^c t_{\beta}^c n_{\gamma}^c t_{\phi}^c \right)$$

where σ and C are the stress and stiffness tensors respectively, Z is the total number of contacts contained in the averaging volume, l is the branch vector connecting the centres of particles in contact, f is the interparticle force generated at contact, k_n and k_t are the

normal and tangential spring constant respectively, α, β, γ, ϕ are subscripts that can indicate the directions x, y and z, n and t are the normal and tangential unit vector components respectively and the apex c indicates the single contacts within V. The expression of the stiffness tensor only holds for small deformations, in the absence of opening or closing of contacts or particle rearrangements. If all the terms of the equations are known, the stiffness tensor can be used to calculate the small-strain shear modulus of soil. Similar results had been derived previously in the literature with different nomenclature (Liao and Chang 1997; Kruyt and Rothenburg 1998). Other examples of derivation of the elastic moduli based on the effective medium theory (the system is assumed to be homogeneous, isotropic, and made of equal spheres) are given by Duffy & Mindlin (1957), Santamarina & Cascante (1996) for regular assemblies, and by Digby (1981), Walton (1987), Chang & Liao (1994) for random assemblies.

When the elastic moduli of granular assemblies are derived numerically, two different approaches to the prediction of the elastic moduli via micromechanical analyses may be found in the literature: a dynamic approach and a static approach. The dynamic approach is generally adopted when studying the mechanisms of wave propagation through granular assemblies. Wave propagation is induced in virtual granular specimens by assigning a certain displacement to a particle (or a layer of particles), simulating the input pulse applied to a transmitter bender element in experimental studies. By recording the displacements occurring in the assembly induced by the input motion (or, equally, by monitoring the variation of macroscopic variables such as the stress level during the propagation of the virtual wave), an 'output' signal is obtained and can be used to derive the velocity of propagation of the wave. The small strain stiffness of the assemblies can in turn be derived from the velocity of propagation. This approach has been adopted by

several authors for the case of regular assemblies (e.g. Mouraille et al. 2006, O'Donovan & O'Sullivan, 2012), and random assemblies (e.g. O'Donovan, et al., 2016).

On the other hand, a static approach may be adopted for the evaluation of the elastic moduli of regular and random assemblies. In this case, virtual granular specimens are subjected to incremental deformation. The response of the assembly in terms of the macroscopic stress derived by averaging techniques is recorded, and the corresponding elastic modulus is calculated. Examples of the application of the static approach can be found in Kruyt & Rothenburg (1998), Makse et al. (2004), Magnanimo et al. (2008).

1.2. OBJECTIVES

The aim of this thesis is to explore the behaviour of granular and clayey geomaterials at very small strains in cases where the macroscopic response observed experimentally cannot be easily interpreted. In these cases, existing models adopted for the evaluation of the small strain stiffness may fail to adequately capture the soil response. Therefore, this work aims at providing appropriate tools for the interpretation of and, where applicable, the simulation of such responses on the basis of the processes occurring at the particle scale. This will be achieved by applying experimental, numerical and theoretical approaches.

The main goals are:

1. Develop a micro-scale based model able to link the very small strain stiffness G_0 of unsaturated granular materials observed experimentally to the varying intergranular stress during drying-wetting cycles via the stiffness at the interparticle contact.

2. Develop a DEM framework (based upon the results of indirect experimental observations) suitable for the simulation of clayey geomaterials, that takes into account the presence of both mechanical and electro-chemical interactions between clay particles.

3. Provide a micromechanical interpretation of the phenomena occurring at the particle scale during the propagation of mechanical shear waves in dry and saturated clay observed experimentally, based upon the results of the DEM simulations.

1.3. THESIS OUTLINE

After providing a general overview of the research background and objectives (**Chapter 1**), the thesis is structured as follows:

Chapter 2 first presents an experimental investigation on the effect of suction and degree of saturation on the small strain stiffness of a well-graded sand specimen during drying-wetting cycles (unsaturated conditions). The techniques to perform drying and wetting paths and to derive the shear modulus at very small strain G_0 are described in detail, and the results of the experimental investigation are presented. Then, a micro-scale based model is derived in order to relate the soil parameter G_0 to the varying soil stress state induced by drying-wetting cycles, via the (microscopic) stiffness at the contact. Finally, the results of the model are presented: the model is able to capture the macroscopic response observed experimentally, and to elucidate the mechanisms behind different responses observed in the literature.

Chapter 3 presents a new DEM framework suitable for the simulation of clay particles. The core of the framework is represented by the contact laws, inferred from indirect experimental evidence at the microscale regarding the mechanical and electro-chemical interaction between clay particles. A validation of the DEM framework is then presented in the chapter. The contact laws are successfully probed against their ability to reproduce qualitatively the compression behaviour of clay observed experimentally, including the effect of different pore-fluid chemistries (pH and dielectric permittivity).

Once a suitable DEM framework for the simulation of clay particles was derived, the macroscopic behaviour of clay was further investigated by looking at the response at very small strains. Consequently, **Chapter 4** presents an experimental investigation of the

propagation of mechanical shear waves in kaolin clay specimens with different pore-fluid chemistry. The results of one-dimensional compression tests in an oedometer-like apparatus equipped with bender elements are shown. The experimental evidence is then interpreted by considering i) the different 'stiffness' of mechanical and electro-chemical interactions and ii) the mechanical and electro-chemical force chains as inferred from the DEM simulations presented in **Chapter 3**. The micromechanical interpretation is able to elucidate the microscopic mechanisms responsible for the non-intuitive experimental evidence. In the light of the micromechanical interpretation of the experimental data, the value of soil density used for the calculation of G_0 from the velocity of propagation of shear waves is then discussed, and an 'effective' soil density is proposed.

Additional details regarding the step-by-step procedure for the preparation and installation of the bender element sensors used in this study, together with the results of a number of preliminary DEM simulations carried out using the newly-designed contact laws are given in **Appendix A** and **B**.

2. A MICROSCALE-BASED MODEL FOR SMALL-STRAIN STIFFNESS IN UNSATURATED GRANULAR GEOMATERIALS

Submitted for publication to Géotechnique – Under revision

Arianna Gea Pagano*, Alessandro Tarantino**, and Vanessa

Magnanimo***

POSITION AND AFFILIATION:
* PhD student, Department of Civil and Environmental Engineering, University of Strathclyde
** Professor, Department of Civil and Environmental Engineering, University of Strathclyde
*** Assistant Professor, Multiscale Mechanics Group, University of Twente

ABSTRACT

Stiffness at very small strains G_0 is commonly assessed via laboratory and field methods and used to design a wide range of infrastructure. When stiffness is inferred from field measurements, its value depends on the state of saturation at the time of the measurement and models are needed to infer soil stiffness for varying degree of saturation. When stiffness is measured on saturated specimens in the laboratory, models are needed to extrapolate the laboratory 'saturated' stiffness to the field 'unsaturated' stiffness. This paper presents an experimental investigation of G_0 of unsaturated sand using the hanging water column method and the bender element technique. Experimental results revealed that wave propagation velocity and, hence, stiffness is not controlled by the product 'suction times the degree of saturation'. A microscale-based model was formulated to interpret the experimental results, and to elucidate the mechanisms behind different patterns of G_0 in unsaturated materials observed in the literature. According to the proposed model, the

evolution of G_0 is controlled by the evolution of the suction-generated intergranular stress during drying-wetting cycles. In particular, the breadth of the water retention curve and the magnitude of the intergranular stress due to the presence of the menisci were found to be responsible for the different trends of variation of G_0 during hydraulic hysteresis.

2.1. INTRODUCTION

The shear modulus of soil at very small strain levels (less than 0.001%), typically denoted as G_0, is a soil stiffness parameter commonly assessed via laboratory and field methods. It is a fundamental parameter for a wide range of geotechnical problems and it is used for the prediction of soil response under both static and dynamic loading conditions. For shallow geotechnical infrastructure interacting with the atmosphere, the unsaturated condition of the soil should be taken into account in both the interpretation of field measurements and the selection of design stiffness parameters. When stiffness is inferred from field measurements involving shallow unsaturated layers, its value depends on the state of saturation at the time of the measurement. Since the state of saturation may change over time, the variation of stiffness with degree of saturation should be predicted in order to analyse the geotechnical structure over a realistic range of scenarios. On the other hand, when stiffness is inferred from laboratory measurements on saturated specimens, models are needed to extrapolate the 'saturated' laboratory stiffness to the 'unsaturated' stiffness in the field.

For the case of small-strain shear modulus of soil in saturated state, a large number of models have been proposed over the past decades. The effect of variables such as confining stress, void ratio, overconsolidation ratio, and strain rate have been widely

investigated (Hardin & Richart, 1963; Hardin & Black, 1968; Hardin & Drnevich, 1972; Hardin, 1978; Iwasaki, et al., 1978; Viggiani & Atkinson, 1995a; Stokoe, et al., 1995; Rampello, et al., 1997; Sorensen, et al., 2010). Under saturated conditions, the macroscale small-strain stiffness is usually fitted by empirical power functions of the aforementioned variables.

For the case of small-strain shear modulus of soils in unsaturated state, a number of models have recently been proposed to quantify the small-strain shear modulus over a wide range of degrees of saturation (Mancuso, et al., 2002; Mendoza, et al., 2005; Ng, et al., 2009; Sawangsuriya, et al., 2009; Khosravi & McCartney, 2012; Oh & Vanapalli, 2014; Wong, et al., 2014; Dong & Lu, 2016). G_0 is recognised to be affected by both suction and degree of saturation, which may vary independently because of hydraulic hysteresis and the void-ratio's dependency on water retention behaviour. A key question is how these two variables control the small strain stiffness and whether they can be combined into a single variable.

A common approach adopted by several authors (Oh & Vanapalli, 2014; Khosravi & McCartney, 2012; Sawangsuriya, et al., 2009) is to derive empirical or semi-empirical relationships of G_0 using as a stress variable the product between suction and degree of saturation (Jommi, 2000), often referred to as Bishop's effective stress for unsaturated soils:

$$\sigma'' = \sigma - u_a + S_r\,(u_a - u_w) \qquad\qquad\qquad 1$$

where σ is the total stress, u_a and u_w are the air and water pressure respectively, and S_r is the degree of saturation.

An implicit assumption in this approach is that, at the same suction, the product 'suction times degree of saturation' increases with an increase in degree of saturation. Since the degree of saturation along a drying path is higher than the degree of saturation along a wetting path, one would expect the values of G_0 to be higher along a drying path rather than a wetting path. Although an evidence of this has been observed experimentally (Khosravi, et al., 2016), a number of experimental investigations show an opposite trend, i.e. the soil is observed to be significantly stiffer along a wetting path rather than a drying path (Khosravi & McCartney, 2011; Ng, et al., 2009; Ng & Xu, 2012).

Inspection of experimental data also reveals that the change of G_0 with suction or degree of saturation occurs in either a monotonic or non-monotonic fashion. Qian, et al. (1993) showed the effect of degree of saturation on the small-strain shear modulus of unsaturated sands from a dry condition to complete saturation (wetting path only) in a resonant column apparatus, obtaining a non-monotonic variation of G_0 with degree of saturation. Similar results have been confirmed by other researchers (Marinho, et al., 1995; Senthilmurugan & Ilamparuthi, 2005; Weidinger, et al., 2009). Data presented by Khosravi et al. (2016) seem to suggest that this type of response is linked to the stiffness behaviour along a water retention hysteresis loop. When G_0 increases monotonically with suction, stiffness appears to be higher along a wetting path. On the other hand, when G_0 varies non-monotonically with suction, stiffness appears to be lower along a wetting path. Ideally, a stiffness model should be capable of capturing the interplay between these two aspects. However, no models presented so far are capable of addressing this coupling.

This paper first presents an experimental investigation of the independent effect of suction and degree of saturation on G_0. Unsaturated sand specimens were tested using a

modified triaxial cell apparatus equipped with bender elements. The hanging water column method was used to explore the soil stiffness behaviour along a water retention hysteresis loop. A conceptually simple microscale-based model is then proposed in order to interpret and predict the evolution of G_0 during hydraulic hysteresis. Finally, the proposed model is shown to be able to elucidate a range of responses observed in the literature.

2.2. MATERIALS AND METHODS

2.2.1. Testing materials

The testing material used was a well-graded sand obtained by mixing different fine, medium and coarse grained sands. To obtain a well-graded grain size distribution (GSD), the mixture was prepared according to a modified Fuller equation:

$$P = \frac{\sqrt{\frac{D}{D_{100}}} - \sqrt{\frac{D_0}{D_{100}}}}{1 - \sqrt{\frac{D_0}{D_{100}}}} \times 100 \qquad\qquad 2$$

where P is the passing percentage, D is the anticipated sieve size, D_{100} is the sieve size corresponding to a passing percentage of 100 % and D_0 is the sieve size corresponding to a passing percentage of 0%. *Figure 2.1* shows the GSD of the tested specimen.

The well-graded GSD allowed the desaturation process to be gradual, resulting in a smooth water retention curve. In addition, differences in the degree of saturation between the top and the bottom of the specimen could be minimised. The physical properties of the soil specimen are shown in *Table 2.1*.

To prepare the high air-entry filter at the bottom of the specimen (required to control suction using the hanging water column method), a silty, crushed quartz stone known by the commercial name of Silica (mean particle size of 25.2 μm) was used. The physical properties of the Silica filter are summarized in *Table 2.2*. The amount of silt used to prepare the slurry (98 g) was calculated in order to obtain a 10 mm thick filter.
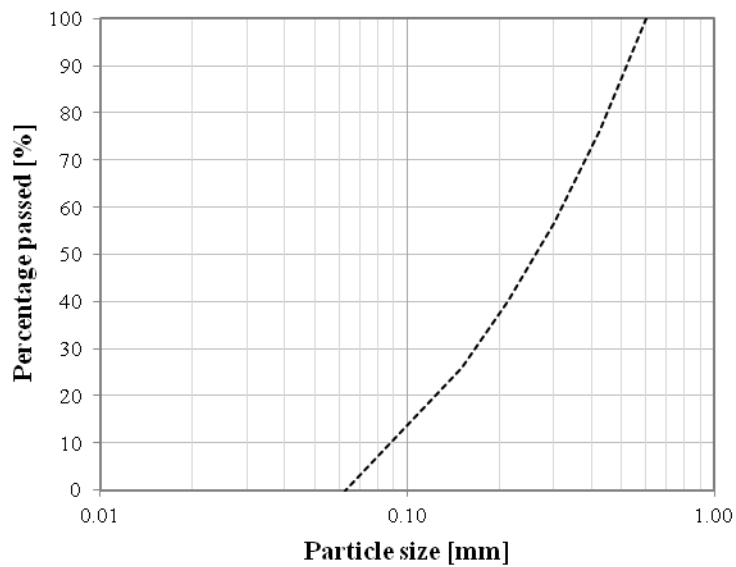
Figure 2.1. Grain size distribution of the soil specimen

Specimen		
Height, h	12.5	cm
Diameter, D	10.0	cm
Total volume, V_{tot}	977.8	cm^3
Specific gravity, G_s	2.63	-
Dry density, ρ	1.59	g/cm^3
Void ratio, e	0.49	-
Porosity, n	0.33	-
Dry mass, M_d	1554.3	g

Table 2.1. Physical properties of the soil specimen

Silt filter		
Height, h	1.0	cm
Diameter, D	10.0	cm
Total volume, V_{tot}	78.5	cm^3
Specific gravity, G_s	2.70	-
Dry density, ρ	1.25	g/cm^3
Void ratio, e	1.16	-
Porosity, n	0.54	-
Dry mass, M_d	98.0	g

Table 2.2. Physical properties of the silt filter

2.2.2. Laboratory equipment

A triaxial test apparatus was modified for testing soil specimens under saturated and unsaturated conditions and measuring the velocity of propagation of mechanical shear waves (bender element technique). A schematic layout of the equipment is shown in *Figure 2.2*.

The specimen was tested along a full water retention hysteresis loop under constant isotropic confining stress. Cell pressure was controlled via a device that allows the water pressure in the cell to be maintained while also measuring the water volume changes occurring in the cell (P/V controller 1 in *Figure 2.2a*). Pore-water pressure inside the specimen was controlled and measured in two different ways depending on whether the specimen was tested under saturated or quasi-saturated/unsaturated conditions.

In the former case, the base pedestal was connected to a second pressure/volume controller device (P/V controller 2 in *Figure 2.2a*) used to impose the pore-water pressure. In the latter case, the base pedestal was connected to a height-adjustable water reservoir, with the water mass exchanged with the specimen continuously monitored using a balance (*Figure 2.2a*). Positive/negative pore-water pressure was imposed by adjusting the height

of the reservoir. Water evaporation from the reservoir was determined by monitoring an identical water reservoir placed on a second balance.

The bender element technique (Shirley and Hampton, 1977) was used to obtain the small-strain shear modulus by measuring the velocity of propagation of shear waves through the specimen. The top cap and base pedestal were modified in order to accommodate a pair of specially manufactured piezoelectric transducers for transmission and measurement of P-waves (compression discs – not used in this study) and S-waves (bender elements). A detailed scheme of the manufactured top cap and pedestal is shown in *Figure 2.2b*. A computer-controlled function generator and oscilloscope allowed the input signal to be sent and both input and output signals to be recorded respectively. Two types of double-layered piezoceramic elements were used for the construction of the sensors: a BIMS-N-PZT5A4-HT x-poled element and a BIMP-N-PZT5A4-HT y-poled element (Morgan Technical Ceramics). Since the parallel configuration provides twice the motion of the series configuration for the same applied voltage, the x-poled element was used as receiver and the y-poled element was used as source. The series-type bender element was shielded with conductive paint and grounded in order to prevent crosstalk effects (Lee & Santamarina, 2005).
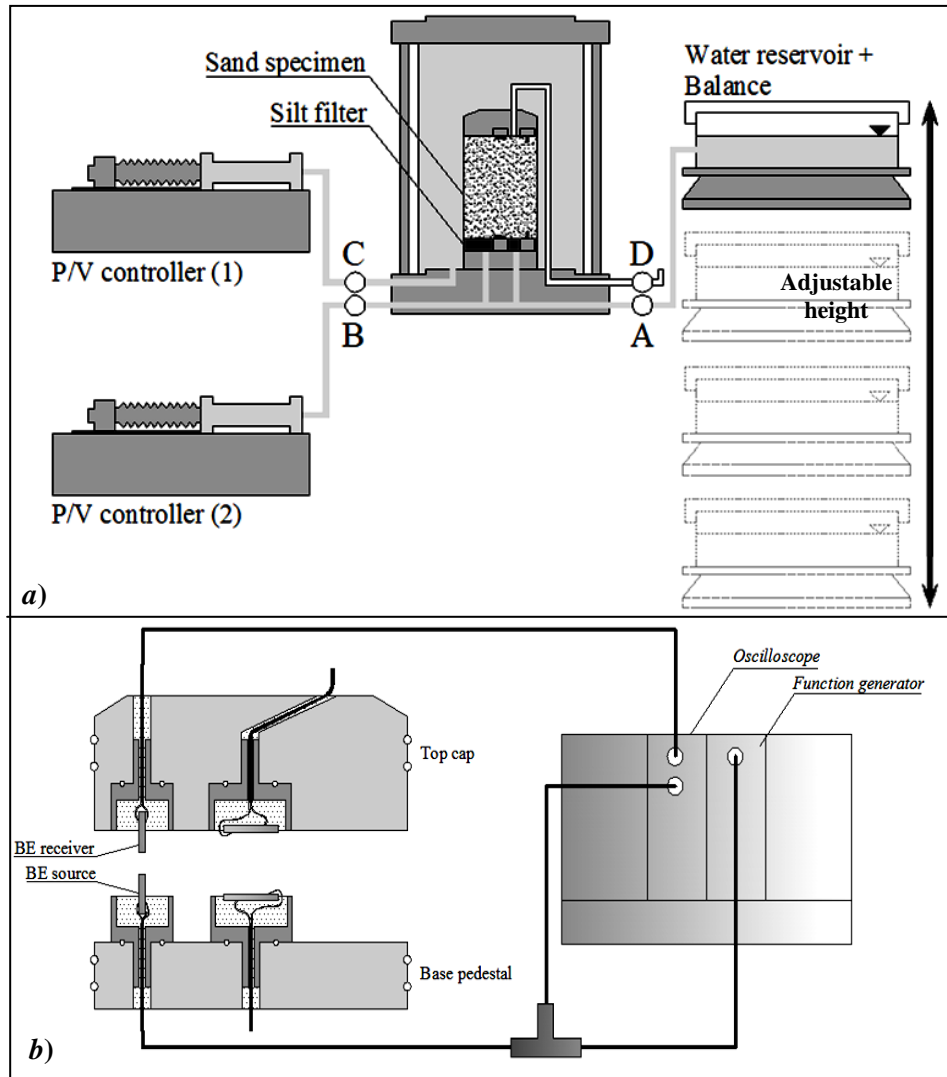
Figure 2.2. Schematic layout of the laboratory equipment: a) triaxial cell with measurement and control of pore water pressure and cell pressure and b) modified top cap and base pedestal equipped with bender elements

2.2.3. Testing procedure

Stage 1 – High air-entry filter preparation

A high air-entry filter was formed on the pedestal by consolidating a silt layer. The silt layer allows the transmission of the negative pore-water pressure to the specimen while preventing the ingress of air into the water drainage system. Furthermore, it prevents the

development of large pores at the specimen/filter interface which is likely to occur in coarse-grained materials (so called "wall effect").

A filter paper disc was first placed on the base pedestal and a latex membrane was placed around the pedestal and fixed with two O-rings. A split mould was assembled around the pedestal, the membrane stretched to the top of the mould and held open by applying a small vacuum. A silt slurry with a water content of around 500% was then gently poured into the mould and allowed to settle for 48 hours. After sedimentation occurred, excess clear water was drained out of the mould by connecting the hydraulic drainage to the water reservoir (valve B closed, valve A open in *Figure 2.2a*) and adjusting the water reservoir height until its water level was one or two millimetres above the top of the silt surface. The filter paper between the filter and the pedestal prevented silt loss through the hydraulic channels during drainage.

Once all the excess water was drained out of the mould, the filter was consolidated by applying suction via the hanging water column method. The water reservoir was lowered in steps, inducing a water flow from the silt filter to the reservoir. The filter remained saturated during this stage. The pore-water pressure in the filter was then raised back to zero suction by raising the water level up to the top of the filter.

Stage 2 – Specimen preparation

Once the silt filter had been put in place and consolidated, the sand specimen was prepared. The material was oven-dried, mixed and placed into a purposely manufactured pluviator to obtain a specimen with level top surface after pluviation. A schematic layout of the pluviator is shown in *Figure 2.3*. During pluviation, the base pedestal drainage channels were kept open (valve B closed, valve A open in *Figure 2.2a*) to prevent

desaturation of the silt filter due to water uptake by the specimen due to capillarity. Water uptake occurring during pluviation was continuously monitored by recording any water exchanges between the specimen and the water reservoir using the balance. This allowed the degree of saturation of the soil specimen to always be known. After pluviation, the top cap was placed on top of the specimen after interposing a filter paper.
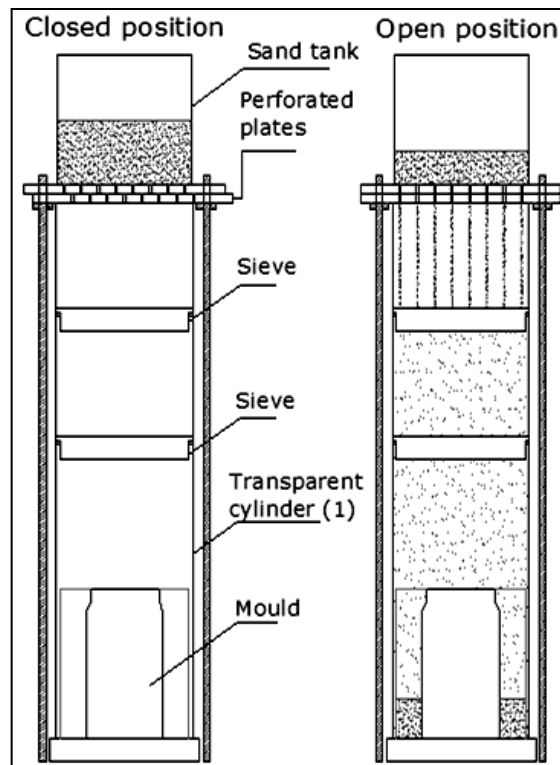

Figure 2.3. Pluviator in closed and open position during specimen preparation

Stage 3 – First wetting and first drying

After the specimen was pluviated, a first wetting path was performed. With the bottom drainage still connected to the reservoir, the water level was raised slightly above the top of the specimen. Once equilibrium was reached, the mass of exchanged water was used to calculate the degree of saturation of the specimen. At the end of this stage, the degree of saturation reached a value of 0.85. With the split mould still in place, the reservoir was lowered in steps to apply a suction, make the specimen able to self-stand and to allow grain

rearrangements to take place when the height of the specimen could still be measured directly. For each value of negative hydraulic head the water exchange between the specimen and the reservoir was continuously monitored and the degree of saturation of the specimen was calculated. The split mould was then removed and the triaxial cell was assembled on the cell base and filled with de-aired water. Finally, a cell pressure of 10 kPa was applied through the pressure/volume controller device (valve C open in *Figure 2.2a*).

Stage 4 – Re-wetting and back pressure application

The specimen was re-saturated by raising the water reservoir up above the top of the specimen. As for the first wetting path, the degree of saturation at the end of this stage didn't reach unity. Therefore, a full saturation procedure had to be performed in order to reach a higher degree of saturation ($S_r > 0.95$). The base pedestal was disconnected from the water reservoir and connected to the second pressure/volume controller device (valve B open, valve A closed in *Figure 2.2a*). The specimen was subjected to step-by-step increments of pore-water pressure (back pressure). During this stage, cell pressure was increased accordingly in order to keep the effective stress state of the specimen constantly equal to 10 kPa. Full saturation was considered to be achieved when the change in pore-water pressure under undrained conditions associated with change in cell pressure was greater than 0.98 of the change in cell pressure (*B*=0.98).

Stage 5 – Drying and wetting cycle with wave velocity measurements

After the saturation procedure was performed, the base pedestal was disconnected from the second pressure/volume controller device and reconnected to the water reservoir (valve B closed, valve A open in *Figure 2.2a*). The hanging water column method was adopted to apply suction at the base of the specimen and perform drying and wetting cycles (by

maintaining a constant cell pressure of 10 kPa). With valve B closed and valve A and D open, the water reservoir was lowered/raised in steps inducing a specimen-to-reservoir/reservoir-to-specimen water flow. For each value of negative hydraulic head, the degree of saturation of the specimen was calculated. Enough time was allowed for the pore-water within the specimen to reach hydraulic equilibrium with the water in the reservoir, ranging from 30 to 2500 minutes. Once equilibrium was reached for each suction step, the function generator was used to trigger the propagation of a shear wave through the specimen, while the oscilloscope recorded the input and output signals.

Stage 6 – Specimen last de-saturation and cell dismantling
At the end of the test, the specimen was de-saturated in a single step to make it self-standing. The cell was then emptied and dismantled, and the specimen's final height, diameter and water content were measured.

2.3.   EXPERIMENTAL RESULTS

2.3.1.   Water retention characteristics of the soil specimen

Figure 2.4 shows the relationship between the average degree of saturation and the distance between the top of the specimen and the level of water in the reservoir (referred to as 'reservoir height' for simplicity) during first wetting, first drying, re-wetting, saturation under positive pressure, and final drying-wetting cycle. The first drying path was performed with the split mould still in place (cell pressure equal to zero). The drying-wetting cycle was performed with a confining pressure of 10 kPa. The value of degree of saturation at the end of the saturation procedure (i.e. at the beginning of the drying-wetting cycle, point D) was back calculated from the value of water content taken at the end of the

test and was found to be equal to 0.96. The data points associated with the first drying (AB) and main drying (DE) appear to lead to a similar air-entry value. This implicitly suggests that negligible deformation was occurring upon the first drying path.
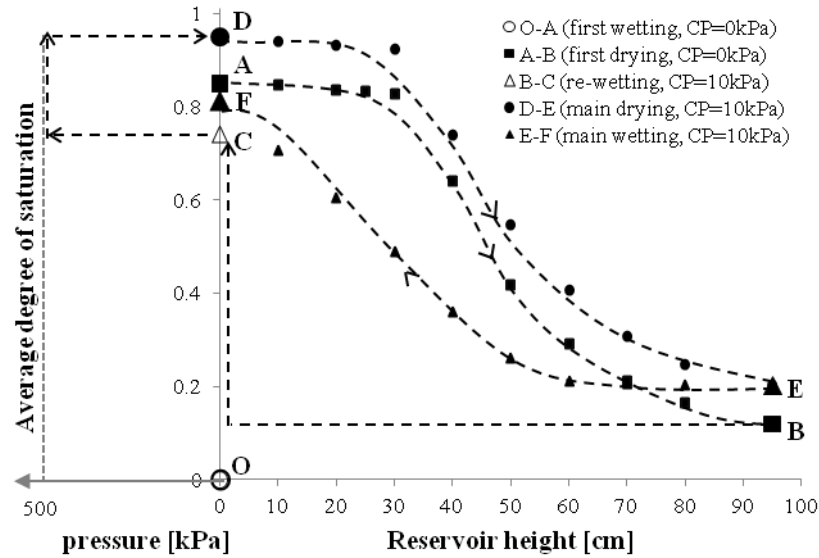

Figure 2.4. Average degree of saturation during first wetting, first drying, re-wetting, main drying and main wetting

The experimental data shown in *Figure 2.4* have been derived by associating the average degree of saturation (calculated from the measured overall mass of water within the specimen) to the height of the water reservoir. However, suction and degree of saturation vary significantly along the height of the specimen (12.5 cm). A difference in suction of 1.22 kPa exists between the top and the bottom of the specimen and this corresponds to a significant difference in degree of saturation.

In order to derive the water retention behaviour of the specimen more accurately, an approach similar to the one adopted by Stanier & Tarantino (2013) was followed. The water behaviour curve was modelled by fitting the water volume changes rather than the average values of suction and degree of saturation. Let us consider the specimen in *Figure 2.5a*. When lowering the reservoir from position 1 to position 2 (drying path), points A, B,

C and D at different heights within the specimen are all de-saturating from a saturated state. Therefore, they all move along a main drying curve, and reach different degrees of saturation at equilibrium as shown in *Figure 2.5c* (points A2 to D2).

When raising the reservoir from position 2 to position 3 (*Figure 2.5b*), points A, B, C and D will re-saturate from the different states of saturation that they reached after main drying. Therefore, they will move along different scanning wetting curves as shown in *Figure 2.5c* (points A3 to D3).
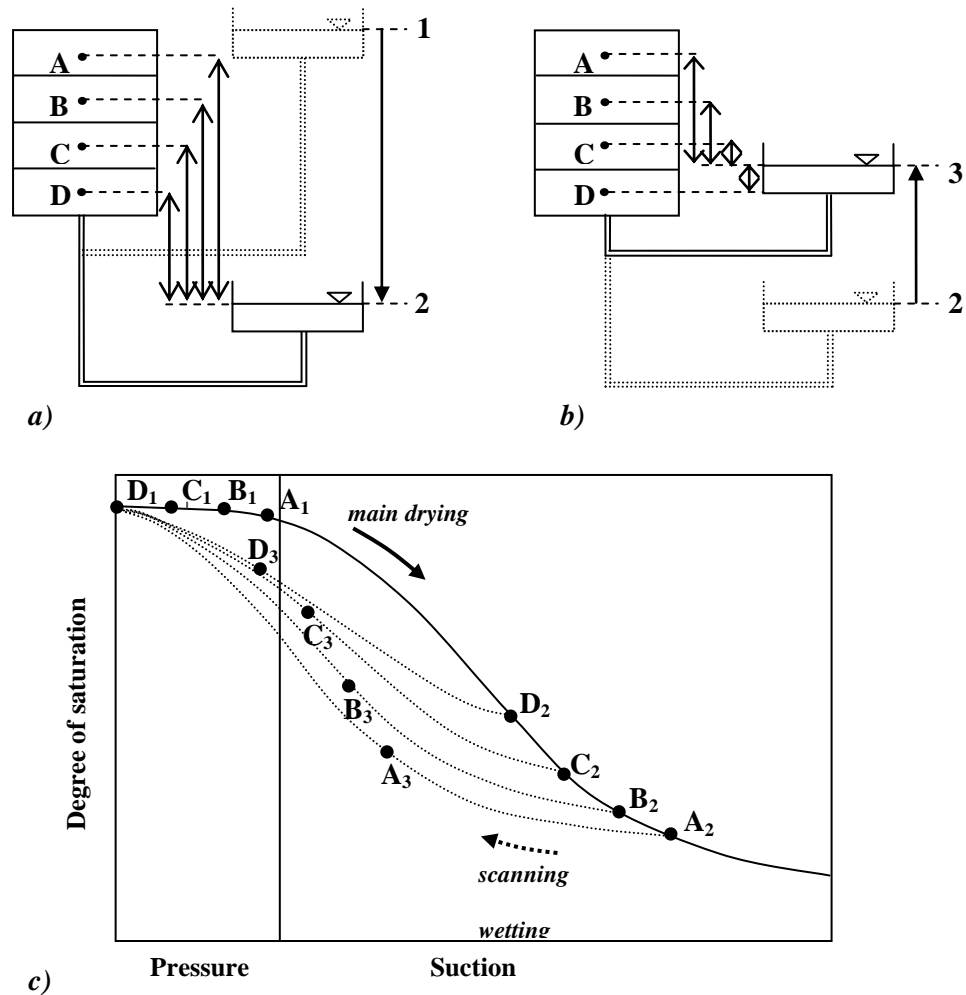
Figure 2.5. Schematic view of the application of suction during a) drying path, and b) wetting path; c) hydraulic paths followed by points at different elevations in the specimen during drying and wetting paths.

53

To model the water retention behaviour, van Genuchten-type functions (van Genuchten, 1980) were considered for the drying path and the scanning wetting paths. In turn, the function used to model a scanning path was assumed to be derived from the main wetting path by 'scaling' the main wetting curve via a fictitious residual volumetric water content. The following functions were considered:

$$\textbf{\textit{Main drying:}} \quad \theta^d = \theta^d_R + \frac{\theta^d_0 - \theta^d_R}{\left[1 + \left(\alpha^d \cdot s\right)^{n^d}\right]^{m^d}} \tag{3}$$

$$\textbf{\textit{Main wetting:}} \quad \theta^w = \theta^w_R + \frac{\theta^w_0 - \theta^w_R}{\left\{1 + [\alpha^w \cdot (s - s^*)]^{n^w}\right\}^{m^w}} \tag{4}$$

$$\textbf{\textit{Scanning wetting:}} \quad \theta^{sc} = \theta^{sc}_R + \frac{\theta^w_0 - \theta^{sc}_R}{\left\{1 + [\alpha^w \cdot (s - s^*)]^{n^w}\right\}^{m^w}} \tag{5}$$

where θ is the (volumetric) water content, θ_R is the residual water content, θ_0 is the water content at suction lower than or equal to zero (pore-water pressure greater than or equal to zero), s is the suction, α, n and m are fitting parameters (with $m = 1 - 1/n$), and the superscripts d, w and sc refer to main drying, main wetting and scanning wetting path respectively.

For the main drying curve, the volumetric water content at suction lower than or equal to zero θ^d_0 was derived from the volumetric water content measured experimentally at the positive pore-water pressure (back-pressure) of 500 kPa. The parameters α^d, n^d and θ^d_R were derived by matching the overall volume of water measured at each suction step upon the drying path with the integral of the main drying retention function (Equation 3) over the height of the specimen (a hydrostatic distribution of suction was assumed at equilibrium).

For the main wetting curve, the volumetric water content at residual state and at suctions lower than or equal to zero were assumed to be equal to the values associated with the main drying path, $\theta_R^d \equiv \theta_R^w$ and $\theta_0^d \equiv \theta_0^w$ respectively. Since the experimental data in *Figure 2.4* showed an average degree of saturation significantly lower than unity when the reservoir was level with the top surface of the specimen, an additional parameter s^* was introduced in the van Genuchten equation representing the value of negative suction (i.e. positive pressure) leading to a volumetric water content equal to θ_0^w.

For the scanning wetting curves, the parameter θ_R^{sc}, which is the fictitious residual water content used to scale the scanning wetting curve from the main wetting curve, was derived by imposing that the scanning curve intersects the main drying curve at the value of suction at the end of the drying path (level 2 in *Figure 2.5a-b*):

$$\theta_R^{sc} = \frac{\theta_R^d + \dfrac{\theta_0^d - \theta_R^d}{\left[1+(\alpha^d \cdot s)^{n^d}\right]^{m^d}} - \dfrac{\theta_0^w}{\{1+[\alpha^w \cdot (s-s^*)]^{n^w}\}^{m^w}}}{1 - \{1 + [\alpha^w \cdot (s - s^*)]^{n^w}\}^{m^w}} \qquad\qquad 6$$

To calculate the volume of water of the specimen along the wetting path, the specimen was divided into four slices as shown in *Figure 2.5a-b*, each slice following a different scanning path. The parameters s^*, α^w, and n^w were derived by matching the overall volume of water measured at each suction step upon the wetting path with the integral of the four scanning retention functions over the height of the slice (Equation 5). The main drying curve, main wetting curve and scanning wetting curves derived from this best-fitting using the least-square method are shown in *Figure 2.6*, and the corresponding fitting parameters are reported in *Table 2.3*. For comparison, the experimental data in terms of the average suction and degree of saturation are also shown in the figure.
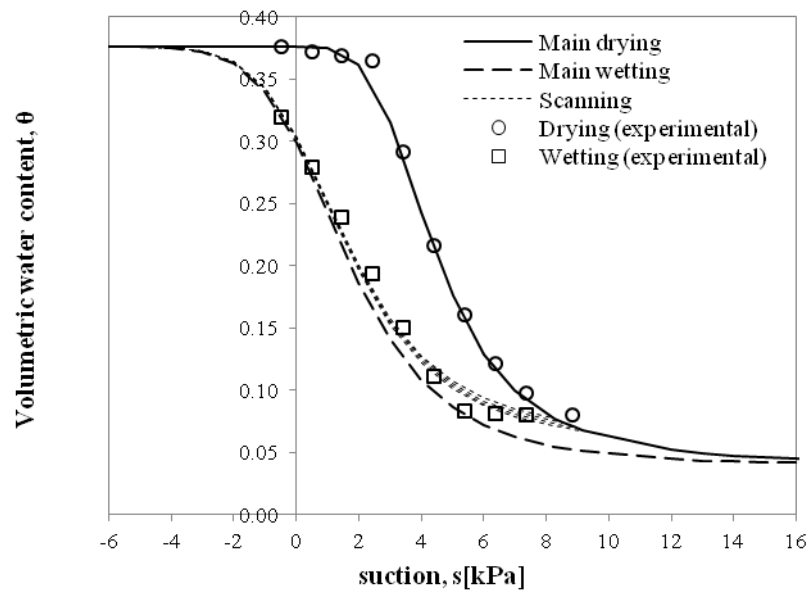
Figure 2.6. WRCs for main drying, main wetting and scanning wetting paths

using van Genuchten functions

α^d	0.25
n^d	4
α^w	0.12
n^w	5.98
s^*	-6.85

Table 2.3. Parameters of the water retention functions

2.3.2. Wave propagation results and interpretation

At each suction step of the drying-wetting cycles, the velocity of propagation of a shear wave was derived using the bender element technique. A sinusoidal signal with a frequency of 5 kHz was adopted as input signal for the transmitter bender element. The waveform and input frequency used in this study were chosen to guarantee a reliable measurement of the arrival time. The adopted input frequency allowed the output signal to be detected easily during the whole test. The sinusoidal waveform was observed to cause

smaller ambiguity in arrival time than other types of waveform, such as square-shaped signals (Blewett, et al., 2000; Leong, et al., 2005; Viana da Fonseca, et al., 2009).

Figure 2.7 shows the input signal and some of the output signals recorded during the tests. Each raw output signal was subject to filtering (Butterworth, low pass filter of order 1) and base-line correction prior to travel time interpretation, in order to remove the undesired effect of background noise without affecting the signal characteristics. Once each output signal was filtered and corrected, the velocity of propagation of the shear wave through the specimen was calculated as:

$$V_s = \frac{L_{tt}}{t} \qquad\qquad 7$$

where V_s is the shear-wave velocity, L_{tt} is the travel length and t is the travel time of the wave. Three bender element measurements were taken for each suction step. The final value of shear-wave velocity for each step was then calculated as the average of the three measurements. The difference between the minimum and maximum of the shear-wave velocities in the triplicate measurement was found to be less than 1.5 % of the average value.

The travel length L_{tt} was taken as the tip-to-tip distance between source and receiver bender elements. This approach has been widely adopted in the literature (Dyvik & Madshus, 1985; Viggiani & Atkinson; 1995a, Fernandez, 2000). As the cell pressure was kept constant during the drying-wetting cycles, volume changes occurring in the cell and measured by the pressure/volume controller (P/V controller 1 in *Figure 2.2a*) could be attributed to changes in the volume of the specimen. Under the assumption of isotropic behaviour, the axial deformation and, hence, the tip-to-tip travelling distance could be inferred from the volume change. The total axial deformation was found to be less than

0.37 % of the specimen height, resulting in a maximum error on the shear-wave velocity $\Delta V_s = \pm 0.35$ m/s, which was assumed to be negligible.

The determination of the travel time is more controversial. Although many researchers have proposed different approaches (Dyvik & Madshus, 1985; Viggiani & Atkinson, 1995a; Viggiani & Atkinson, 1995b; Jovicic & Coop, 1997; Santamarina & Fam, 1997), there is still no agreement about the most reliable method for travel time interpretation. In this study, the travel time of the wave was chosen as the time interval between characteristic points (first main peaks) of the input and output signals. This procedure is a simple alternative to more complex methods such as cross-correlation or cross-power of the transmitter and receiver signals (Viggiani & Atkinson, 1995a). Although the resulting absolute values of wave velocity might be slightly less accurate, changes in stiffness during the test can be determined accurately as long as the choice of the arrival time is consistent throughout the analysis of the data (Viggiani & Atkinson, 1995b).
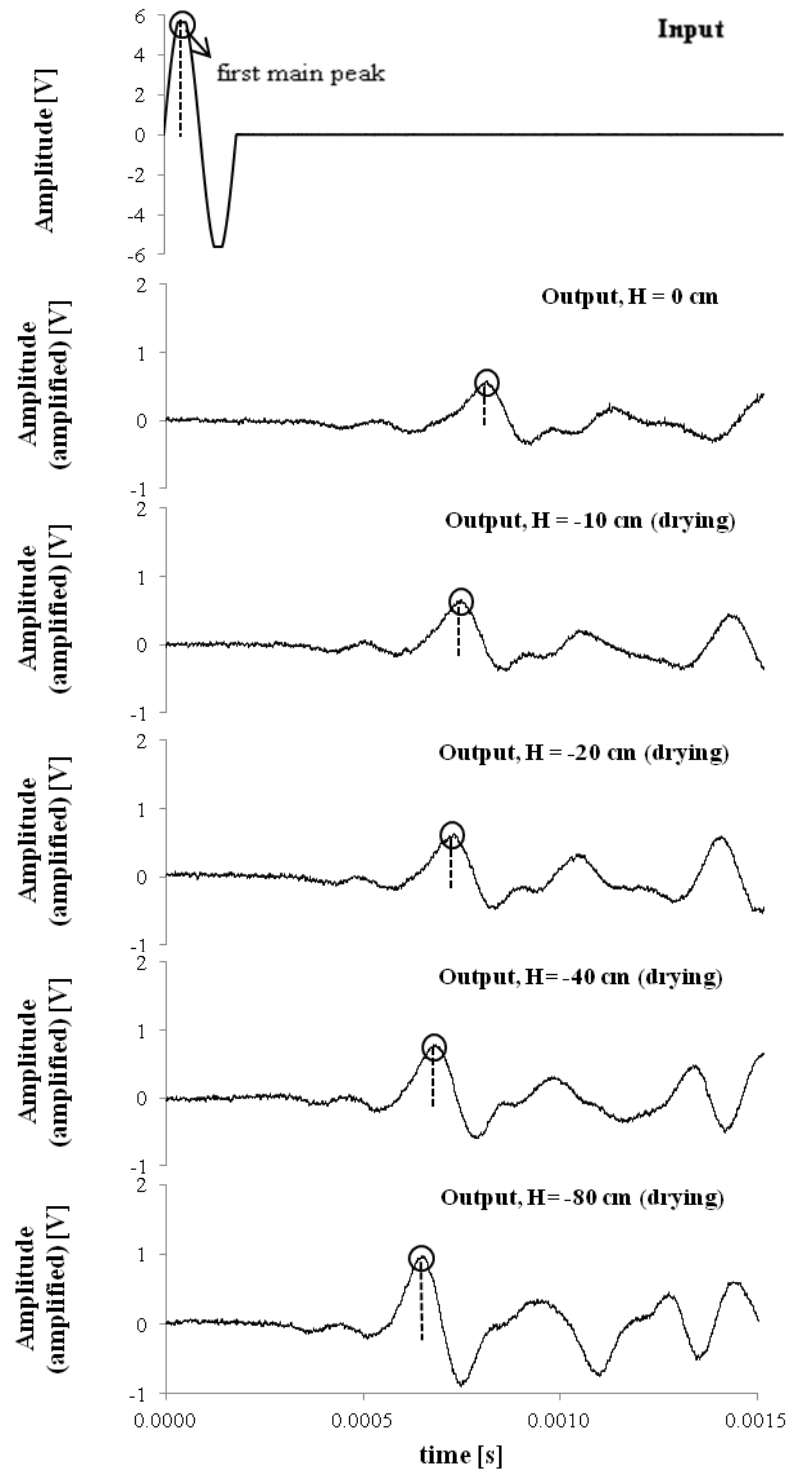
Figure 2.7. Examples of input signal (sinusoidal pulse) and corrected

output signals with identification of first main peaks for travel time

interpretation

2.3.3. **Small-strain stiffness calculation**

Interpretation of bender element tests is based on the assumption that the soil behaves as a linear elastic material at very small strain. The shear modulus can then be determined from the elastic wave propagation theory as:

$$G_0 = \rho \, V_s^2 \qquad\qquad\qquad 8$$

where ρ is the bulk density of the soil specimen and V_s is the velocity of the shear wave propagating through the sample. *Figure 2.8* shows the evolution of the small-strain shear modulus with the relative distance between the top of the specimen and the water level in the reservoir. It appears that G_0 increases significantly with suction, and the soil appears to be stiffer upon a wetting path rather than a drying path.
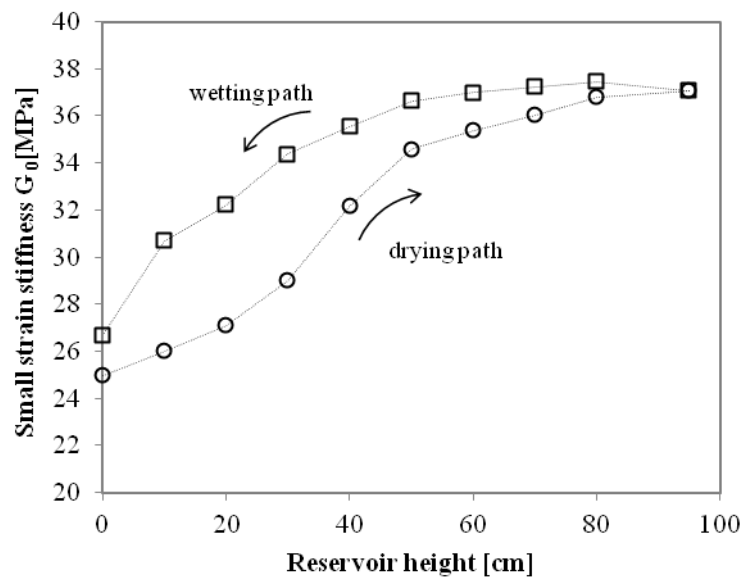
Figure 2.8. Small strain stiffness evolution during hydraulic hysteresis

2.4. MICROSCALE-BASED MODEL FOR G_0 IN UNSATURATED SOILS

The approach followed in this paper to model the independent effect of suction and degree of saturation on the small-strain shear modulus G_0 consists of linking G_0 to an unsaturated intergranular stress σ_i, which depends in turn on both suction and degree of saturation. The intergranular stress is derived from equilibrium considerations at the particle-scale by assuming that water at the inter-particle contacts is present in the form of either bulk or meniscus water. The functional form that links the small-strain shear modulus to the intergranular stress is derived on the basis of simplified micro-mechanical models. The different steps to derive G_0 as a function of σ_i are schematically illustrated in *Figure 2.9*.
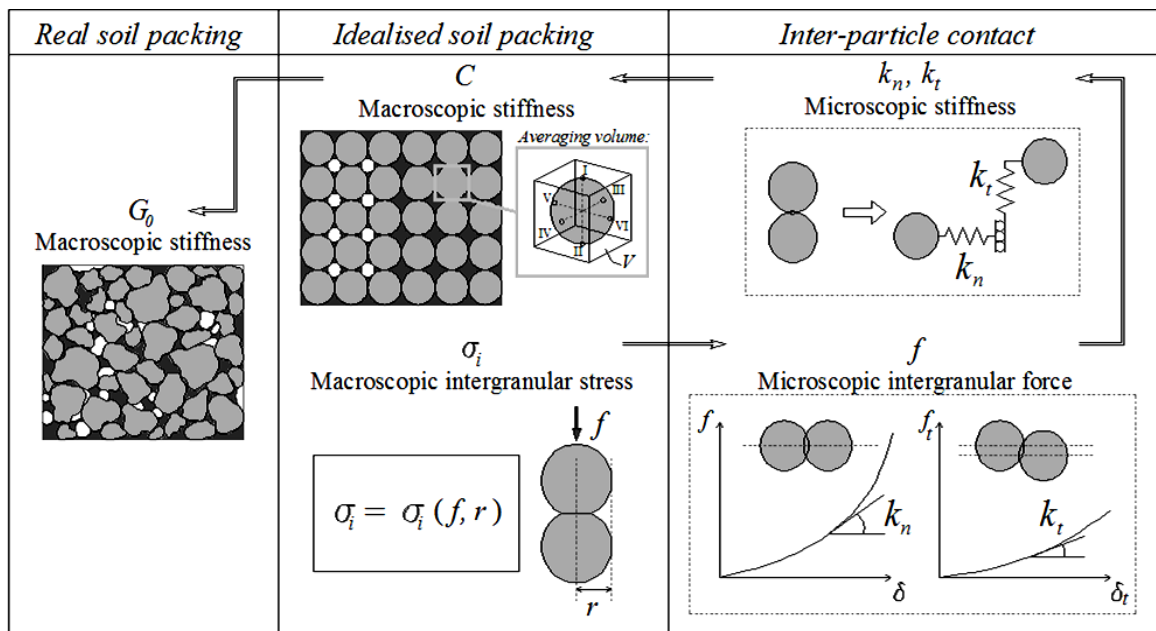
*Figure 2.9.*Schematic illustration of the proposed model: from macroscopic intergranular stress to macroscopic stiffness

Macroscopic intergranular stress of unsaturated packings

The degree of saturation/suction-induced intergranular stress, σ_i, may be formulated by considering an idealised packing of equal spheres in an ordered structure. Let us consider the idealised unsaturated packing as shown in *Figure 2.10,* and let us assume that the contact area of each pair of spherical particles is a point. The two-phase fluid can be described as the coexistence of a region fully occupied by bulk water (saturated region) and a region occupied by the menisci alone. Boso et al. (2005) derived an expression of the intergranular stress σ_i of the unsaturated packing as:

$$\sigma_i = \sigma + \left[\sigma_i^b \frac{S_r - S_{rm}}{1 - S_{rm}} + \sigma_i^m \left(1 - \frac{S_r - S_{rm}}{1 - S_{rm}}\right)\right] \qquad 9$$

where S_r is the total degree of saturation, S_{rm} is the residual degree of saturation (degree of saturation of the region occupied by the menisci alone), σ is the total stress, σ_i^b is the intergranular stress in the bulk water region, and σ_i^m is the intergranular stress in the meniscus water region.

The first term in square brackets takes into account the contribution of suction to the intergranular stress in the saturated region, which is directly proportional to the suction (as $\sigma_i^b \equiv s$). The second term in square brackets indicates the contribution of suction to the intergranular stress in the meniscus water region. The two contributions of suction in *Equation 9* are weighed by functions of the degree of saturation based on the assumptions that i) the areal degree of saturation equals the volumetric degree of saturation and ii) the variation of the volume occupied by the meniscus with suction can be neglected.

To explore the nature of the intergranular stress at the meniscus contact, it is convenient to examine the case of two rigid spherical particles with point contact. According to Fisher (1926), σ_i^m is given by:

$$\sigma_i^m = \frac{\frac{2\pi r T}{1+\tan(\theta/2)}}{\pi r^2} \qquad\qquad 10$$

where θ is the angle defining the position of the meniscus junction, r is the particle radius, and T is the surface tension. The angle θ is related to suction according to the following equation:

$$s = T \left[\frac{1}{r\left(\frac{1}{\cos\theta} - 1\right)} - \frac{1}{r\left(1 + \tan\theta - \frac{1}{\cos\theta}\right)} \right] \qquad\qquad 11$$

By combining *Equation 10* and *Equation 11*, the relationship between the suction s and the intergranular stress σ_i^m in the meniscus water region can be derived. *Figure 2.10b* shows the variation of σ_i^m with suction for the case of $T = 0.072$ N/m and $r = 0.1$ mm, with θ ranging from 53° (roughly corresponding to zero suction) to 22°. For the purpose of comparison, the bulk water intergranular stress σ_i^b is also plotted. It can be seen that σ_i^m can be assumed practically independent of suction.

Accordingly, the assumption made in the proposed model is that σ_i^m is independent of suction even for the case of real, non-spherical particles. In this case, however, the value of σ_i^m cannot be derived using *Equation 10* but has to be calibrated experimentally as described later on in the paper.
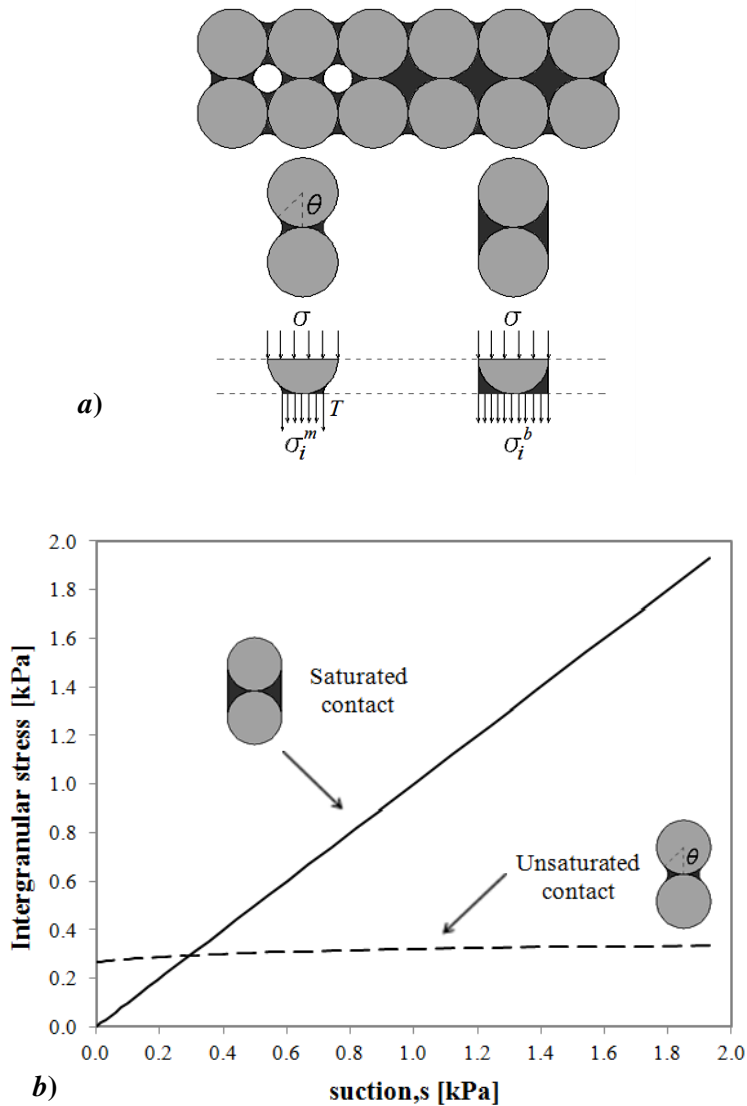
Figure 2.10. Unsaturated soil packing: a) idealised unsaturated soil; b) evolution of the intergranular stress in the meniscus water region and in the bulk water region with suction

Micro-mechanical model: from macroscopic intergranular stress to microscopic intergranular force and stiffness

In order to derive the functional form linking the macroscopic intergranular stress σ_i in *Equation 9* to the shear modulus G_0 a micro-mechanical model was used, based on the implicit assumption that the pore- fluid is homogenous and at zero pressure (e.g. air).

Existing micro-mechanical models allow to derive general expressions of the macroscopic intergranular stress tensor, $(\sigma_i^*)_{\alpha\beta}$, of an idealised packing of discrete particles as a function of the microscopic intergranular force f developing at each particle contact, using different averaging techniques (e.g. Liao & Chang, 1997; Kruyt & Rothenburg, 1998; Kruyt & Rothenburg, 2001). Using the particle-in-volume averaging method, the following expression can be derived (Luding, 2004; Luding, 2005):

$$(\sigma_i^*)_{\alpha\beta} = \frac{1}{V} \sum_{p \in V} \sum_{c=1}^{N} l_\alpha^c f_\beta^c \qquad\qquad 12$$

where V is an averaging representative volume within the packing, N is the number of contacts contained in the averaging volume, l is the component of the branch vector connecting the centres of particles in contact, the apex c indicates the single contacts within V, p is the generic particle occurring within V, and α, β are subscripts that indicate the combinations of the vertical and horizontal directions. In this study, only the normal component of the intergranular stress tensor was considered, i.e. $(\sigma_i^*)_{\alpha\alpha} = \sigma_i^*$:

$$\sigma_i^* = \frac{1}{V} \sum_{p \in V} \sum_{c=1}^{N} l^c f^c \qquad\qquad 13$$

where f is intended as the normal component of the force between two particles in contact. In turn, the force f can be derived as a function of the normal stiffness at the contact, k_n, and the relative displacement in the normal direction, δ:

$$f = f(k_n, \delta) \qquad\qquad 14$$

Following the Hertzian contact model (*Figure 2.11*), the force f can be derived as a non-linear function of δ (Love, 1927):

$$f = k_{n0}\delta^{3/2}$$

<div align="right">*15*</div>

where k_{n0} is a material constant depending on the characteristics of individual particles. In this study, k_{n0} is a model parameter determined experimentally as discussed later on in the paper.

Using *Equation 15* the incremental stiffness k_n can be written in terms of the force f and the model parameter k_{n0} as:

$$k_n = \frac{\partial f}{\partial \delta} = \frac{3}{2}k_{n0}\delta^{1/2} = \frac{3}{2}k_{n0}^{2/3}f^{1/3}$$

<div align="right">*16*</div>

In order to calculate the shear modulus of the packing (as described in the following paragraph), a tangential stiffness at the contact k_t was also introduced. For the sake of simplicity, the tangential stiffness k_t was assumed to be equal to a fraction of the normal stiffness k_n:

$$k_t = \frac{2}{7}k_n$$

<div align="right">*17*</div>
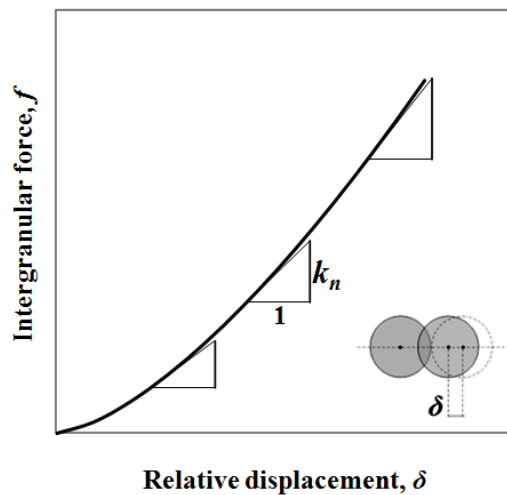
*Figure 2.11.*Hertzian contact model

Micro-mechanical model: from microscopic stiffness to macroscopic stiffness

The simplest approach to derive the macroscopic stiffness of idealised aggregates of identical, randomly distributed spherical particles is based on the mean-field theory (e.g. Digby, 1981; Walton, 1987). The theory assumes that individual particles move according to an external uniform strain field. Starting from this assumption, the macroscopic stiffness tensor can be derived (e.g. Liao & Chang, 1997; Kruyt & Rothenburg, 1998; Chang and Hicher, 2005; Luding, 2004; Luding, 2005):

$$C_{\alpha\beta\gamma\phi} = \frac{1}{V} \sum_{p \in V} \left(k_n \sum_{c=1}^{N} (l^2/2) \, n_\alpha^c n_\beta^c n_\gamma^c n_\phi^c + k_t \sum_{c=1}^{N} (l^2/2) \, n_\alpha^c t_\beta^c n_\gamma^c t_\phi^c \right) \qquad 18$$

where α, β, γ, ϕ are subscripts that indicate the combinations of the vertical and horizontal directions, and n and t are the components of the normal and tangential unit vector at contact respectively, and k_n and k_t are non-linear stiffness given by *Equations 16* and *17*. The shear modulus is associated with the term C_{1212} of the stiffness tensor, where *1* and *2* are the vertical and horizontal direction respectively. Different expressions of C_{1212} can be derived depending on the particle configuration.

Micro-mechanical model: regular packings

A simplified approach for deriving C_{1212} and σ_i^* was followed in this study, i.e. the soil aggregate was idealised as a packing of identical spherical particles in a regular structure. The lattice-type geometry of the system allows to derive explicit expressions of the macroscopic tensors. As an exercise, two different configurations (simple cubic, SC, and body centred cubic, BCC) were selected (*Figure 2.12*) in order to ascertain the validity of the model irrespective of the choice of the particle configuration.
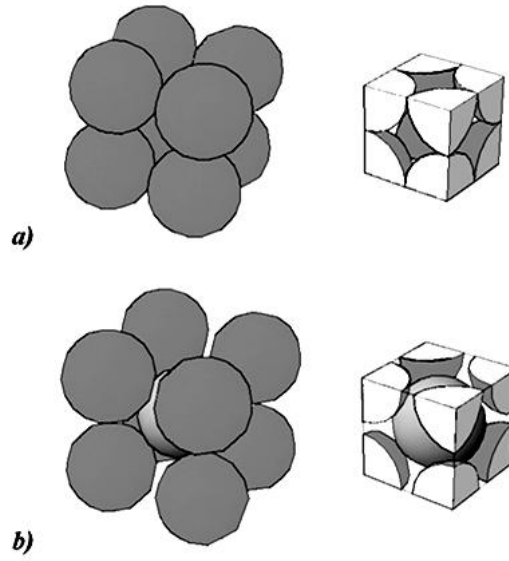
*Figure 2.12.*Idealised particle configuration: a) simple cubic (SC) and b)

body centred cubic (BCC)

For the case of SC configuration (*Figure 2.12a*), the elementary averaging volume V is a cube whose inscribed sphere is a single particle (or equally, a cube containing eight 1/8 of a particle, whose corners are the centres of the particles):

$$\textbf{SC}: \ V = (2r)^3 = 8r^3 \qquad\qquad 19$$

Thus, both σ_i^* and C_{1212} can be calculated from *Equation 12* and *18* respectively as an average over 6 contacts, and are representative of the overall volume:

$$\textbf{SC}: \ \sigma_i^* = \frac{1}{V}\sum_{c=1}^{6} l^c f^c = \frac{2l}{V} f \qquad\qquad 20$$

$$\textbf{SC}: \ C_{1212} = \frac{1}{V}\frac{l^2}{2}\left(k_n \sum_{c=1}^{6} n_1^c n_2^c n_1^c n_2^c + k_t \sum_{c=1}^{6} n_1^c t_2^c n_1^c t_2^c \right) = \frac{l^2}{V} k_t = \frac{2}{7}\frac{l^2}{V} k_n \qquad 21$$

For the case of BCC configuration (*Figure 2.12b*), the elementary averaging volume is a cube containing a total of 2 particles (one whole particle placed in the centre of the cube,

plus eight 1/8 of a particle placed in each corner of the cube), whose corners are the centres of the eight particles surrounding the particle in the cube's centre:

$$\textbf{BCC:} \quad V = \left(\frac{4}{\sqrt{3}}r\right)^3 = \frac{64}{3\sqrt{3}}r^3 \qquad\qquad 22$$

Thus, both σ_i^* and C_{1212} can be calculated from *Equation 12* and *18* respectively as an average over 8 contacts for each of the 2 particles within the averaging volume, and are representative of the overall volume:

$$\textbf{BCC:} \; \sigma_i^* = \frac{1}{V}2\sum_{c=1}^{8} l^c f^c = \frac{16l}{V}f \qquad\qquad 23$$

$$\textbf{BCC:} \; C_{1212} = \frac{1}{V}\frac{l^2}{2}\left[2\left(k_n\sum_{c=1}^{8} n_1^c n_2^c n_1^c n_2^c + k_t\sum_{c=1}^{8} n_1^c t_2^c n_1^c t_2^c\right)\right] = \frac{l^2}{V}\left(\frac{8}{9}k_n + \frac{16}{9}k_t\right) = \frac{88}{63}\frac{l^2}{V}k_n \qquad 24$$

From *Equation 20* and *23*, we have:

$$\textbf{SC:} \quad f = \frac{\sigma_i^*}{2l}V \qquad\qquad 25$$

$$\textbf{BCC:} \quad f = \frac{\sigma_i^*}{16l}V \qquad\qquad 26$$

By combining *Equations 21* and *24* with *Equation 16* and *Equations 25* and *26*, two possible functional forms (one for each configuration) that link the shear modulus C_{1212} with intergranular stress σ_i^* can be derived. These functional forms were assumed to also characterise the relationship between the small-strain shear modulus G_0 of the unsaturated soil specimen and the suction/degree of saturation-induced intergranular stress, σ_i. In other words, C_{1212} was replaced by G_o and σ_i^* was replaced by σ_i (the latter given by *Equation 9*), leading to the following expressions:

$$\textbf{SC:}\; G_o \equiv C_{1212} = \frac{2}{7}\frac{l^2}{V}\frac{3}{2}k_{n0}{}^{2/3}\left(\frac{\sigma_i^*}{2l}V\right)^{1/3} \equiv \frac{2}{7}\frac{l^2}{V}\frac{3}{2}k_{n0}{}^{2/3}\left(\frac{\sigma_i}{2l}V\right)^{1/3} \qquad\qquad 27$$

$$\textbf{BCC:}\; G_o \equiv C_{1212} = \frac{88}{63}\frac{l^2}{V}\frac{3}{2}k_{n0}{}^{2/3}\left(\frac{\sigma_i^*}{16l}V\right)^{1/3} \equiv \frac{88}{63}\frac{l2}{V}\frac{3}{2}k_{n0}{}^{2/3}\left(\frac{\sigma_i}{16l}V\right)^{1/3} \qquad\qquad 28$$

2.5. CALIBRATION AND VALIDATION OF THE MODEL

2.5.1. Calibration against experimental data

The proposed model was calibrated and validated against the experimental results obtained in this study. Two model parameters need to be identified, namely k_{n0} and σ_i^m. In the macroscopic model, these parameters should be intended as macroscopic parameters with an intuitive physical micro-scale meaning. In particular, k_{n0} does not represent anymore a material property as in the micro-mechanical model, but a model parameter that accounts for a number of characteristics of the real soil packing including the particle stiffness, particle shape, particle size distribution, particle arrangements etc.

A calibration procedure was devised to determine k_{n0} and σ_i^m against the small-strain shear modulus at saturation, G_0^{sat}, and at residual saturation, G_0^{res}, respectively. An equivalent particle radius $r = l/2 = D_{50}/2$ was also selected (although it can be shown that the choice of the equivalent particle radius does not affect the performance of the model, as it would just lead to different values of k_{n0} and σ_i^m).

Calibration of k_{n0} at saturation

The measurement of G_0^{sat} was taken at the beginning of the drying path, after the saturation procedure. In this case, the intergranular stress in *Equation 9* equals the confining pressure (cell pressure, σ_{CP}) only:
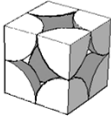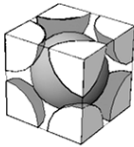
$$\sigma_i = (\sigma_i)^{sat} = \sigma - u_w = \sigma_{CP} \qquad\qquad\qquad 29$$

The model parameter k_{n0} can therefore be derived by inverting *Equations 27* and *28* with $G_0 = G_0^{sat}$, $\sigma_i = \sigma_{CP}$, and $l = 2r$:

$$\textbf{SC: } k_{n0} = \left[\frac{14}{3}\frac{r\,G_0^{sat}}{(2r^2\,\sigma_{CP})^{1/3}}\right]^{3/2} \qquad\qquad 30$$

$$\textbf{BCC: } k_{n0} = \left[\frac{28}{11\sqrt{3}}\frac{r\,G_0^{sat}}{\left(\frac{2}{3\sqrt{3}}r^2\,\sigma_{CP}\right)^{1/3}}\right]^{3/2} \qquad\qquad 31$$

Table 4 shows the calibrated parameter k_{n0} for SC and BCC configurations.

	k_{n0} [kN/m$^{3/2}$]	$\sigma_i{}^m$ [kPa]
SC		
	99503.6	22.7
BCC		
	40084.5	22.7

Table 2.4. Model parameters k_{n0} and $\sigma'_m{}^i$

Calibration of σ_i^m at residual saturation

The measurement of the second parameter needed for calibration, G_0^{res}, was taken at the end of the main drying path, where $S_r = S_{rm}$. In this situation, the intergranular stress σ_i in *Equation 9* depends on the confining pressure σ_{CP} and on the (unknown) intergranular stress at meniscus contacts σ_i^m, regardless of suction:

$$\sigma_i = (\sigma_i)^{res} = \sigma_i^m + \sigma_{CP} \qquad\qquad 32$$

The model parameter σ_i^m can therefore be derived by inverting *Equations 27* and *28* with $G_0 = G_0^{res}$, $\sigma_i = \sigma_i^m + \sigma_{CP}$, and $l = 2r$:

$$\textbf{SC:} \quad \sigma_i^m = \frac{1}{2r^2}\left(\frac{14}{3}\frac{r\,G_0^{res}}{k_{n0}^{2/3}}\right)^3 - \sigma_{CP} \qquad\qquad 33$$

$$\textbf{BCC:} \quad \sigma_i^m = \frac{3\sqrt{3}}{2r^2}\left(\frac{28}{11\sqrt{3}}\frac{r\,G_0^{res}}{k_{n0}^{2/3}}\right)^3 - \sigma_{CP} \qquad\qquad 34$$

Table 4 shows the parameter σ_i^m for both SC and BCC configurations. As a result of the calibration procedure against the experimental data, the values of σ_i^m are identical.

2.5.2. Validation against experimental data

Once the parameter σ_i^m was derived at residual saturation, the intergranular stress σ_i and the corresponding intergranular force was calculated (*Equation 9* and *25* for SC and *Equation 9* and *26* for BCC). In particular, in order to take into account the variability of the degree of saturation within the specimen, bounding values of the intergranular stress (corresponding to bounding values of the stiffness C_{1212}) were estimated. For the lower bound solution, the degree of saturation appearing in *Equation 9* was calculated along the drying and wetting paths using the main drying and scanning wetting van Genuchten-type curves respectively (*Equation 3* and *5*), with suction *s* equal to the values of suction corresponding to the bottom height of the specimen (*Figure 2.13b-c*). The same approach was followed for the calculation of the upper bound solution, but with suction *s* equal to the values of suction corresponding to the top height of the specimen (*Figure 2.13b-c*). From the value of k_{n0} previously calibrated, the stiffness values k_n and k_t for the upper

and lower bounds were calculated for each combination of suction and degree of saturation (*Equation 16* and *17*), and were then used to derive C_{1212} (*Equation 21* and *24*).

Figure 2.13a shows the comparison between the values of G_0 obtained experimentally and the simulated stiffness C_{1212}. The model gives an accurate prediction of the small-strain shear modulus during hydraulic hysteresis. The variation of G_0 with suction is well captured at a qualitative and quantitative level.

a)

b) Main drying
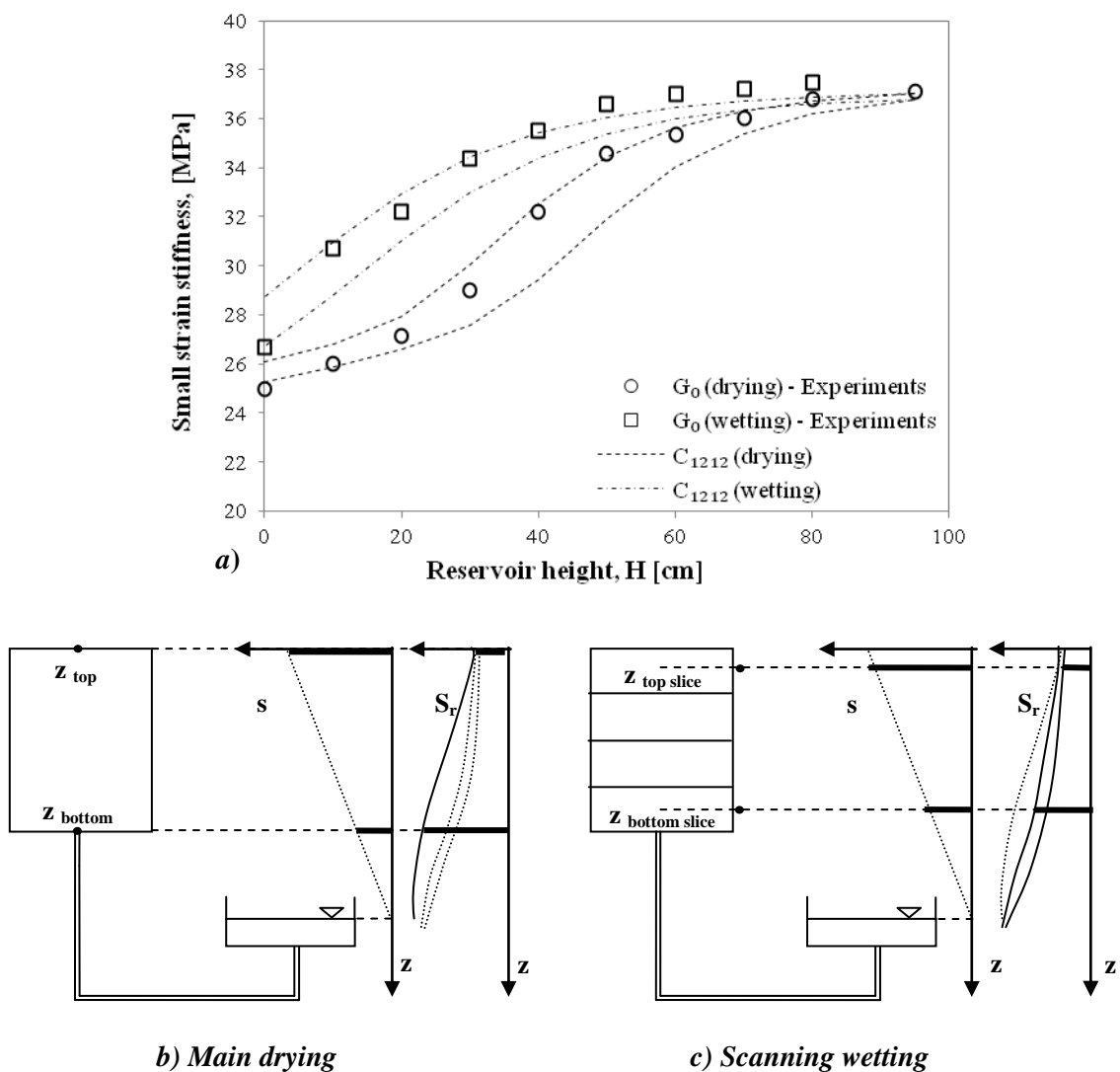
c) Scanning wetting

Figure 2.13. a)Variation of G_0 and upper and lower bounds of C_{1212} during drying-wetting cycle; schematic view of the values of suction and degree of saturation for the calculation of the bounding values of C_{1212} during b) main drying, and c) scanning wetting

2.6. DISCUSSION

The proposed model for small strain shear modulus of unsaturated granular materials was used to elucidate the mechanisms behind different patterns of small strain response in unsaturated granular materials. Two key responses were explored: soils have been observed to exhibit a stiffer behaviour along either a drying or a wetting path and the mechanisms leading to either behaviour are still unclear; furthermore, G_0 has been observed to vary with suction in either a monotonic or non-monotonic fashion. Again, the fundamental mechanisms behind either response have never been expounded.

2.6.1. Influence of the breadth of the water retention curves on the variation of G_0

Let us consider two ideal soils, soil *A* and soil *B*. Let us assume that the soils show the same small strain shear modulus at saturation (G_0^{sat}) and residual state (G_0^{res}). Under these circumstances, the parameters of the proposed model, k_{n0} and σ_i^m, will be the same for the two soils.

Let us now assume that the breadths of the main water retention curves are different for the two soils as an effect, for instance, of their different grain-size distributions. Soil *A* is characterised by a water retention behaviour that develops over a range of suction typical of a coarse-grained soil, whereas the water retention curves of the soil *B* extend over a wider suction range due to the presence of finer particles (*Figure 2.14a*). Let us also assume that the two soils reach the same value of residual degree of saturation, S_r^m.

The small strain stiffness returned by the model for the two soils is shown in *Figure 2.14b*. soil *A* appears to be stiffer upon a wetting path and shows a monotonic variation of G_0 with suction upon both wetting and drying, similarly to the behaviour observed on the

majority of the experimental investigations carried out in the past on unsaturated soils (e.g. Khosravi & McCartney, 2011; Ng, et al., 2009; Ng & Xu, 2012). On the other hand, soil *B* is stiffer upon a drying path and exhibits a non-monotonic variation of G_0 with suction upon both drying and wetting, as observed by other researchers (e.g. Khosravi et al., 2016).

In particular, it is worth noticing that the non-monotonic variation of G_0 with suction, tentatively attributed in the existing literature to coarse-grained soils only (Oh and Vanapalli, 2014; Khosravi et al., 2016), is exhibited here by soil *B* (containing finer particles) rather than soil *A* (coarse-grained soil). This finding suggests that the evolution of G_0 with suction depends on a combination of factors involving the water retention behaviour of the soil, rather than being a direct result of the soil type.

Indeed, the reason for this different behaviour lies on the evolution of the unsaturated intergranular stress during wetting-drying cycles of the two soils. *Figure 2.14c* shows the suction-induced intergranular stress in the bulk water region σ_i^b (saturated contact) and the suction-induced intergranular stress in the meniscus water region σ_i^m (meniscus contact) versus suction. The stress σ_i^b coincides with suction whereas σ_i^m is constant as discussed in the previous section.

For soil *A*, the intergranular stress at the saturated contact never exceeds the intergranular stress at the meniscus contact. Under these conditions, the whole water retention behaviour is contained in a range of suction where the contribution of the menisci to the intergranular stress is always higher than the contribution of suction at the saturated contact. Since the effect of the menisci is more significant along the wetting path, i.e. where the degree of saturation is smaller, the soil exhibits a stiffer behaviour upon wetting.

The picture is different for soil B. The intergranular stress at the saturated contact crosses the value of the intergranular stress generated by the menisci as suction increases. The intergranular stress in the bulk water region becomes higher than the intergranular stress in the meniscus water region as suction increases. As a result, the soil becomes stiffer upon a drying path because the degree of saturation is higher and the region occupied by the bulk water is larger than the region occupied by the menisci. In this case, the variation of G_0 with suction becomes non-monotonic and this is associated with the average intergranular stress initially being dominated by the intergranular stress in the bulk water and then controlled only by intergranular stress associated with the menisci at high suction.
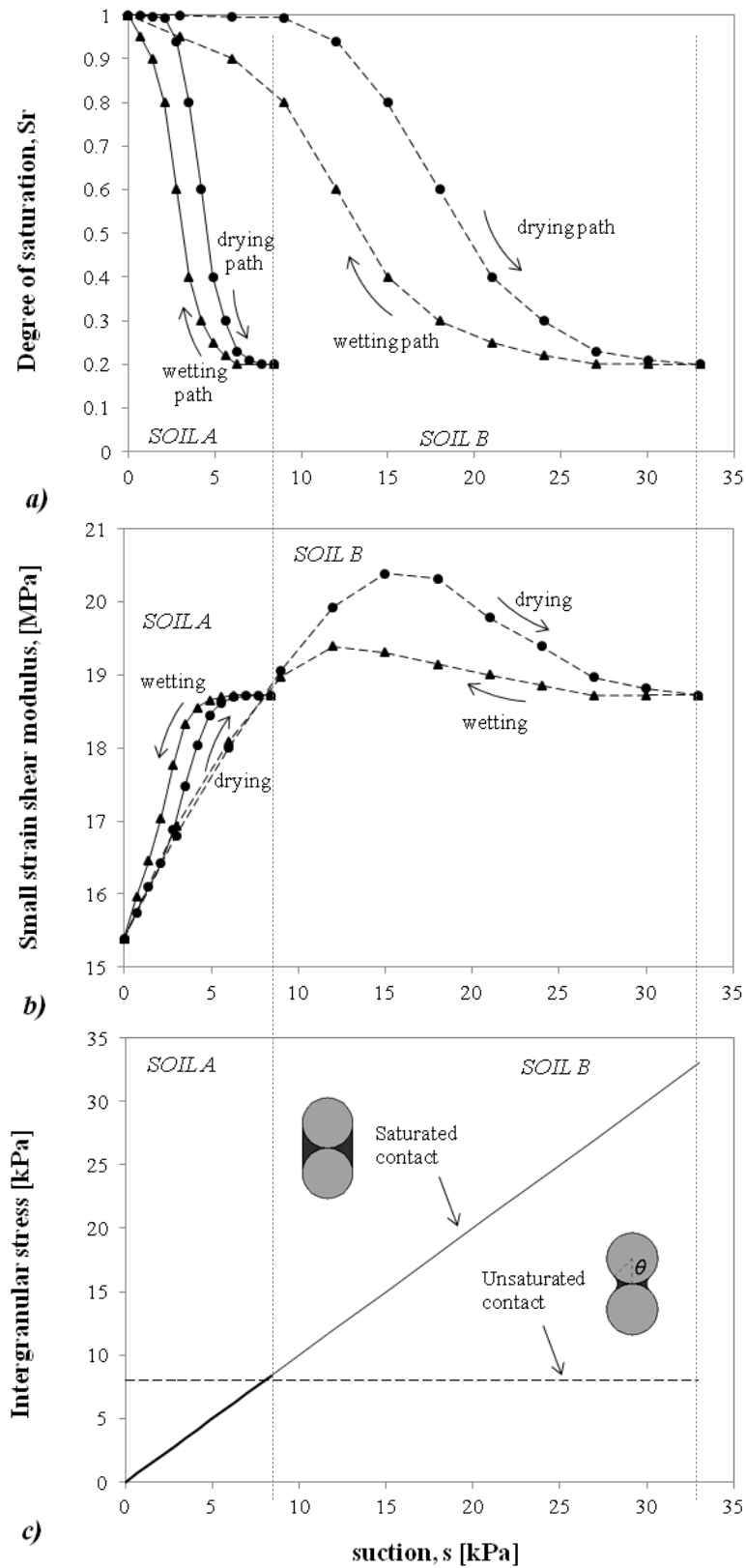
Figure 2.14. Influence of the breadth of the water retention curve on the variation of G_0 for soil A and B : a) water retention curves; b) variation of G_0 with suction; c) variation of intergranular stress with suction

2.6.2. **Influence of meniscus intergranular stress on the variation of G_0**

Let us now consider the case of a loose soil containing fine particles (soil C) and a dense coarse-grained soil (soil D). Although soil D is characterised by the presence of larger particles, its higher density could bring the air-entry suction of soil D to a value similar to soil C, in turn resulting in the same water retention characteristics for the two soils (*Figure 2.15a*). Let us also assume that the two soil exhibit the same value of small-strain shear modulus at saturation (G_0^{sat}) but different values of small-strain shear modulus at residual saturation (G_0^{res}) as a result of the different grain-size distributions. In this case, the parameter k_{n0} will be the same for the two soils, while σ_i^m will assume two different values (higher for the case of finer particles).

Figure 2.15b shows the results of the simulation for soils C and D. Soil C ($\sigma_i^m = 30\ kPa$) exhibits a stiffer behaviour upon wetting, with a monotonic variation of the small strain shear modulus with suction. Soil D ($\sigma_i^m = 5\ kPa$) is instead stiffer upon drying, with a non-monotonic variation of G_0.

Once again, it is demonstrated that the evolution of the small-strain stiffness depends on the evolution of the intergranular stress during hydraulic hysteresis, rather than on the grain-size distribution only. For soil C (containing finer particles), the intergranular stress at the saturated contact (bulk water region) remains smaller than σ_i^m for the whole range of suction (*Figure 2.15c*), causing the soil to be stiffer upon a wetting path and G_0 to increase with suction in a monotonic fashion. For soil D (containing larger particles), the intergranular stress at the saturated contact becomes higher than σ_i^m within the water retention suction range, causing the soil to become stiffer upon a drying path and G_0 to increase with suction in a non-monotonic fashion. The same non-monotonic behaviour observed by Khosravi et al. (2016) for the case of unsaturated sandy soils could therefore

be attributed to a similar evolution of the intergranular stress during hydraulic hysteresis, rather than to the grain-size distribution of the soil.
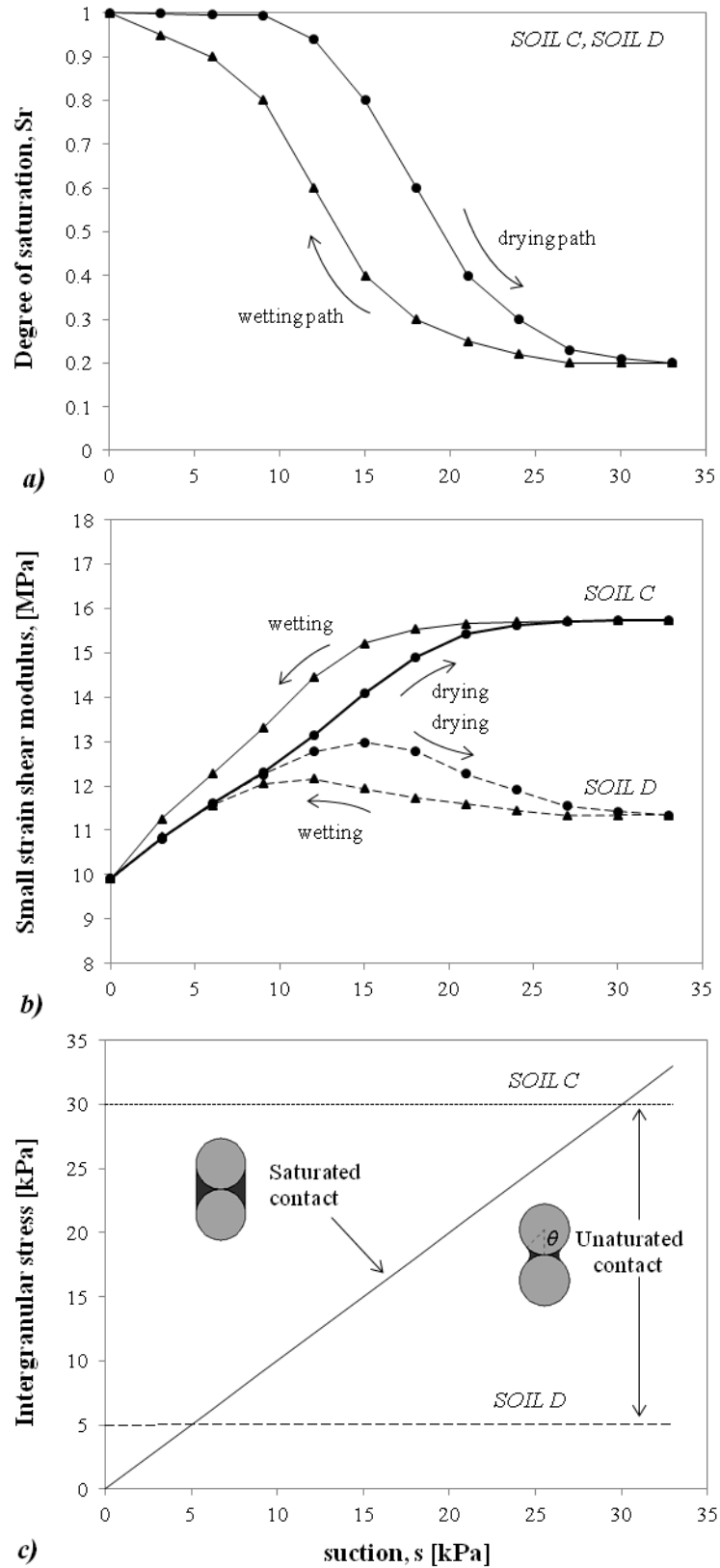
Figure 2.15. Influence of the meniscus intergranular stress on the variation of G_0 for soil C and D : a) water retention curve; b) variation of G_0 with suction; c) variation of intergranular stress with suction

2.7. CONCLUSIONS

The paper has presented a simple conceptual model for the small strain shear modulus of unsaturated granular soils based on a micro-mechanical approach. The model accounts for the independent effect of suction and degree of saturation on soil stiffness. It is based on the knowledge of the water retention curves during wetting-drying cycles, and on two parameters that can be easily calibrated against the small strain stiffness measured at saturation and at residual state. The performance of the model was assessed against experimental data on an unsaturated sand specimen. The soil stiffness simulated by the model along a drying and a wetting path captures the behaviour observed experimentally both at a qualitative and quantitative level. The model captures the higher stiffness observed along a wetting path that the stress variable obtained as the product 'suction times degree of saturation' ('Bishop's' stress) fails to predict.

According to the proposed model, the evolution of G_0 is controlled by the evolution of the unsaturated intergranular stress state over a hydraulic hysteresis loop. In particular, it has been shown that the breadth of the water retention curve and the intensity of the intergranular stress due to the presence of the menisci have an effect on G_0. The combination of these effects can lead to different patterns of G_0 during hydraulic hysteresis.

When the intergranular stress at meniscus contacts is higher than the intergranular stress at saturated contacts and/or the water retention curves develop over a relatively narrow suction range, soil is stiffer during wetting, and the variation of G_0 is monotonic for both drying and wetting paths. When the intergranular stress at meniscus contacts becomes smaller than the one at saturated contacts and/or the water retention curves develop over a

relatively large suction range, the soil becomes stiffer during drying, and the variation of G_0 is non-monotonic.

ACKNOWLEDGEMENTS

3. A DEM INVESTIGATION OF THE MICROMECHANICS OF NON-ACTIVE CLAYS

Submitted for publication to Géotechnique

Arianna Gea Pagano*, Alessandro Tarantino**, Thomas Weinhart*** and Vanessa Magnanimo***

POSITION AND AFFILIATION:
* PhD student, Department of Civil and Environmental Engineering, University of Strathclyde
** Professor, Department of Civil and Environmental Engineering, University of Strathclyde
*** Assistant Professor, Multiscale Mechanics Group, University of Twente

ABSTRACT

The micromechanical interactions between individual couples of clay particles cannot be investigated experimentally in a direct fashion due to the small particle size, as opposed to granular materials. A suitable approach for understanding the mechanical processes occurring at the microscale consists of carrying out indirect experimental investigations by modifying particle-to-particle interactions. On the basis of the indirect experimental evidence, possible inter-particle interactions can be selected and translated into a DEM framework, which in turn can be validated by probing the response of the discrete assembly against the observed macroscopic behaviour. A DEM model was developed in this study with contact laws inferred from indirect experimental evidence at the microscale regarding the mechanical interactions at the edge-to-face contact and the electro-chemical repulsion between particle faces. The adopted contact laws were successfully tested against the ability of the DEM framework to reproduce qualitatively the compression behaviour of clay observed experimentally. Specific aspects of irreversible and reversible compression behaviour were considered, including the effect of different pore-fluid chemistry (pH and dielectric permittivity). The contact laws presented in this work were intentionally simple

(i.e. piecewise linear functions) to explore their potential for capturing the main features of the macroscopic response of non-active clays and, hence, corroborating the underlying micromechanical concept.

3.1. INTRODUCTION

The macroscopic response of geomaterials is controlled by the processes occurring at the microscale (i.e. the interplay between inter-particle forces and particle arrangements). Understanding these processes is key to interpret experimental data and to inform 'continuum' macroscopic constitutive models.

For the case of granular materials, microscale processes at the contact between couples of particles have been directly investigated in terms of the interparticle forces (Cavarretta, et al., 2010) and particle kinematics (Andò, et al., 2012a; Andò, et al., 2012b). The microscopic mechanisms observed experimentally can therefore be translated into Discrete Element Method (DEM) models, which have been widely used as a virtual laboratory to investigate fundamental aspects of the behaviour of granular materials (O' Sullivan, et al., 2006), including strain localisation (Kawamoto, et al., 2018; Iwashita & Oda, 1997), induced anisotropy (Guo & Zhao, 2012), crushing (Thornton, et al., 1996; Cheng, et al., 2003; Bolton, et al., 2008), wave propagation and small strain stiffness (Mouraille, 2009; O'Donovan, et al., 2012).

On the other hand, microscale processes in clays cannot be directly investigated due to the small size of individual clay particles. Inter-particle forces in clays may be electro-chemical in nature, in contrast to the conventional mechanical interactions that characterise granular materials. Due to the lack of direct observations of such interactions, the choice

and implementation of suitable contact laws into DEM models for the case of clayey geomaterials is not straightforward.

DEM simulations of clay behaviour have been performed by Anandarajah and his co-workers (Anandarajah & Chen, 1997; Anandarajah, 2000; Yao & Anandarajah, 2003; Anandarajah & Amarasinghe, 2012). For the case of non-active clay, Anandarajah assumes that particles possess a uniform negative charge, and that attraction between particles is driven only by the short-range van der Waals forces (Anandarajah, 2000). By adding these contributions to the conventional mechanical inter-particle interactions, the authors obtained numerical results that compared reasonably well with the soil behaviour observed in the laboratory. A criticism of the assumption made by Anandarajah and co-workers is that interparticle force-displacement constitutive laws are built on a purely theoretical basis, with no direct experimental evidence of their validity at the microscale. Furthermore, the 'activation' of van der Waals forces is difficult to justify for the average inter-particle distances occurring in natural clays.

Microscopic mechanisms occurring in clays have been investigated indirectly by Pedrotti and Tarantino (2017) using a combination of Mercury Intrusion Porosimetry (MIP) and Scanning Electron Microscope (SEM). From the experimental data, they inferred that particle edges are charged positively for an acidic pore-fluid (as is the case of ordinary laboratory water) and particle faces are charged negatively. Reversible and non-reversible microscopic mechanisms resulting from the charge distribution on clay particles were then described in a conceptual micro-mechanical model. In the absence of direct experimental evidence, a step forward in the investigation of the microscale mechanisms would consist of selecting possible inter-particle interactions, translating them into a DEM

framework, and probing the response of the discrete assembly against macroscopic clay behaviour.

This paper presents a DEM validation of the micro-scale mechanisms inferred by Pedrotti and Tarantino. To this end, a numerical DEM framework to simulate aggregates of clay particles is introduced in this work. Constitutive contact laws were designed on the basis of the conceptual micro-mechanical model. Assemblies of spherical primary units were created to form rod-shaped particles in a pseudo-2D environment (3D particles in a 2D displacement field) using the open source C++ code MercuryDPM (http://www.mercurydpm.org/). Attractive and repulsive long-range forces were added to the contact laws in order to simulate the positive/negative charge characterising the clay particle surface. Each rod was designed to behave as a single unit thanks to an additional 'bonding' interaction, which is able to stick together spheres belonging to the same rod.

The contact laws were tested against the ability of the DEM framework to reproduce qualitatively some aspects of the compression behaviour of clay observed experimentally. These include the effect of the pore-fluid chemistry (pH and dielectric permittivity) on the virgin loading and unloading-reloading lines, and the dependency of the slope of the unloading-reloading compression curves on the pre-consolidation stress. The contact laws presented in this work were intentionally kept simple to explore their potential to capture the main features of the macroscopic response of 'non-active' clay and, hence, corroborate the underlying micro-mechanical concept.

3.2. BACKGROUND: CONCPETUAL MICRO-MECHANICAL MODEL FOR NON-ACTIVE CLAYS

Pedrotti and Tarantino (2017) formulated a conceptual micro-mechanical model describing the mechanisms underlying reversible and non-reversible compression of non-active clays. The conceptual model was based on the results of an extensive experimental investigation into the microscopic and macroscopic behaviour of kaolinite, including Mercury Intrusion Porosimetry (MIP), Scanning Electron Microscope imaging (SEM) and oedometer tests.

The model was based upon the assumption that both mechanical and electro-chemical forces affect inter-particle interactions. Coulombian forces, due to the presence of permanent charges on the surface of clay particles, were assumed to be the only electro-chemical forces controlling the interaction between clay particles. Particle faces were assumed to be negatively charged due to isomorphic substitution of cations, whereas particle edges were assumed to be either negatively or positively charged depending on whether the pH is alkaline or acidic respectively. A schematic representation of the microscopic mechanisms inferred by Pedrotti and Tarantino is shown in *Figure 3.1*.
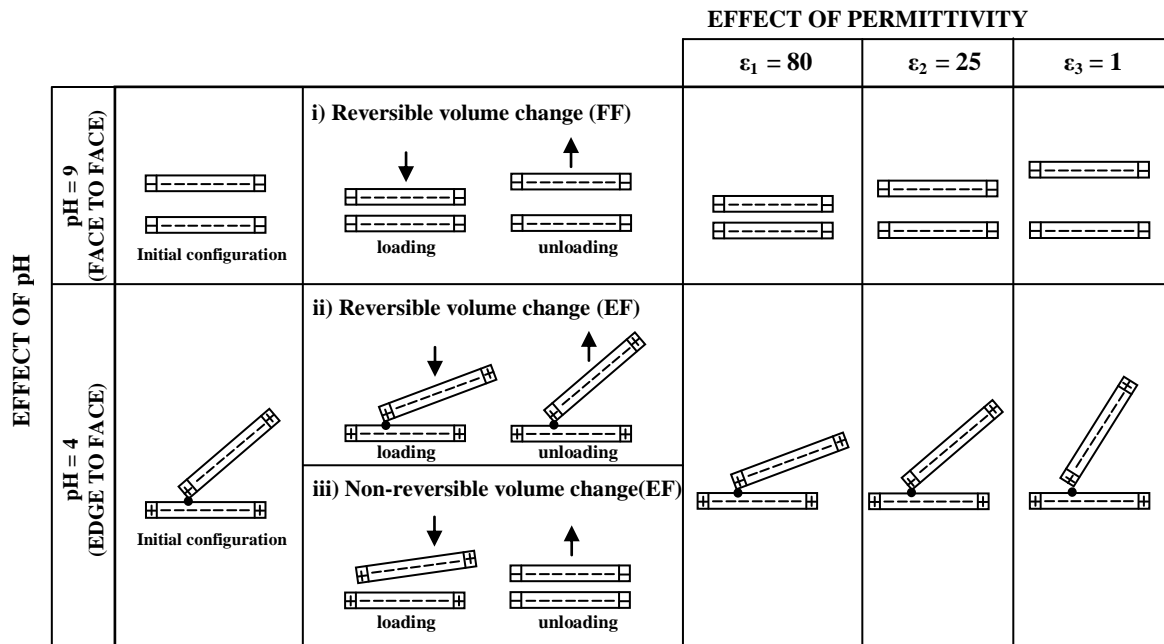
Figure 3.1. Schematic representation of the conceptual micromechanical model by Pedrotti & Tarantino (2017)

For an alkaline pore-fluid, the negative charge of both particle faces and edges generates a repulsive Coulombian force, preventing particles from creating a contact and resulting in a sub-parallel 'face-to-face' configuration. In this case, an increase or decrease of external load was assumed to generate only reversible volume change (mechanism 'i' in *Figure 3.1*).

For an acidic pore-fluid, the positive charge of the particle edges and the negative charge of the particle faces were assumed to generate an attractive Coulombian force, resulting in the creation of 'edge-to-face' contacts between particles. This type of contact was assumed to cause both reversible and non-reversible micro-mechanisms. Reversible mechanisms refer to the case when particles in contact, subjected to loading or unloading, tilt with respect to each other with no contact disengagement (mechanism 'ii' in *Figure 3.1*). On the other hand, non-reversible volume change was attributed to the loss of edge-

to-face contacts (i.e. slippage or normal detachment) due to external loading (mechanism 'iii' in *Figure 3.1*). After contact disengagement, particles were assumed to dispose in a sub-parallel 'face-to-face' configuration and, hence, give rise to reversible mechanisms only.

Finally, for both edge-to-face and face-to-face configurations, the magnitude of the repulsive Coulombian interaction controlling the distance between particles during loading/unloading reversible paths was assumed to be controlled by the dielectric permittivity of the pore-fluid, ε. In particular, small values of the dielectric permittivity of the pore-fluid (e.g. air) were assumed to give rise to high repulsive/attractive interactions, and vice-versa.

3.3.   DISCRETE ELEMENT METHOD FRAMEWORK

In this work, the Discrete Element Method (Cundall & Strack, 1979) was used to simulate the behaviour of a non-active clay subjected to 1-D loading and unloading. DEM analyses describe the particle-to-particle interactions occurring within particle aggregates. In basic DEM models, particles are modelled as disks (2-D analysis) or spheres (3-D analysis). The contact forces and torques acting on each particle (either due to the interaction with other particles or due to the interaction with the domain boundaries) at the beginning of the analysis have to be selected as the basic input. Once the forces and torques are known, the dynamic motion of the particles is determined by integrating Newton's equations of motion for the translational and rotational degrees of freedom.

The simplest contact model describing the normal mechanical interaction between pairs of spherical particles, f_{ij}^n, involves a linear-elastic repulsive force (particles repel each

other with no energy loss) and a linear dissipative force (acting against the relative velocity and resulting in a loss of energy), as in Luding (2008):

$$f_{ij}^n = \begin{cases} 0, & \delta_{ij}^n \leq 0 \\ k_n \delta_{ij}^n + \gamma_n v_{ij}^n, & \delta_{ij}^n > 0 \end{cases} \qquad 1$$

where δ_{ij}^n and v_{ij}^n are the normal overlap and the normal relative velocity between sphere i and sphere j respectively (taken on the line connecting the centres of the spheres), k_n is the normal stiffness at the contact, and γ_n is the damping coefficient. A non-zero tangential interaction f_{ij}^t can also be considered, arising when spheres in contact ($\delta_{ij}^n > 0$) experience a relative displacement in the tangential direction:

$$f_{ij}^t = \begin{cases} 0, & \delta_{ij}^n \leq 0 \\ k_t \delta_{ij}^t + \gamma_t v_{ij}^t, & \delta_{ij}^n > 0 \\ \mu f_{ij}^n, & \left| k_t \delta_{ij}^t \right| > \mu f_{ij}^n \end{cases} \qquad 2$$

where k_t is the tangential stiffness at the contact, δ_{ij}^t and v_{ij}^t are the relative tangential displacement and the relative tangential velocity respectively, γ_t is the tangential damping coefficient, and μ is the friction coefficient. The tangential contact model can be extended to the rotational degree of freedom by introducing a rolling resistance f_{ij}^{ro}, calculated by substituting the terms δ_{ij}^t, k_t, v_{ij}^t and γ_t in Equation 2 with the relative rotation δ_{ij}^{ro}, the rolling stiffness k_{ro}, the rolling velocity v_{ij}^{ro} and the rolling damping coefficient γ_{ro} respectively.

Starting from the basic interactions described in Equations 1 and 2, two specific aspects of clay DEM modelling were addressed in this study: a) the creation of elongated particles rather than spherical particles, and b) the introduction of additional inter-particle interactions to simulate the effect of the positive/negative charge carried by clay particles.

3.3.1. **Modelling elongated rod-like clay particles**

Kaolin clay particles naturally occur as small hexagonal-shaped elements, with particle sizes usually falling in the range $0.1 - 10$ μm. Particles are typically elongated, and the ratio between the thickness of a particle and its main dimension is usually around 1/10 (Mitchell & Soga, 2005). In 2D analyses, kaolin particles can therefore be schematised as rod-like elements, having a 1-to-10 ratio between thickness and length.

In this study, spheres were used to create rod-like particles constrained so as to move in a plane (pseudo-2D framework). Each sphere represents an elementary DEM particle, i.e. initial information such as dimensions and density were assigned individually to each sphere, as well as the contact law parameters. However, an additional attractive force was introduced to 'bond' together groups of spheres into single rod-like particles:

$$f_{bond} = k_n\, \delta_{bond} \qquad\qquad\qquad 3$$

where f_{bond} is the attractive force bonding together spheres in the same rod, k_n is the normal stiffness at the contact (as for Equation 1), and δ_{bond} is the desired overlap between spheres belonging to the same rod (input parameter). Therefore, although each sphere was treated separately as an elementary unit, each group of spheres forming a rod behaved as a single elongated particle (similarly to crushable particles or deformable agglomerates modelled by Thornton, et al. 1996, Cheng, et al. 2003, Bolton, et al. 2008, Ueda et al. 2013, Asadi et al., 2018).

For the sake of simplicity, equal rods of 19 spheres were considered in this study (*Figure 3.2*). The overlap δ_{bond} was taken as being equal to the radius of each sphere, in order to obtain a thickness-to-length ratio for each rod equal to 1/10. The properties of the elementary spheres used in this work are given in *Table 3.1*. The assigned properties

yielded a constant collision time t_c = 2.6e-9 s and a restitution coefficient equal to 0.9. A

constant time step taken as $\Delta t = 0.02 t_c$ could therefore be used.
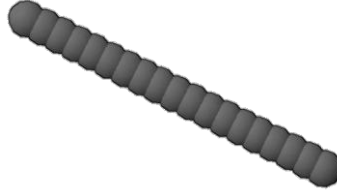
Figure 3.2. Rod-like particle created using MercuryDPM

INPUT PARAMETER		VALUE (SI units)
Sphere density	D	2605 kg/m³
Sphere radius	R	0.5e-6 m
Spheres per rod	$N_{s,rod}$	19
Number of spheres	N_s	5700
Number of rods	N_{rods}	300
Bonding overlap	δ_{bond}	0.5e-6 m
Threshold overlap	$\delta_{ij}^{n,*}$	0.5e-6 m
Normal stiffness	k_n	1e3 N/m
Tangential stiffness	k_t	$2/7 k_n$
Rolling stiffness	k_{ro}	$2/5 k_n$
Friction	μ	0.3
Normal damping coefficient	γ_n	5.7e-8 kg/s
Tangential damping coefficient	γ_t	$2/7 \gamma_n$
Rolling damping coefficient	γ_{ro}	$2/5 \gamma_n$
Background dissipation (relaxation)	Γ_{rel}	3.16e-9 kg/s
Background dissipation (compression)	Γ	3.16e-10 kg/s

Table 3.1. Properties of the elementary spheres.

3.3.2. Constitutive contact law between pairs of clay particles

In the present study, elementary spheres belonging to different rods were designed to interact with each other via a purposely formulated constitutive contact law. The approach adopted in this work was to obtain the total normal force acting at the contact as the sum of a mechanical component and an electro-chemical component. A schematic representation of the normal and tangential contact laws introduced in this study is shown in *Figure 3.3*.
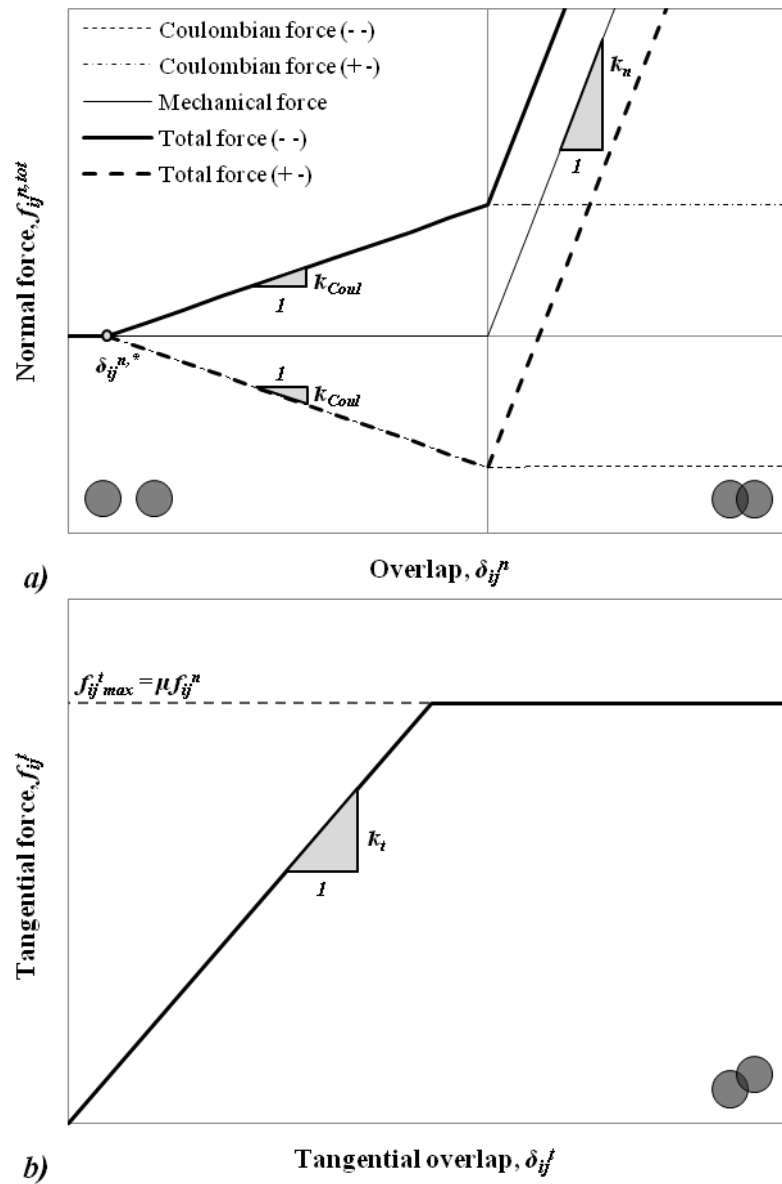
Figure 3.3. Normal and tangential contact laws (sphere-to-sphere interaction) for the simulation of clay particles.

The mechanical component was modelled via the linear elastic-dissipative contact model in Equation 1, reported in *Figure 3.3a* as 'Mechanical force'. The values of k_n, k_t, k_{ro} and μ adopted in this work were assumed to be independent of the nature of the pore-fluid and are reported in *Table 3.1*. The selected values of k_n, k_t and k_{ro} guaranteed the simulation of 'stiff' particles in the pressure range explored in this study (i.e. the ratio between the stiffness at the contact and the particle diameter is several orders of magnitude higher than the maximum applied pressure).

The electro-chemical component was modelled by introducing a long-range inter-sphere repulsive/attractive force. The pattern of the electro-chemical component of the normal force is reported in *Figure 3.3a* as 'Coulombian force'. The long-range Coulombian interaction, $f_{ij,Coul}^{n}$, arises for negative values of the overlap (representing the distance between spheres not in contact) once a fixed threshold value is exceeded, and remains constant after overlapping occurs:

$$f_{ij,Coul}^{n} \qquad\qquad\qquad\qquad 4$$

$$= \begin{cases} 0, & \delta_{ij}^{n} < \delta_{ij}^{n,*} \\ \pm\, k_{Coul}(\delta_{ij}^{n,*} - \delta_{ij}^{n}), & \delta_{ij}^{n,*} < \delta_{ij}^{n} < 0 \\ \pm\, k_{Coul}(\delta_{ij}^{n,*}), & \delta_{ij}^{n} > 0 \end{cases}$$

where $\delta_{ij}^{n,*}$ is the threshold overlap, and k_{Coul} is the normal stiffness of the long-range Coulombian interaction. The Coulombian force is positive (repulsive) when spheres i and j carry the same charge and is negative (attractive) when spheres i and j carry opposite charges. Changing the sign of the Coulombian force allows for simulation of alkaline/acidic pore-fluid. Changing the value of k_{Coul} allows for simulations of pore-fluids with different dielectric permittivity. Values of the normal Coulombian stiffness k_{Coul} for the simulation of different pore-fluids were selected following a rigorous

calibration procedure against experimental results. This procedure is described later in Section 4.3. It is worth noticing that, as for Pedrotti & Tarantino (2017), Coulombian forces were assumed to be the only electro-chemical forces controlling the interaction between particles not yet in contact. However, the constitutive contact law could be easily extended to more complex contact interactions, e.g. including van der Waals forces, by considering additional attractive forces in the $\delta_{ij}^n < 0$ range.

The total normal force acting at the contact is then obtained by adding together the mechanical and electro-chemical contributions given by Equation 1 and Equation 4 respectively ('Total force' in *Figure 3.3a*):

$$f_{ij}^{n,tot} = f_{ij}^n + f_{ij,Coul}^n$$

<div align="right">5</div>

Once the total force at each contact is calculated and the instantaneous position of the particles is known, macroscopic variables such as the distribution of the stress in the assembly could be extracted from the discrete data via the *coarse-graining* micro-macro transition method implemented in MercuryDPM (Tunuguntla, et al., 2015).

3.3.3. Design of clay-like particles

Two types of particles were designed in this work as shown in *Figure 3.4*. Particles that are negatively charged on both edge and face (alkaline pore fluid) were generated by assigning a negative charge to all the spheres belonging to each rod, resulting in the development of only repulsive long-range forces between rods interacting with each other. Particles that are negatively charged on the face and positively charged on the edge (acidic pore fluid) were generated by assigning a negative charge to the inner spheres of each rod and a positive charge to the end spheres. This choice resulted in the formation of edge-to-face

contacts between rods, driven by the attractive force developing between positively charged edges and negatively charged faces.
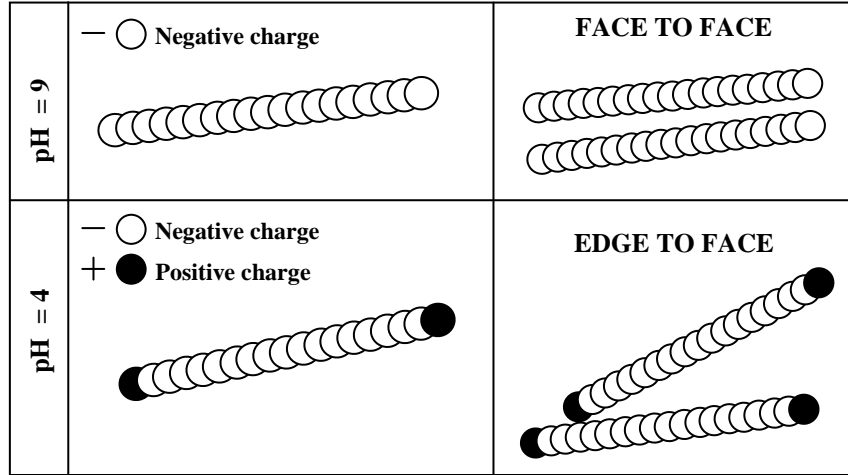
Figure 3.4. Design of clay-like particles: alkaline pH (FF configuration) and acidic pH (EF configuration).

3.4. NUMERICAL PROCEDURES

3.4.1. Specimen preparation

DEM simulations were performed on assemblies of N_{rods}= 300 rods, amounting to a total number of spheres equal to 5700. The effect of the sample size was tested by performing preliminary tests on specimens with different number of rods. Results were found to be independent of the rod number for N_{rods}> 250.

Initial configurations were created by placing the rods in a square domain in the *x-z* plane, with their long axis along the *x*-direction. The domain boundaries were taken as solid walls. The characteristics of the particle-to-wall interaction were assumed to be equal to the mechanical particle-to-particle interaction (however, no charge was assigned to the walls). The *x* and *z* coordinates of the centre of the first sphere forming each rod were assigned randomly, while a constant *y* coordinate was assigned to the centres of all the

spheres and remained unchanged during the entire simulation. The initial size of the domain was selected in order to obtain a specimen in a gas-like state, i.e. with an initial void ratio $e = 20$ and rods not interacting with each other. The void ratio of the specimen is intended here as the area fraction, i.e. the ratio between the area occupied by the voids and the area occupied by the solids obtained by projecting the rods onto the *x-z* plane.

Once the 'gas' specimen was created, a constant displacement rate was assigned to the top and right walls, and a position-dependent displacement rate was assigned to the particles in order to compress the specimen isotropically. The movement was stopped when the material experienced a fluid-solid transition, i.e. the virtual specimen was able to carry an external load. The signature of the transition is given by non-zero values of stress and of the average number of contacts (including electro-chemical long-range contacts) within the specimen.

Once a 'solid' specimen was obtained, the assembly was subjected to a relaxation stage. The boundaries were kept stationary and the particles were left to relax towards an equilibrium configuration. In order to expedite the relaxation stage, an additional global background dissipation (reported in *Table 3.1*) proportional to the particle velocity was introduced. The relaxation stage was stopped when the kinetic energy of the sample was found to be at least five orders of magnitude smaller than the elastic energy.

3.4.2. 1-D compression and unloading

After relaxation, a one-dimensional compression of the specimen in the *z*-direction was carried out by lowering the top boundary wall in order to simulate oedometric conditions. During this stage, the void ratio and the vertical stress state of the specimen were

calculated at regular intervals in order to obtain a compression curve. Both loading (compression) and unloading (rebound) were performed during the analysis.

The one-dimensional loading and unloading paths were performed in a displacement-controlled mode during the simulation, i.e. by lowering or raising the top wall while the vertical stress σ_z' of the specimen was measured. A background dissipation (smaller than the one used for relaxation) was also added (*Table 3.1*).

During both loading and unloading paths, the displacement rate assigned to the top boundary (corresponding to a displacement of 1.6e-5 µm for each time step) was maintained small enough to ensure a quasi-static process. To this end, the displacement rate was selected by performing the same loading/unloading paths at different displacement rates and identifying the maximum displacement rate below which the output of the simulation became independent of the displacement rate itself. The addition of the background dissipation allowed to increase the displacement rate without affecting the results, thus reducing the total simulation time.

3.4.3. Calibration of the Coulombian normal stiffness

In order to reproduce the response of the clay specimens during 1-D compression, the parameters that characterise the Coulombian contact law need to be defined depending on the nature of the pore-fluid. The threshold overlap $\delta_{ij}^{n,*}$ was tentatively selected as 1/2 of the rod thickness (i.e. equal to the radius of the spheres) and assumed to be independent of the nature of the pore-fluid. On the other hand, the value of the normal stiffness of the Coulombian interaction k_{Coul} was varied depending on the dielectric permittivity of the pore-fluid.

For the case where the pore-fluid is water, the parameter k_{Coul}^{water} was calibrated to match the void ratio at the end of the specimen preparation stage with the void ratio measured experimentally at quasi-zero vertical stress when using ordinary laboratory water as the pore-fluid (Pedrotti and Tarantino 2017).

The Coulombian normal stiffness in the presence of air and acetone, i.e. the other two pore-fluids tested by Pedrotti and Tarantino (2017), were derived by assuming that the Coulombian normal stiffness is inversely proportional to the dielectric permittivity of the pore-fluid. As a result, the Coulombian normal stiffness in air and acetone can be derived from the stiffness in water as follows:

$$k_{Coul}^{air} = k_{Coul}^{water} \frac{\varepsilon^{water}}{\varepsilon^{air}} \qquad\qquad 6$$

$$k_{Coul}^{acetone} = k_{Coul}^{water} \frac{\varepsilon^{water}}{\varepsilon^{acetone}} \qquad\qquad 7$$

where ε^{air}, $\varepsilon^{acetone}$ and ε^{water} are the dielectric permittivity values of air, acetone and water respectively ($\varepsilon^{air} = 1$, $\varepsilon^{acetone} = 25$, and $\varepsilon^{water} = 80$).

3.5. NUMERICAL RESULTS AND DISCUSSION

Four sets of simulations were performed in this study by changing the contact law parameter k_{Coul} and the sign of the charge assigned to the spheres. These simulations were aimed at reproducing the experimental compression behaviour of the kaolin clay specimens tested by Pedrotti and Tarantino (2017) by considering pore-fluids with different dielectric permittivity (air, acetone, and water) and different pH (acidic pH=4 and alkaline pH=9).

The association between the experimental tests and the numerical simulations is given in *Table 3.2*. Particle edges were given a positive charge in Simulations 1, 2 and 3 to generate an edge-to-face configuration as observed experimentally in Tests 1, 2, and 3 for the case of air, acetone, and acidic water respectively. Particle edges were given a negative charge in Simulations 4 to generate a face-to-face configuration as observed experimentally in Test 4 for the case of alkaline water.

	Pore fluid	Dielectric permittivity		pH
TEST 1	Air (dry powder)	ε^{AIR}	1	-
TEST 2	Acetone	$\varepsilon^{ACETONE}$	25	-
TEST 3	Water	ε^{WATER}	80	4
TEST 4	Alkaline water			9

	Coulombian stiffness [N/m]		Edge charge	Face charge
SIMULATION 1	$k_{Coul}{}^{AIR}$	40	+	-
SIMULATION 2	$k_{Coul}{}^{ACETONE}$	1.6	+	-
SIMULATION 3	$k_{Coul}{}^{WATER}$	0.5	+	-
SIMULATION 4			-	-

Table 3.2. Association between experimental tests and numerical simulations.

3.5.1. Validation of the contact law for clays

The core of the contact law for clays is represented by the Coulombian force, which was added to the traditional mechanical force implemented in granular DEM analyses. In turn, the Columbian force was designed based on the assumption that its magnitude and sign depend on the dielectric permittivity of the pore-fluid and on the pH. The contact law can

therefore be probed by analysing the response of the DEM model when simulating different permittivity and pH values for the pore-fluid.

Figure 3.5 shows the values of the simulated initial void ratio e_0 at the end of the preparation stage for all simulations. According to the calibration procedure previously described, the initial void ratio for the case of water at pH = 4 (Simulation 3) obviously matches the void ratio measured experimentally at quasi-zero vertical stress. The striking result is that the void ratio is matched reasonably well at a quantitative level also for the other pH/dielectric permittivity scenarios. The initial void ratio matched almost perfectly for the case of the edge-to-face configuration (Simulation 1 and 2). For the case of the face-to-face configuration (Simulation 4), the substantial reduction in the initial void ratio caused by the de-activation of most of the edge-to-face contacts for the case of alkaline pore-fluid is also well captured. There is indeed a slight underestimation of the void ratio by the DEM simulation. This may be due to the fact that the variation of pH from 4 to 9 in real clay specimens is unlikely to cause the deletion of all the positive edge charges, resulting in a slightly more open structure due to residual edge-to-face contacts. In contrast, all particle edges were given a negative charge in the DEM simulation.
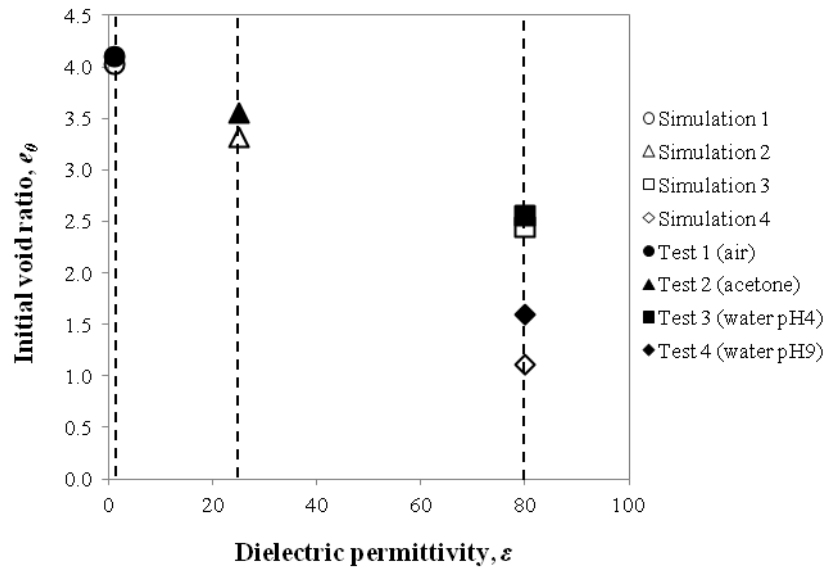
Figure 3.5. Initial void ratio at the end of the specimen preparation (● ▲ ■ ♦ : experimental results from Pedrotti and Tarantino (2017); ○ Δ □ ◊ : simulation results).

The ability to predict the initial configuration of the specimen at a quantitative level in terms of void ratio by relating a microscopic quantity (k_{Coul}) with a macroscopic quantity (ε) is the first demonstration of the validity of the DEM model to capture some aspects of the macroscopic behaviour of clayey materials, even using a very limited set of contact law parameters.

3.5.2. Effect of pre-consolidation stress on 'elastic' response upon unloading

Wide experimental evidence shows that the unloading-reloading lines of clay specimens in the plane void ratio - effective vertical stress ($e - log\sigma_z'$) are not parallel but increase their slope as the pre-consolidation stress increases. This is also the case for the specimens saturated with ordinary laboratory water and subjected to standard oedometer tests (Pedrotti and Tarantino, 2017) in *Figure 3.6*.

The DEM model was therefore challenged for its capability to capture the effect of the pre-consolidation stress on the elastic behaviour upon unloading/reloading. *Figure 3.7* shows the results from Simulation 3. Three unloading paths were performed in the DEM analysis. As for the experimental observation, the increase in slope of the unloading paths with the maximum vertical stress experienced by the assembly before unloading appears to be captured satisfactorily.
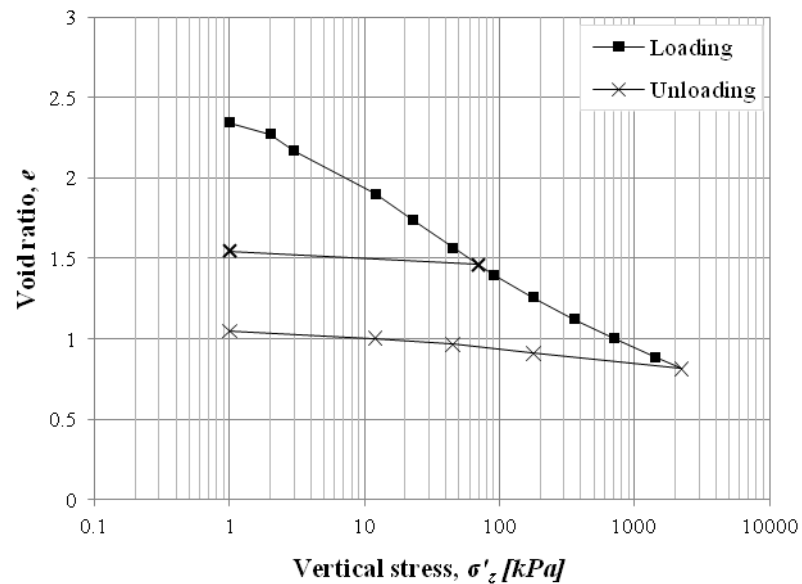
Figure 3.6. Test 3: mono-dimensional compression of kaolin mixed with water, pH= 4 (Pedrotti & Tarantino, 2017).
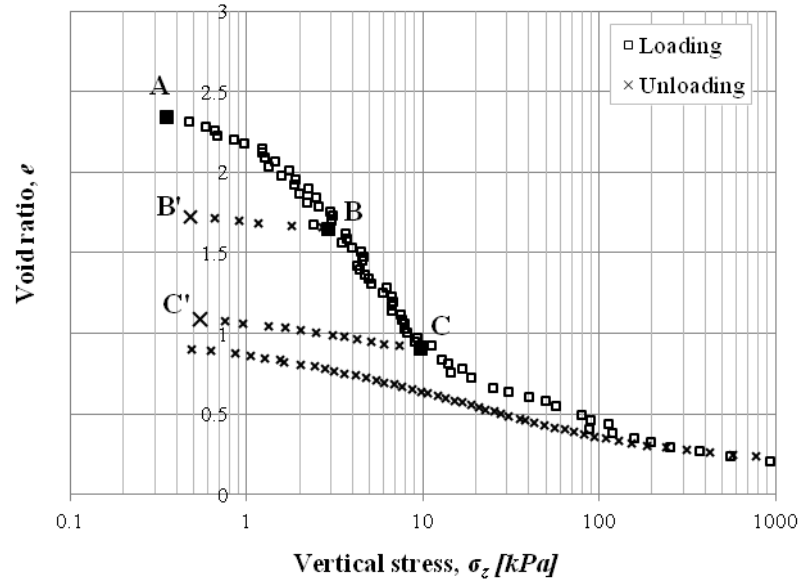
Figure 3.7. Numerical results of Simulation 3 (E+, F-, $k_{Coul} = k_{Coul}^{water}$).

It should be noted that the DEM simulation cannot be compared quantitatively with the experimental compression curve. The range where the void ratio appears to be linear in a semi-log scale ($e - log\sigma_z'$) extends up to 10 kPa in the DEM simulation, whereas the experimental data shows that this range is equal to or greater than 2000 kPa. Furthermore, simulated kaolin particles have been observed to bend significantly after the 10 kPa range is exceeded (as shown later in *Figure 3.12*), suggesting that the response of the model at high stress may be unreliable. The experimental compression curve should therefore be compared with the linear branch of the compression curve (in a semi-log plot) derived from the DEM simulation. The mismatch in the vertical stress can be attributed to the simplifications introduced in this DEM analysis. For instance, the Columbian interaction and mechanical interaction of the contact law were designed as piecewise linear functions as this work is mainly aimed at exploring the potential of the DEM model to capture the main features of the macroscopic response of non-active clay, thus corroborating the micro-mechanical concepts underlying the DEM model. The mechanical interaction

between spheres in contact and the electro-chemical interaction between spheres having the same (negative) charge is more complex than the linear one adopted in this work. A Hertzian contact law and a function that reproduces the DLVO theory (combined effect of van der Waals and double layer forces) would in principle be more appropriate. However, highly non-linear contact laws would make the computational times prohibitive when considering the high number of particles (and, hence, spheres) required to represent adequately the elementary volume.

It is interesting to exploit the DEM model to explore the micro-mechanisms controlling the response observed in *Figure 3.6* and *Figure 3.7. Figure 3.8* shows the configuration of the specimen at different stages of the loading- unloading process (as also shown in *Figure 3.7*): state A represents the state at the end of the preparation stage, state B and C represent states on the virgin compression line at two different values of pre-consolidation stress, and B' and C' represent two states at the end of unloading.

ii) Rotation of particles in EF

i) Compression of particles in FF

iii) EF disengagement

a) **A** : *e=2.34, σ$_z$=0.35 kPa*   **B** : *e=1.70, σ$_z$=3.00 kPa*   **C** : *e=0.91, σ$_z$=10.01 kPa*

Small elastic rebound of EF and FF

b) **B** : *e=1.70, σ$_z$=3.00 kPa*   **B'** : *e=1.74, σ$_z$=0.5 kPa*

High elastic rebound of FF

Unaltered EF

c) **C** : *e=0.91, σ$_z$=10.00 kPa*   **C'** : *e=1.09, σ$_z$=0.55 kPa*
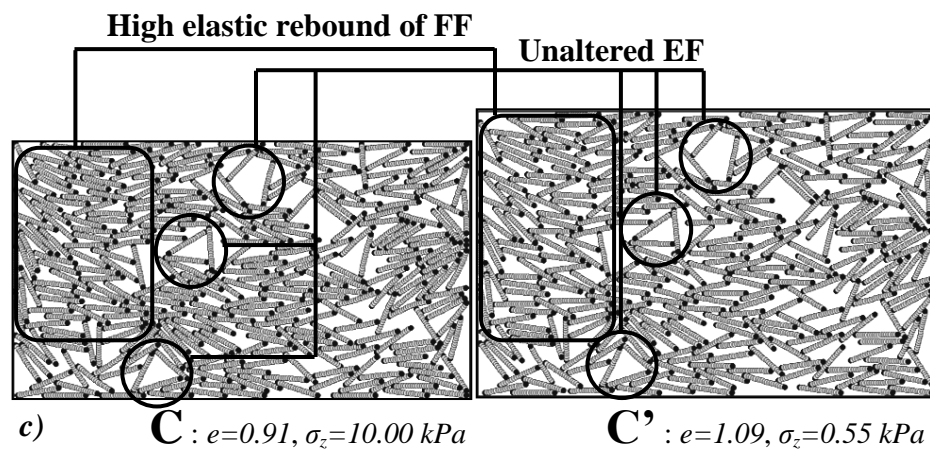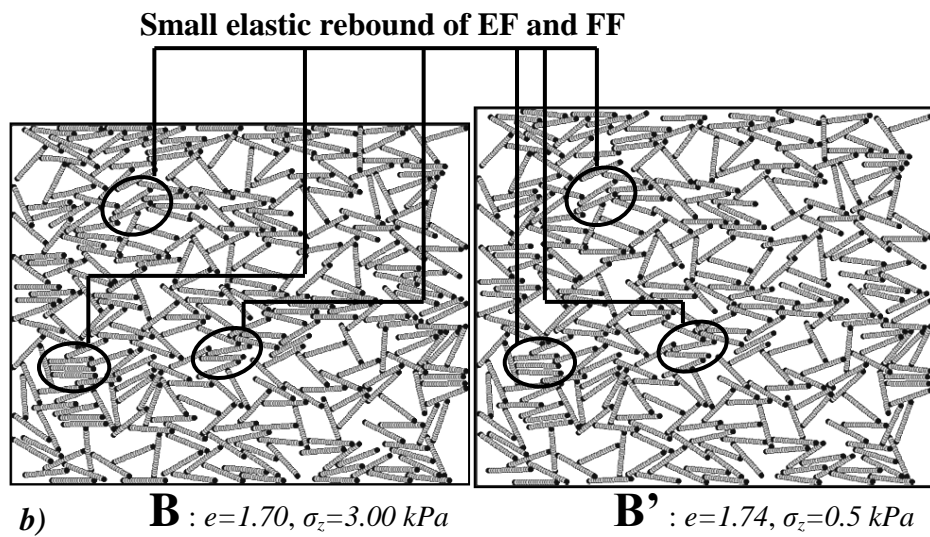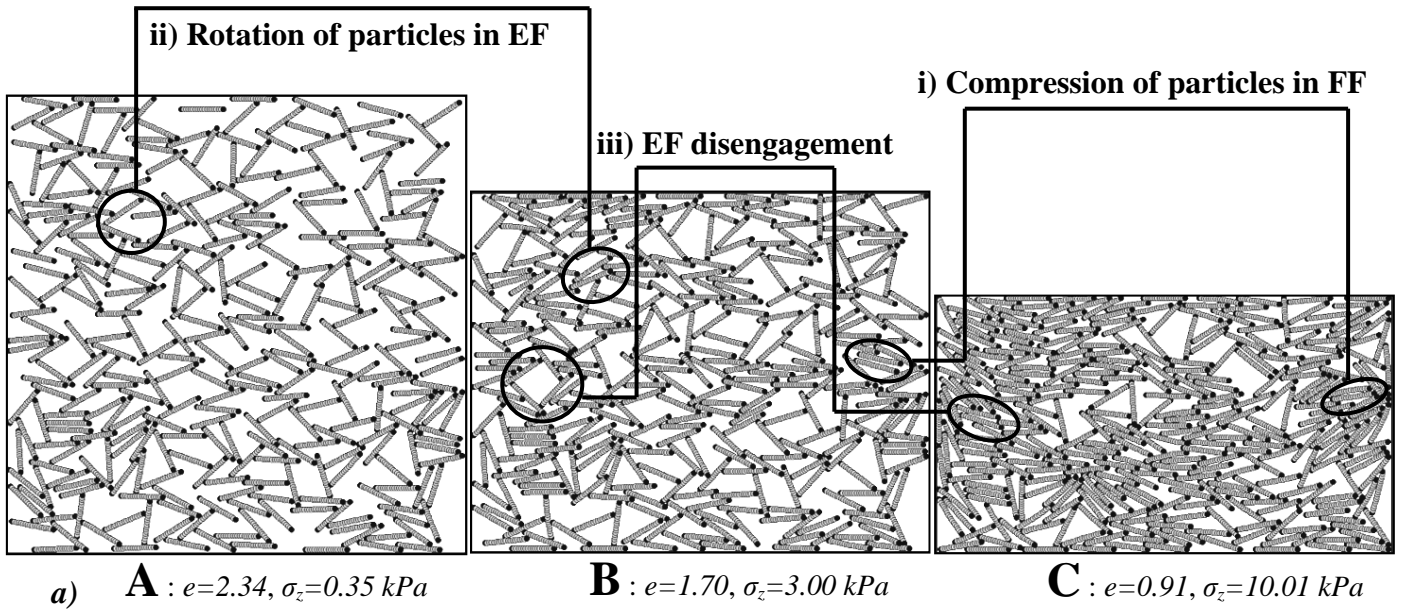
Figure 3.8. Different specimen configurations from Simulation 3 (E+, F-, $k_{Coul} = k_{Coul}{}^{water}$).

At the end of the preparation stage (A), rods are arranged in both edge-to-face and face-to-face configurations, resulting in the creation of a relatively open structure. The bigger pores are associated with the formation of edge-to-face contacts. The smaller pores correspond instead to the gaps between sub-parallel particles.

Upon virgin loading (A − B − C), three different micro-mechanisms are clearly visible (*Figure 3.8a*):

i)   the reduction of the distance between particles in face-to-face configuration (i.e. mechanism 'i' in *Figure 3.1*and *3.8a*);

ii)   the rotation of particles in edge-to face contact configuration towards each other without contact disengagement (i.e. mechanism 'ii' in *Figure 3.1*and *3.8a*);

iii)   the loss of edge-to-face contacts, in turn generating a face-to-face configuration (i.e. mechanism 'iii' in *Figure 3.1*and *3.8a*).

At low stress (path A − B in *Figure 3.7* and *Figure 3.8a*), compression is mostly associated with mechanisms 'ii' and 'iii', as the volume change generated by the compression or loss of edge-to-face contacts is much higher than the one associated with mechanism 'i'. At higher stress (path B − C in *Figure 3.7* and *Figure 3.8a*, and from C onwards in *Figure 3.7*), compression gradually starts to be dominated by mechanism 'i', i.e. the reduction of the distance between sub-parallel particles, as face-to-face configuration becomes predominant.

Upon unloading (B − B', C − C') (*Figure 3.7* and *Figure 3.8b* and *3.8c*), the elastic behaviour is associated with different mechanisms depending on the magnitude of the pre-consolidation stress. At low pre-consolidation stress (B − B'), particles in both edge-to-face and face-to-face configuration undergo a small elastic rebound, due to the small

Coulombian repulsion activated in 'i' and 'ii' upon loading. The particle configuration of the specimen remains essentially unaltered during unloading.

As the pre-consolidation stress increases (C – C'), the edge-to-face contacts still existing in the assembly do not contribute to the rebound, i.e. their 'structure' remains totally unaltered after unloading. It appears that the particle 'frame' generated by the edge-to-face contacts is surrounded by a 'matrix' of particles in face-to-face configuration, which almost loads the particle frame isotropically. The elastic rebound is therefore mostly associated with the rebound of particles in face-to-face configuration. The high Coulombian repulsion due to the high stress reached upon loading in turn generates a higher rebound upon unloading.

Finally, it is worth noticing that the loss of edge-to-face contacts is indeed permanent (as in *Figure 3.1*): edge-to-face contacts lost upon loading are not recovered upon unloading.

3.5.3. Effect of dielectric permittivity on one-dimensional compression behaviour

The second aspect explored in the DEM analyses concerns the effect of the dielectric permittivity of the pore-fluid on the one-dimensional compression of clay. The experimental results of oedometer tests conducted on kaolin clay specimens saturated with air (dry powder, $\varepsilon = 1$), acetone ($\varepsilon = 25$) and laboratory water ($\varepsilon = 80$) are shown in *Figure 3.9.*
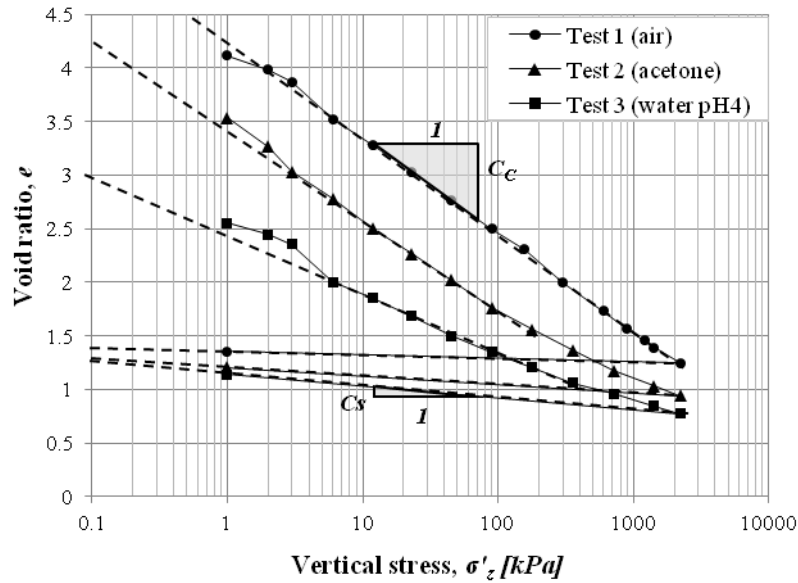
Figure 3.9. Test 1, 2, 3: mono-dimensional compression of kaolin mixed with air, acetone and water at pH = 4 (Pedrotti & Tarantino, 2017).

The numerical results of Simulation 1, 2, and 3 are shown in *Figure 3.10a* and *3.10b* for loading (non-reversible volume change) and unloading (reversible volume change) respectively. The variation of the long-range Coulombian interaction between particles as induced by the change in dielectric permittivity affects the macroscopic behaviour of the assembly upon both loading and unloading paths. Upon loading, the higher is the Coulombian stiffness (i.e. the lower is the dielectric permittivity of the pore-fluid) the higher is the slope of the virgin compression curve. Upon unloading, the higher is the Coulombian stiffness interaction, the lower is the slope of the unloading 'elastic' line.
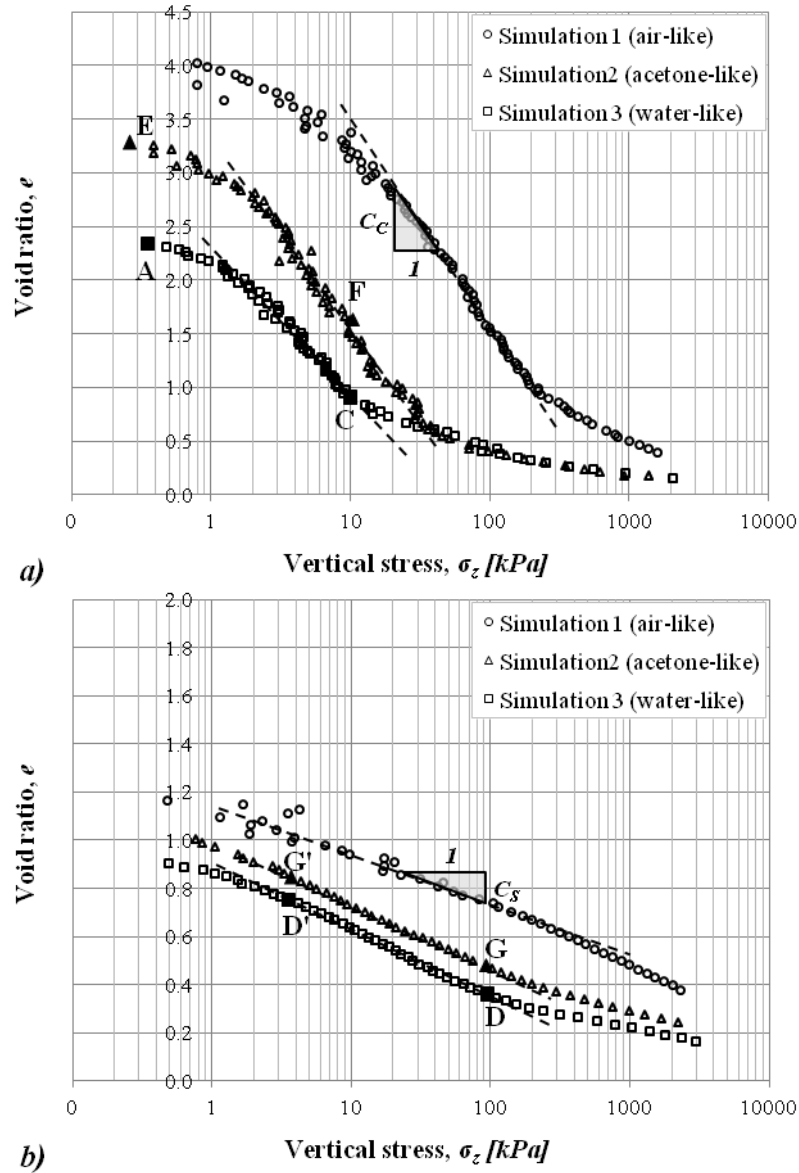
Figure 3.10. Numerical results of Simulation 1, 2, 3 during a) loading path and b) unloading path.

The response of the DEM models captures very well the behaviour observed experimentally (at a qualitative level). The agreement goes beyond a purely visual comparison. *Figure 3.11* shows the comparison in terms of compressibility index C_c and swelling index C_s normalised with respect to their values in 'ordinary' water (pH= 4, Simulation 3). A very good agreement is observed between experimental and simulated values.
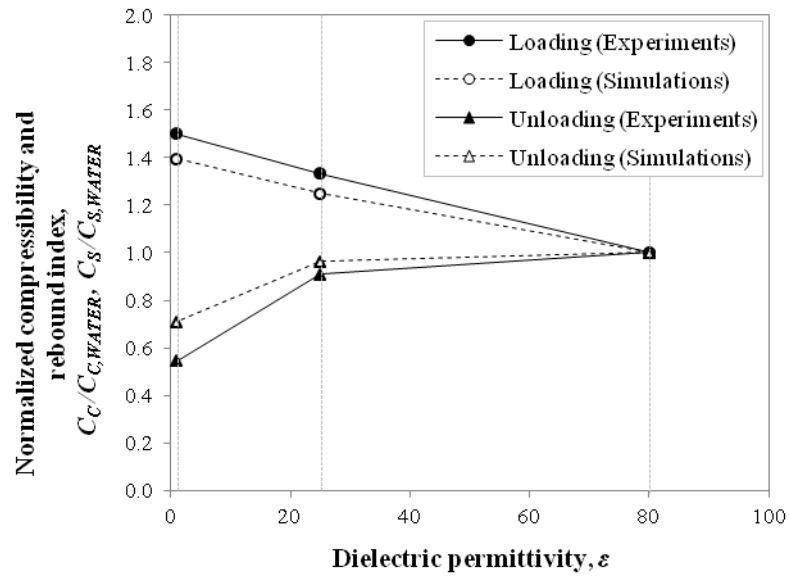
Figure 3.11. Normalised compressibility and swelling index: Test 1, 2, 3 and Simulation 1, 2, 3

The DEM model was again used to explore the micro-mechanisms leading to this macroscopic behaviour. *Figure 3.12* shows some of the specimen configurations obtained from Simulation 2 (acetone, $\varepsilon = 25$), and 3 (water, $\varepsilon = 80$). Pictures of the assemblies were taken at different stages: at the end of the preparation stage (A and E for water and acetone respectively), at an intermediate stage during first loading (C for water, F for acetone), and at two intermediate states upon unloading (D – D' for water and G – G' for acetone).

Simulation 3 (water pH4) **Simulation 2 (acetone)**

A : *e=2.34, σ_z=0.35 kPa*

E : *e=3.31, σ_z=0.26 kPa*

C : *e=0.91, σ_z=10.01 kPa*

F : *e=1.64, σ_z=10.00 kPa*

D : *e=0.36, σ_z=94.7 kPa*

G : *e=0.47, σ_z=92.3 kPa*

D' : *e=0.75, σ_z=3.57 kPa*

G' : *e=0.85, σ_z=3.27 kPa*
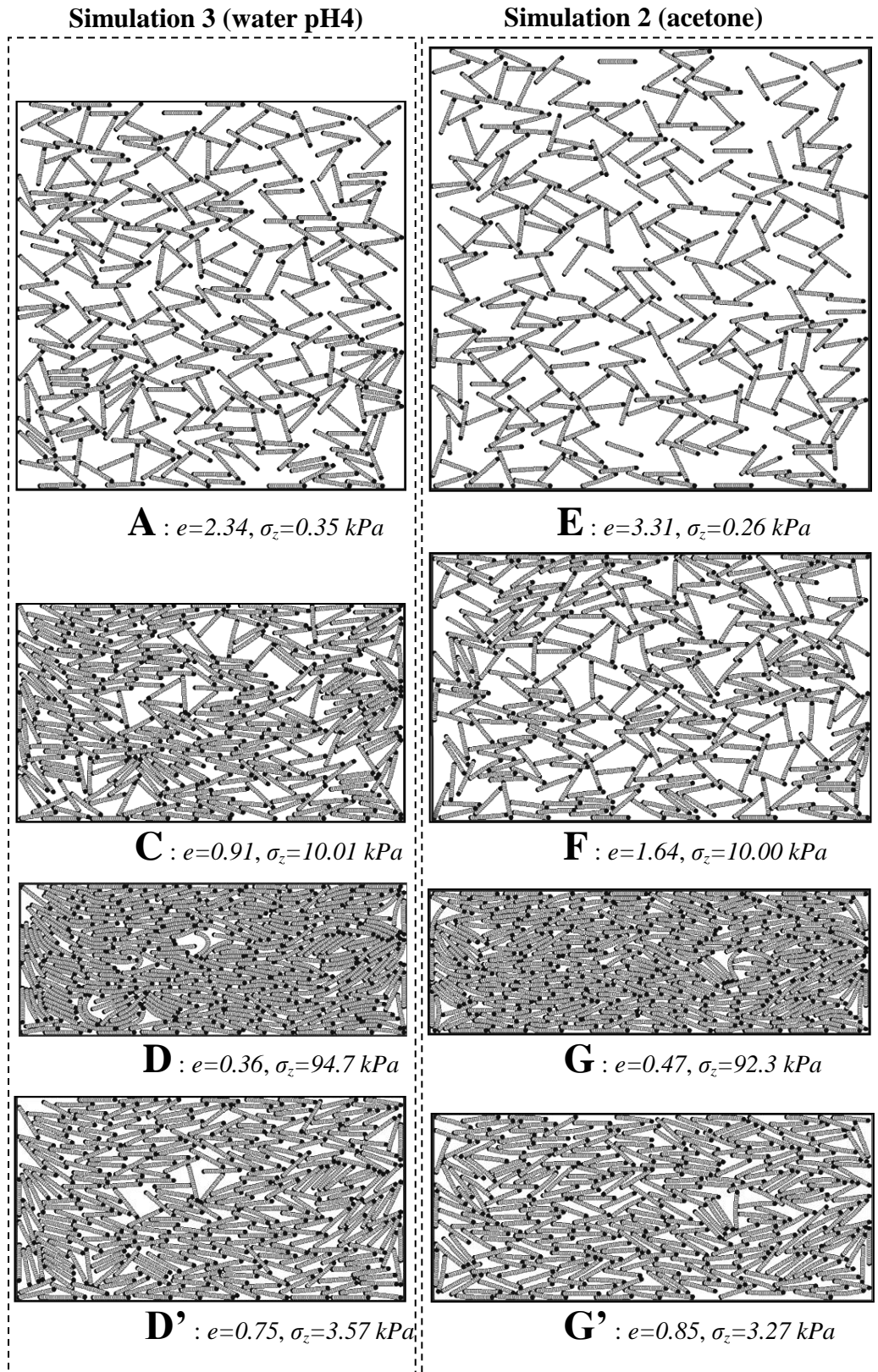
Figure 3.12. Different specimen configurations from Simulation 2 (E+, F-, $k_{Coul} = k_{Coul}^{acetone}$) and 3 (E+, F-, $k_{Coul} = k_{Coul}^{water}$).

The effect of the magnitude of the Coulombian stiffness k_{Coul} on the specimen configuration at the same stress is clearly visible. The higher the Coulombian stiffness, the more open is the structure of the assembly (A and E). Upon first loading (A – C and E – F in *Figure 3.10a* and *Figure 3.12*), the higher compressibility of the specimen in Simulation 2 (pore-fluid = acetone) is associated with mechanism 'iii'. The more open is the structure (i.e. the higher is the repulsion between negatively charged particle faces) the higher is the loss in terms of void ratio every time an edge-to-face contact is permanently lost upon first loading, leading to a faster reduction of void ratio with applied load.

Upon unloading (D – D' and G – G' *Figure 3.10b* and *Figure 3.12*), the higher rebound of the specimen in Simulation 3 (pore-fluid = water) is associated with mechanisms 'i' and 'ii', i.e. the reduction of the distance between particles in both edge-to-face and face-to-face configuration before unloading. This behaviour can be easily explained by considering two qualitative contact laws with different slopes k_{Coul}, as is the case for Simulation 2 and 3 (*Figure 3.13*). For particles interacting in the $\delta_{ij}^n < 0$ range, let us assume that the same change in external stress upon unloading (for example from D – D' and G – G'), also produces the same change in normal contact force, Δf. The resulting change in overlap $\Delta \delta$ depends on the Coulombian stiffness, in particular it is higher for the contact characterised by lower stiffness and, hence, higher dielectric permittivity (i.e. water).
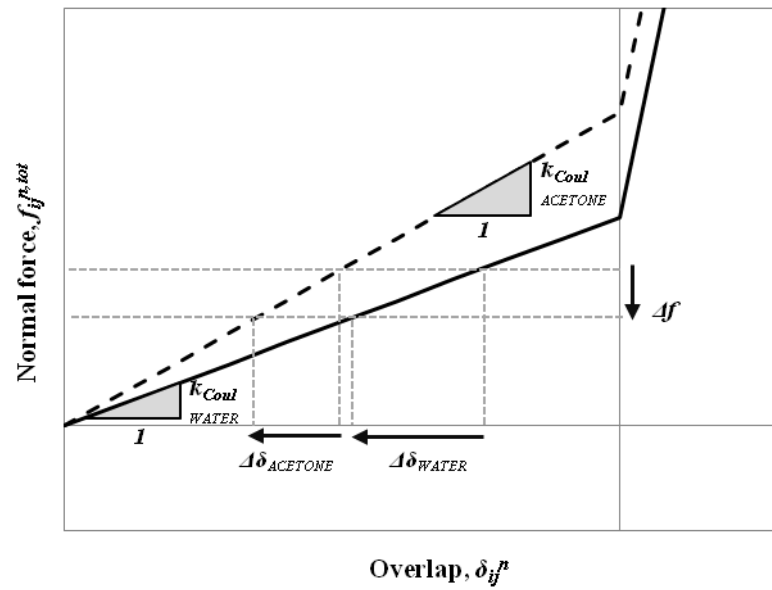
Figure 3.13. Effect of unloading paths oh the specimen rebound for different values of k_{Coul}

3.5.4. Effect of pH on compression behaviour

Finally, the validity of the DEM model against its ability to simulate the effect of pH on the compression behaviour of clay was explored by comparing the numerical results of Simulation 3 and 4 with the experimental results of oedometer tests performed on kaolin clay specimens saturated with ordinary deionised water (pH = 4) and alkaline water (pH = 9) (*Figure* 3.*14* and *3.15*).
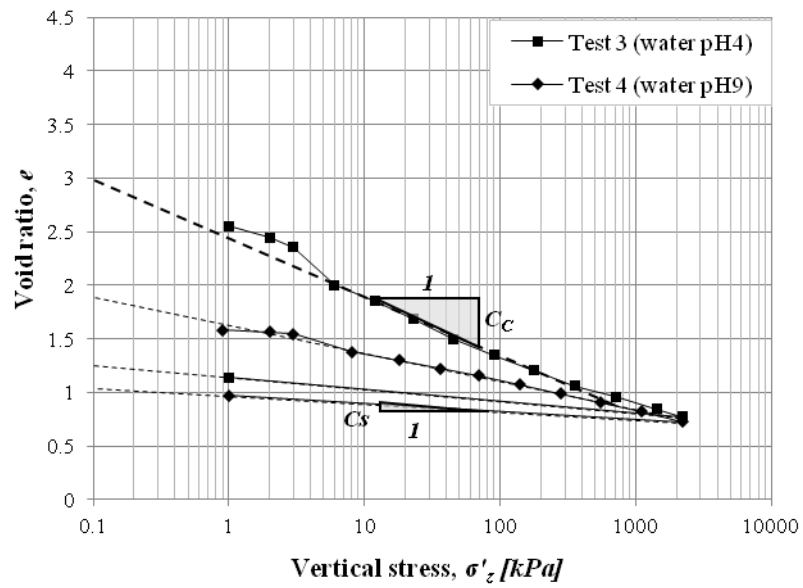
Figure 3.14. Test 3, 4: mono-dimensional compression of kaolin mixed acidic water (pH=4) and alkaline water (pH=9) (Pedrotti & Tarantino, 2017).
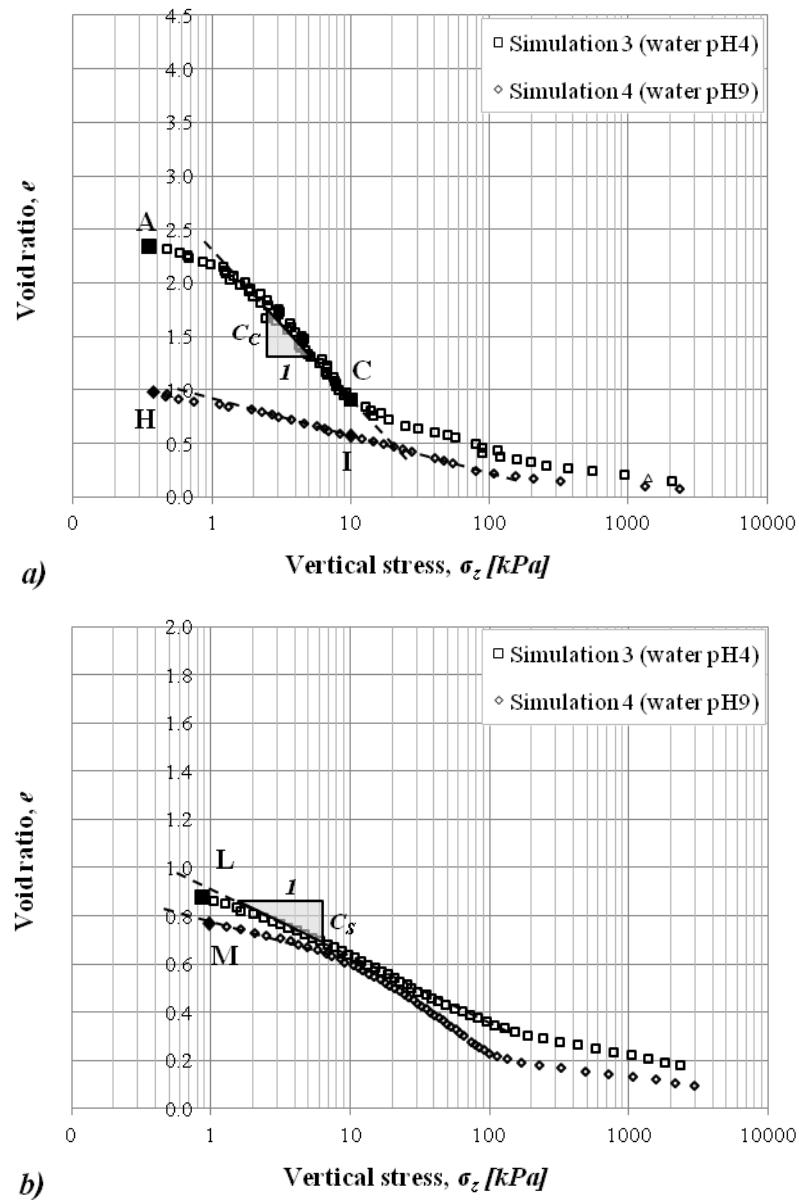
Figure 3.15. Numerical results of Simulation 3, 4 during a) loading path and b) unloading path.

The case of pH=9 was simulated by substituting the positive charge on the edges of the rods with a negative charge. As shown in *Figure 3.15*, this caused a drastic reduction of the void ratio at the same vertical stress, and reduced the specimen compressibility upon first loading. Upon unloading, the numerical response observed in Simulation 4 (pH=9) returns a small plastic deformation.

Figure 3.16 shows the comparison between the results obtained experimentally and numerically in terms of compressibility index C_c and swelling index C_s normalised with respect to their values in ordinary water (pH= 4, Simulation 3). Again, the trend observed in the experimental data is well captured by the simulation.
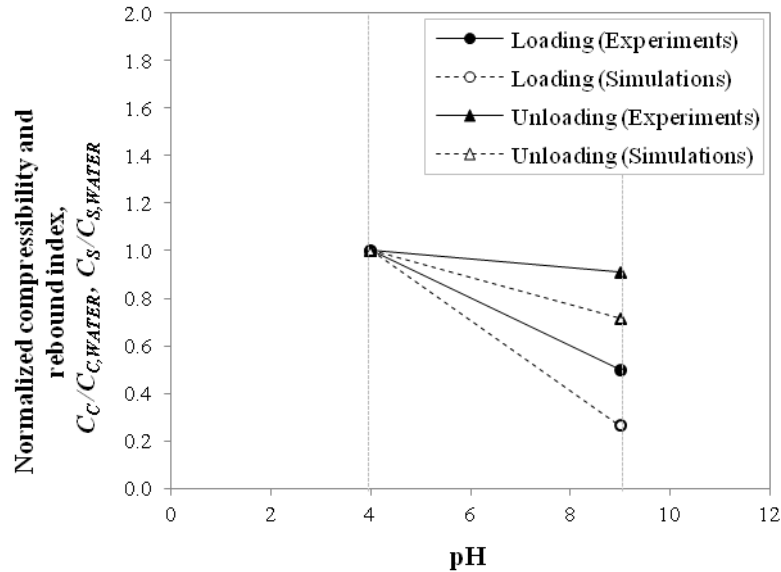
Figure 3.16. Normalised compressibility and swelling index: Test 3, 4 and Simulation 3, 4.

The underlying micromechanics behind the macroscopic behaviour at different pH levels was explored by comparing the assembly configurations obtained from Simulation 3 and 4 (*Figure 3.17*). The formation of edge-to-face contacts present in Simulation 3 does not occur in Simulation 4, where rods are arranged in sub-parallel configurations even at low stresses (A and H).

Upon first loading (A – C and H – I in *Figure 3.15a* and *Figure 3.17*), the lower compressibility observed in Simulation 4 is associated with the absence of edge-to-face contacts: the rods are arranged into a closer configuration at the beginning of compression, and the resulting microstructure is less compressible since there are no edge-to-face contacts that are permanently lost upon first loading.

Upon unloading, the response observed numerically in Simulation 4 shows that the loading and unloading paths overlap almost completely, expect at very low stresses. The small plastic deformation occurring at the end of the unloading path (point M in *Figure 3.15b* and *Figure 3.17*) is only associated with a slight rearrangement of the rods during first loading. In this case, plastic deformation arises from irreversible particle rearrangement as opposed to the plastic deformation observed in water at pH = 4, which is mainly controlled by the disengagement of the edge-to-face contact.

Simulation 3 (water pH4)   **Simulation 4 (water pH9)**
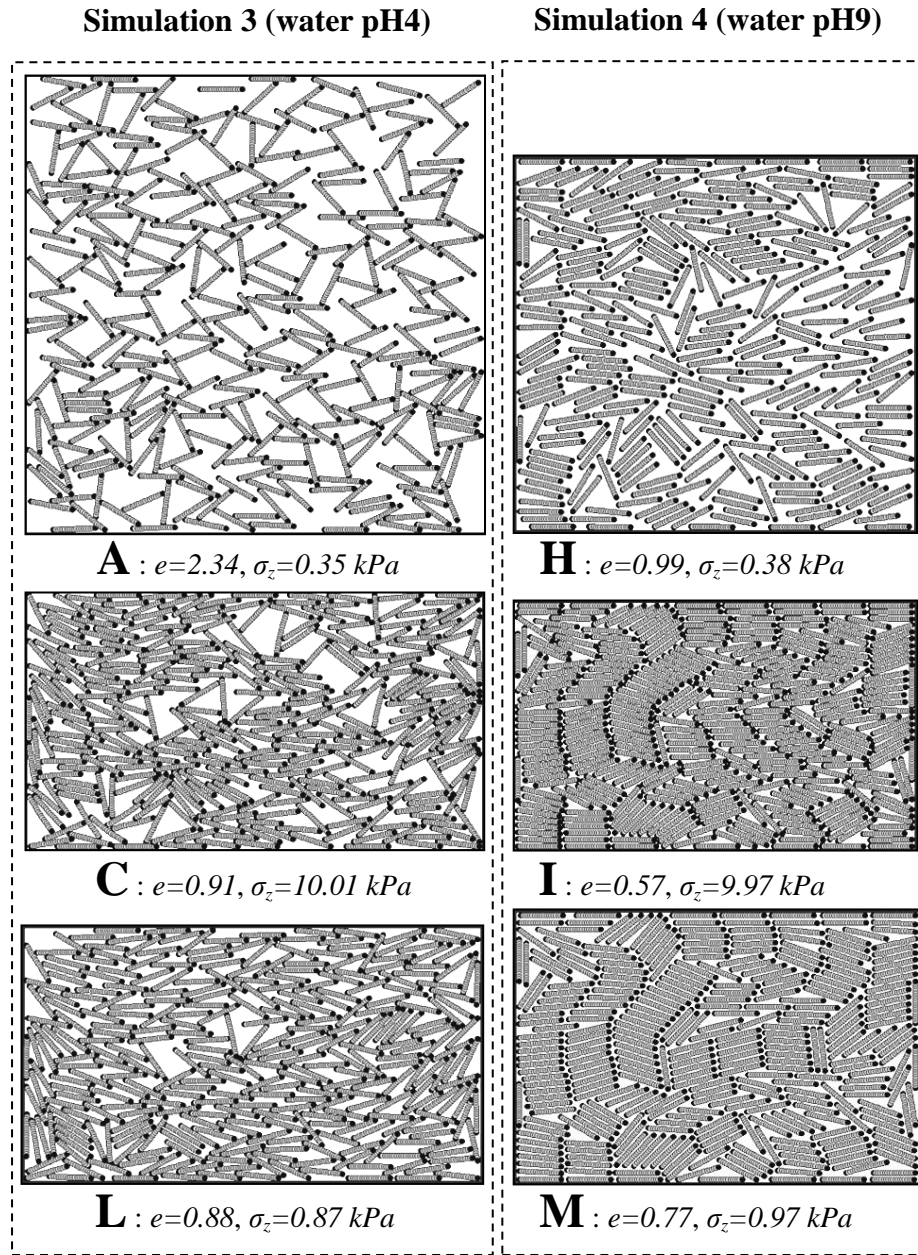
Figure 3.17. Different specimen configurations from Simulation 3 (E+, F-, $k_{Coul} = k_{Coul}^{acetone}$) and 4 (E-, F-, $k_{Coul} = k_{Coul}^{water}$).

3.6. CONCLUSIONS

This paper has presented a DEM validation of the micro-scale mechanisms affecting the macroscopic compression behaviour of a non-active clay. A numerical DEM framework

for the simulation of assemblies of clay-like particles has been introduced on the basis of a conceptual micro-mechanical model put forward by Pedrotti and Tarantino (2017) that describes the reversible and non-reversible particle-to-particle mechanisms occurring in non-active clays.

Two main aspects of the simulation of clayey geomaterials were addressed. First, assemblies of spherical primary units were created to form rod-shaped particles in order to account for the non-spherical shape of clay particles. Secondly, attractive and repulsive long-range forces were added to the basic linear-elastic contact laws in order to simulate the electro-chemical interactions driven by the positive/negative charge characterising the surface of clay particles.

The contact laws introduced in this work were tested against their ability to reproduce qualitatively some aspects of the compression behaviour of kaolin clay observed during an extensive experimental investigation carried out by Pedrotti and Tarantino (2017). The effect of pore-fluid chemistry (different pH and dielectric permittivity) was considered. An alkaline pore-fluid was simulated by assigning a homogeneous negative charge to the spheres forming the rods, resulting in the development of repulsive long-range forces between rods interacting with each other. Acidic pore-fluid was instead simulated by assigning a negative charge to the inner spheres of the rods and a positive charge to the ending spheres, resulting in the formation of edge-to-face contacts between rods. For the case where edge-to-face contacts are active, the effect of different dielectric permittivity of the pore-fluid was simulated by changing the magnitude of the attractive/repulsive electro-chemical forces.

The parameters defining the electro-chemical interactions (i.e. the stiffness of the Coulombian interaction k_{Coul} for different pore-fluids) were derived following a rigorous

calibration procedure against experimental results. Using the calibrated parameters, a very good agreement was observed between the experimental data and the results of four sets of simulations, in terms of a) the dependency of the slope of the unloading-reloading compression curves on the pre-consolidation stress, and b) the compression behaviour upon virgin loading and unloading-reloading paths. The ability to successfully reproduce clay behaviour at a qualitative level based on a simple calibration procedure shows a promising potential for the proposed DEM framework.

The contact laws presented in this work were intentionally kept simple to explore their potential for capturing the main features of the macroscopic response of non-active clay and, hence, corroborating the underlying micro-mechanical concept. It is expected that a quantitative prediction could be achieved by removing the simplifying assumptions of the adopted DEM framework, although at the cost of a significantly increased computational burden.

ACKNOWLEDGEMENTS

4. MICROMECHANICAL INTERPRETATION OF MECHANICAL WAVE PROPAGATION IN SATURATED NON-ACTIVE CLAY

Submitted for publication to Géotechnique

Arianna Gea Pagano* and Alessandro Tarantino**

POSITION AND AFFILIATION:
* PhD student, Department of Civil and Environmental Engineering, University of Strathclyde
** Professor, Department of Civil and Environmental Engineering, University of Strathclyde

ABSTRACT

This paper presents an investigation of the particle-scale mechanisms controlling the propagation of mechanical shear waves in saturated non-active clay. One-dimensional compression tests were carried out on kaolin clay specimens in an oedometer-like apparatus equipped with bender elements. The role of particle-to-particle mechanical and electro-chemical interactions was investigated by saturating the specimens with fluids having different pH and dielectric permittivity. The velocity of propagation of mechanical shear waves varied significantly with the different pore-fluids in a non-intuitive fashion. The experimental results were interpreted by considering i) the different 'stiffness' of mechanical and electro-chemical interactions and ii) the mechanical and electro-chemical force chains as inferred from DEM simulations. The wave velocity appeared to depend on the nature of the prevailing inter-particle interaction and on the amount of particles contributing to the transmission of forces throughout the specimen. In the light of the micromechanical interpretation of the experimental data, the value of soil density used for the calculation of soil stiffness at very small strains was discussed. It is proposed that an 'effective' density should be considered only taking into account the portion of solids

involved in the dynamic motion. Preliminary calculations suggested that the 'effective' density may deviate significantly from the bulk density.

4.1. INTRODUCTION

The velocity of propagation of mechanical waves is commonly used in geotechnical applications to infer soil stiffness at very small strains, G_0. Very small strain stiffness has been demonstrated experimentally to depend on mean effective stress, void ratio (Hardin & Richart, 1963; Hardin, 1978; Iwasaki & Tatsuoka, 1977; Prange, 1981; Kokusho & Esashi, 1981) and, for the case of clays, on the overconsolidation ratio (Hardin & Black, 1968; Hardin & Black, 1969). For design purposes, empirical relationships for very small strain stiffness have been developed to include dependency on these variables.

However, further experimental studies have highlighted that the macroscopic response may not always be well captured by the empirical relations for G_0. For instance, the very small strain stiffness of transitional soils and polydisperse granular geomaterials (Wichtmann & Triantafyllidis, 2009; Goudarzy, et al., 2016) has been proven to be controlled by an 'effective' void ratio, referred to as 'equivalent granular' or 'skeleton' void ratio (i.e. the void ratio that would exist in the packing if all the particles not involved in the force transmission were removed). Micro-mechanical considerations, based on particle arrangements and force transmission through particle-to-particle contacts (Radjai & Wolf, 1998; Radjai, et al., 1998), have been used to clarify the nature of the 'effective' void ratio.

Therefore, a micro-mechanical insight into the processes occurring at the particle scale is key to the correct interpretation of soil behaviour at the macroscale. For the case of

granular geomaterials, the interplay between particle-scale and macroscale behaviour has been explored via analytical and numerical models based on grain-to-grain contact mechanics. Wave velocities or soil stiffness at very small strain have been successfully investigated analytically and numerically (the latter generally using DEM simulations) for the case of ordered and random packings under different conditions (Kruyt, 2010; Liao & Chang, 1997; Kruyt & Rothenburg, 1998; Luding, 2005; Mouraille, 2009; O'Donovan & O'Sullivan, 2012; O'Donovan, et al., 2016).

The same approach cannot be easily replicated for clayey geomaterials, due to the lack of understanding of the nature of inter-particle interactions. In contrast to granular materials, particle-to-particle interactions in clay are not only mechanical, but also electro-chemical. The relative role of mechanical and electro-chemical interactions in the force transmission mechanisms throughout clayey soils (and, hence, in the propagation of mechanical waves) remains as yet little explored.

The aim of this paper is to make a step forward towards the interpretation of the micro-mechanisms affecting the velocity of propagation of mechanical shear waves in saturated non-active clay. To this end, mechanical interactions (occurring between particles in contact) and electro-chemical interactions (activated at a certain distance between particles not in contact) in reconstituted kaolin clay specimens were investigated experimentally by saturating the specimens with pore-fluids having different dielectric permittivity and pH. The dielectric permittivity was varied to affect the strength of the repulsion between particles (electro-chemical interaction) in the presence of edge-to-face contacts (mechanical interaction). The pore-fluid pH was instead modified to de-activate edge-to-face (mechanical) contacts between particles, leading to electro-chemical interactions only.

Each specimen was subjected to 1-D loading and unloading in an oedometer-like apparatus equipped with bender elements. The velocity of propagation of mechanical shear waves through the specimens was measured at different stress levels during loading and unloading, and the results obtained for different pore-fluids were compared. To interpret the experimental data, mechanisms of force transmission were hypothesised based on i) the quantitative analysis of the interaction between two particles, either mechanical or electro-chemical, and ii) particle configurations obtained from DEM simulations carried out in a separate work (Pagano et al. 2018 – **Chapter 3**).

4.2.   MATERIALS AND METHODS

4.2.1. Testing material and specimen preparation

The non-active clay tested in this study was Speswhite kaolin (plastic limit and liquid limit equal to $w_P = 0.32$ and $w_L = 0.64$ respectively). Prior to preparing the specimens, kaolin powder was oven dried at 105°C for at least 24 hours. Four different specimens were then prepared and tested: dry powder only (Specimen I), dry powder + ethanol (Specimen II), dry powder + de-mineralised water (Specimen III), and dry powder + alkaline water (Specimen IV). Specimens II to IV were prepared from slurry at water (or ethanol) contents of approximately $1.5 \cdot w_L$.

Alkaline water for the preparation of Specimen IV was obtained by adding potassium hydroxide (KOH, molar concentration smaller than 0.01 M) to laboratory de-mineralised water. Since pH affects the liquid limit of kaolin, Specimen IV was prepared at a lower water content than Specimen II and III ($w=55\%$ instead of $w=100\%$), as a higher water

content would have resulted in a highly fluid mixture. *Table 4.1* shows the properties of the specimens tested in this study.

Specimen	I	II	III	IV
Initial height, h_0 [cm]	9.1	11.0	9.8	9.9
Diameter, D [cm]	10	10	10	10
Specific gravity, G_s	2.605	2.605	2.605	2.605
Dry mass, M_d [g]	375.61	576.71	587.95	843.59
Pore fluid	Air	Ethanol	De-miner. Water	Alkaline Water
Dielectric permittivity, ε	1	24	80	80
pH	-	-	4	9

Table 4.1. Specimen properties.

The four pore-fluids used in this study (air, ethanol, de-mineralised water and alkaline water) were purposely selected in order to obtain specimens with different initial microstructures, as in Pedrotti & Tarantino (2017).

Pore-fluids with different dielectric permittivity (air: $\varepsilon = 1$, ethanol: $\varepsilon = 24$, de-mineralised water: $\varepsilon = 80$) were chosen to modify the intensity of the repulsion forces between particles both in contact (edge-to-face configuration) and not in contact (face-to-face configuration). The higher the dielectric permittivity, the lower the intensity of the repulsion (at the same inter-particle distance).

The pore-fluids generating different pH (laboratory de-mineralised water: pH = 4 after exposure to clay, alkaline water: pH = 9 after exposure to clay) were chosen to control the activation or the de-activation of the edge-to-face contacts. In particular, pH values greater than the point of zero charge (PZC), equal to 5.5 for kaolin clay (Sposito, 1984; Carroll & Walther, 1990; Huertas, et al., 1998) resulted in the de-activation of edge-to-face contacts.

4.2.2. **Laboratory equipment and testing procedures**

Four one-dimensional mechanical loading/unloading tests were carried out in an oedometer-like apparatus (100 mm diameter) equipped with bender elements (BEs) for the measurement of shear wave velocities. A schematic view of the apparatus is shown in *Figure 4.1*. BEs were constructed using double-layer piezoceramic elements (BIMS-N-PZT5A4-HT x-poled element and BIMP-N-PZT5A4-HT y-poled element by Morgan Technical Ceramics for receiver and transmitter bender element respectively). The sensors were embedded into the top cap and pedestal of the cell, and in turn connected to a function generator and an oscilloscope for triggering/recording the input/output signal respectively.

After specimen preparation, the kaolin mixture (dry powder or slurry) was placed into the cell. Drained conditions and specimen saturation (except for the case of dry powder) were ensured for the entire duration of each test by connecting the base pedestal to a reservoir containing the same fluid used to saturate the specimen. The reservoir was placed on a balance for monitoring pore-fluid exchanges during the tests. The first consolidation step was performed by simply placing the top cap on the specimen, corresponding to a vertical stress of 1 kPa. At the end of the first consolidation step, one-dimensional loading was carried out in displacement-control mode by applying a constant displacement rate of 0.0035 mm/min to the specimen via a loading frame. A load cell and a vertical displacement transducer allowed for the continuous measurement of applied force and axial displacement respectively. The void ratio and the vertical stress during the tests could then be calculated. Furthermore, the propagation of mechanical shear waves was triggered at specific levels of stress during the tests (15 kPa, 30 kPa, 65 kPa, 100 kPa, 225 kPa, 590 kPa) by exciting the transmitter BE with a sinusoidal signal (input frequency 5 kHz).

Output signals were recorded and interpreted in order to calculate the corresponding velocities of propagation.
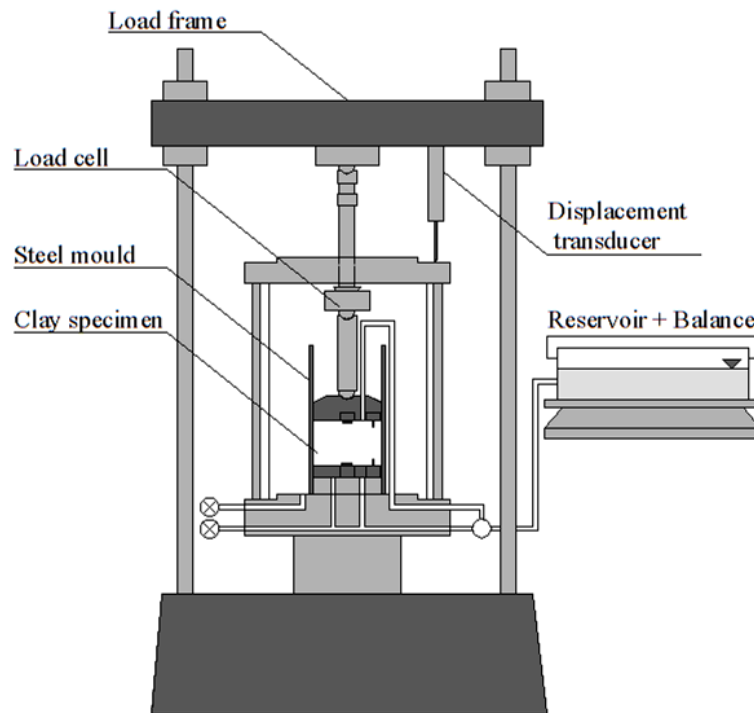
Figure 4.1. Schematic view of the oedometer-like apparatus equipped with bender elements.

4.3. EXPRERIMENTAL RESULTS

4.3.1. 1-D loading and unloading

Figure 4.2 shows the results of the one-dimensional loading/unloading performed on the four specimens in terms of void ratio against vertical effective stress. As in Pedrotti and Tarantino (2017), the specimens exhibited a different compression behaviour as a consequence of the different microscopic structure induced by the pore-fluid chemistry.
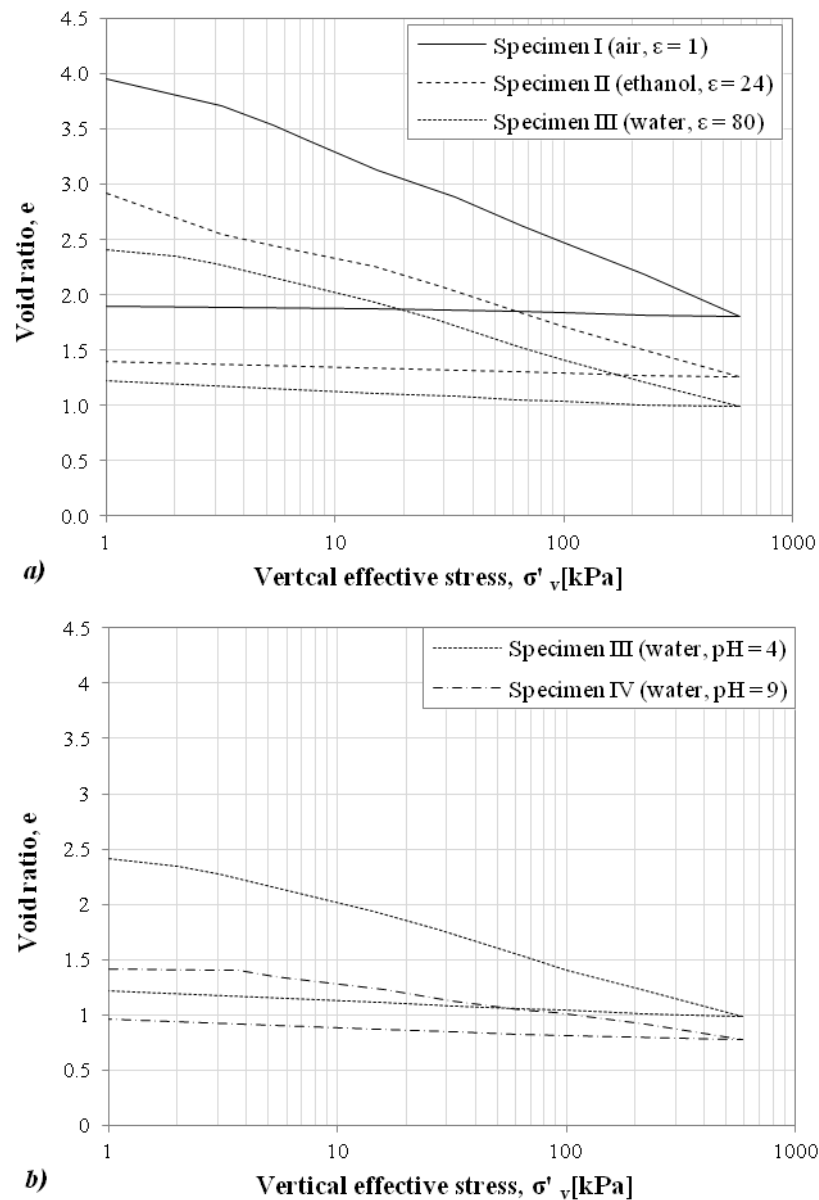
Figure 4.2. Macroscopic 1-D compression behaviour of kaolin clay saturated with a) fluids with different dielectric permittivity, and b) fluids at different pH.

The effect of dielectric permittivity for Specimen I (dry powder, $\varepsilon = 1$), Specimen II (saturated with ethanol, $\varepsilon = 24$) and Specimen III (saturated with de-mineralised water, $\varepsilon = 80$) is shown in *Figure 4.2a*. At any level of vertical effective stress, the higher the dielectric permittivity of the pore-fluid (and, hence, the lower the repulsion between negatively charged faces), the lower the void ratio of the specimen. Upon loading, the

compressibility of the specimen was observed to be slightly smaller with increasing dielectric permittivity. Upon unloading, an opposite trend was observed, with the rebound of the specimen increasing with increasing dielectric permittivity.

Figure 4.2b shows the effect of the pore-fluid pH on soil compressibility. Specimen III (saturated with de-mineralised water, pH = 4) exhibited a higher void ratio than Specimen IV (saturated with alkaline water, pH = 9) at any level of stress, and was observed to be more compressible upon loading. No noticeable differences in the rebound of the specimens were apparent upon unloading.

4.3.2. Wave propagation

The velocity of propagation of the shear waves travelling through the specimens was obtained from the interpretation of the output signals recorded by the oscilloscope during the four tests. Raw signals were first subjected to base-line correction and filtering (low pass Butterworth filter of order 1) in order to remove any background noise and facilitate the interpretation of the wave arrival. An example of filtered and corrected output signal for different levels of stress during loading is shown in *Figure 4.3* (dry powder). The travel time of the wave, t, was taken in this study as the time interval between the first main peaks of the input and output signals (Viggiani & Atkinson, 1995a; Viggiani & Atkinson, 1995b), while the travel length, L, was chosen as the tip-to-tip distance between the transmitter and receiver bender elements (Dyvik & Madshus, 1985; Viggiani & Atkinson, 1995a; Fernandez, 2000). The velocity of propagation was then calculated as:

$$V_s = \frac{L}{t} \hspace{6cm} \textit{1}$$

Figure 4.4 shows the evolution of the velocity of propagation of the shear waves against vertical effective stress during loading and unloading. As for the void ratio, the velocity of propagation appears to be affected by both the dielectric permittivity and the pH of the pore-fluid.
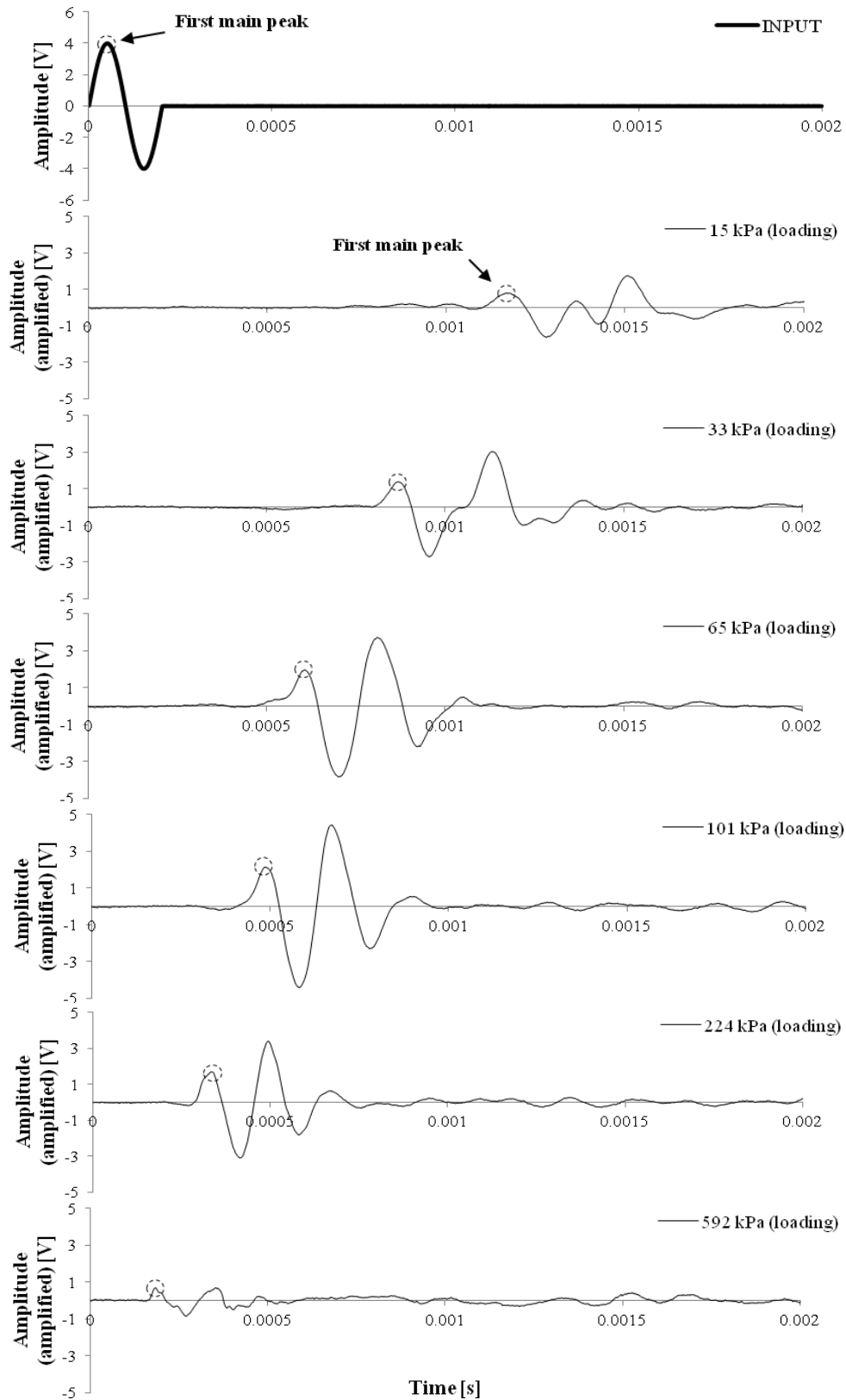
Figure 4.3. Input signal and output signal (filtered and corrected) at different

stress levels during loading

The effect of dielectric permittivity is shown in *Figure 4.4a*. At low levels of stress, the velocity of propagation of the shear waves in the specimens saturated with air, ethanol and de-mineralised water was observed to be essentially the same. However, after a threshold value of vertical effective stress was reached (about 225 kPa), the velocities of propagation diverged for the three specimens, with shear waves being much faster for Specimen I (dry powder, $\varepsilon = 1$), intermediate for Specimen II (saturated with ethanol, $\varepsilon = 24$), and slower for Specimen III (saturated with de-mineralised water, $\varepsilon = 80$). The difference in the wave velocity for the three specimens remained during unloading.

The effect of pH is shown in *Figure 4.4b*. Shear waves appeared to be slower in Specimen III (saturated with de-mineralised water, pH = 4) and faster in Specimen IV (saturated with alkaline water, pH = 9) upon both loading and unloading.

These responses are not intuitive and an interpretation has been sought by investigating the micro-mechanical interactions underpinning the experimental observations.
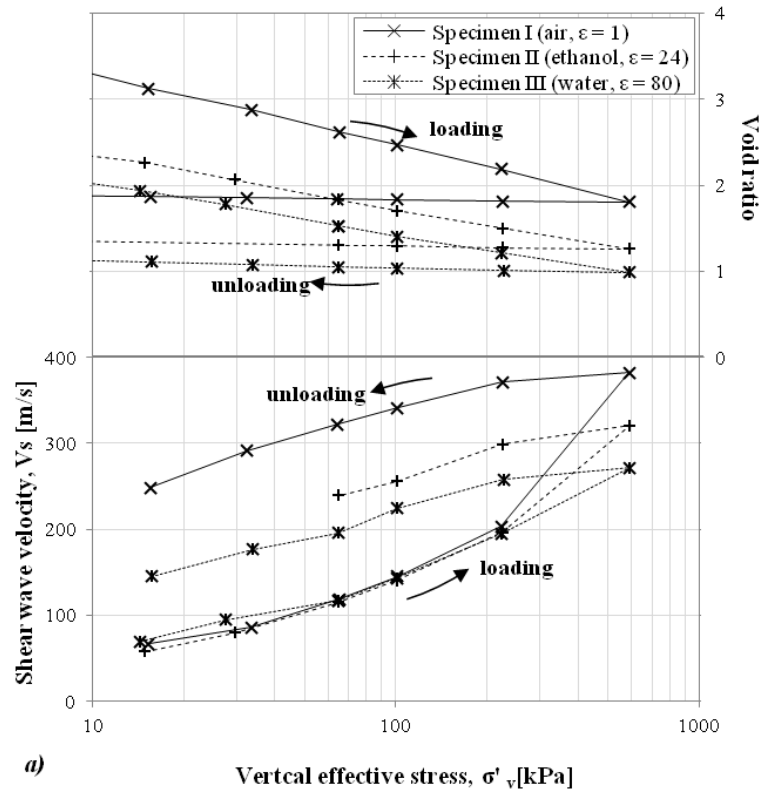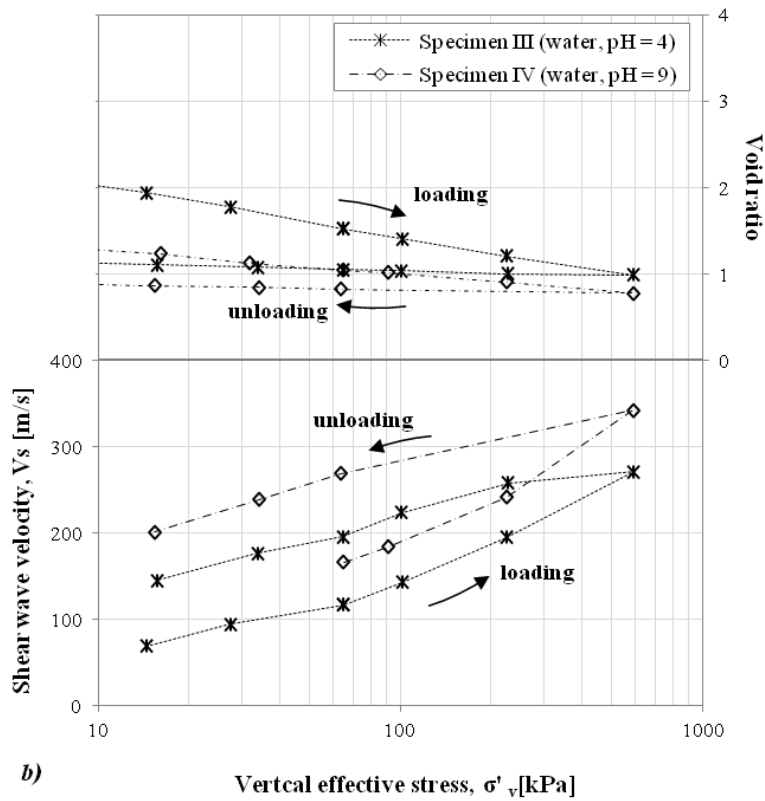
Figure 4.4. 1D compression and shear wave propagation velocity of kaolin specimens saturated with a) fluids with different dielectric permittivity, and b) fluids at different pH.

4.4. MICROMECHANICAL INTERPRETATION

4.4.1. Mechanical and electro-chemical particle-to-particle interactions

The micromechanical analysis of the behaviour of kaolin clay specimens is based on the assumption that clay particles may interact in two different manners depending on the nature of the pore-fluid (*Figure 4.5*):

a) Via mechanical interaction, generated when particle faces are negatively charged and particle edges are positively charged, leading to a Coulombian attraction between the edge and the face of neighbouring particles. Once an edge and face come in contact (*Figure 4.5a*), their interaction is controlled by the mechanical properties of the particles. Mechanical contacts in kaolin clay typically occur for values of pH smaller than the PZC value, i.e. in the presence of 'active' edge-to-face interactions (Pedrotti & Tarantino 2017).

b) Via electro-chemical interaction, generated at a certain distance between particles (*Figure 4.5b*). These include Coulombian interaction (either attractive or repulsive, depending on the charge distribution on the surface of adjacent particles) and the van der Waals interaction (attractive for kaolin particles), whose balance is theoretically described by the DLVO theory (Derjaguin & Landau, 1941; Verwey, et al., 1948). Electro-chemical repulsion can occur either when both particle face and edge are negatively charged (i.e. as a repulsion between negatively charged faces of particles in face-to-face configuration, typically occurring for values of pH higher than the PZC value) or when particle faces are negatively charged and particle edges are positively charged (in the form of repulsion between negatively charged faces of particles in edge-to-face configuration).

	ATTRACTIVE **REPULSIVE** **REPULSIVE**
a) Mechanical interaction	*b) Electro-chemical interaction*
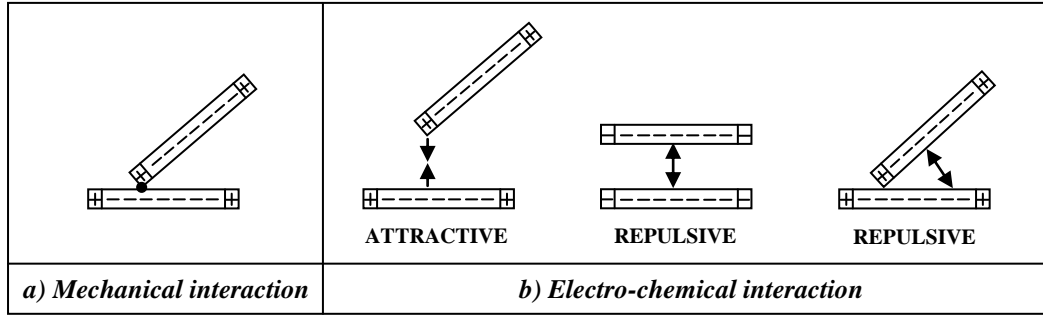
Figure 4.5. Possible modes of particle-to-particle interaction in kaolin clay.

Mechanical interactions occurring between particles in edge-to-face configuration can be quantitatively described similarly to the case of mechanical contacts in granular geomaterials. The intergranular force developing at the contact between the edge of a particle and the face of its neighbour can therefore be calculated according to Hertz as the intergranular force developing between a sphere (representing the particle edge) and an elastic half-space (representing the particle face):

$$F = \frac{4}{3} E^* r^{1/2} \delta^{3/2} \qquad\qquad\qquad 2$$

where E^* is the equivalent Young modulus of the particles, r is the radius of the sphere representing half the thickness of the particle, and δ is the depth of indentation of the sphere into the half-space. By dividing the intergranular force by the gross contact area, A, the stress associated with the mechanical interaction between particles in contact, σ^m, can be calculated:

$$\sigma^m = \frac{F}{A} = \frac{4}{3A} E^* r^{1/2} \delta^{3/2} \qquad\qquad\qquad 3$$

On the other hand, the electro-chemical repulsive interaction between negatively charged faces of clay particles in water can be quantified according to Bolt (1956). The interaction between two clay particles in face-to-face configuration occurs through the

overlap of their diffuse double-layers, and the resulting repulsion equals the difference between the osmotic pressure in the central plane between the plates and the osmotic pressure of the free solution. An approximate solution for the distance between parallel clay particles in suspension, assuming the validity of the Gouy theory (Gouy, 1910) for the ion distribution in the double-layer and van't Hoff equation for the calculation of the osmotic pressure, can therefore be derived as:

$$d = \frac{log64 - log(\sigma^{ec}/RTc_0)}{0.4343(2\sqrt{\beta c_0})} - x_0 \qquad\qquad 4$$

where $R = 8.314472$ J/mol·K is the gas constant, σ^{ec} is the repulsive intergranular stress, T is the temperature, c_0 is the concentration of ions in the bulk liquid, β is a constant dependant on the temperature and x_0 is a constant dependant on the surface density of charge of the clay particle. By rearranging Equation 4, σ^{ec} can be derived as:

$$\sigma^{ec} = 10^{[log64+log(RTc_0)-0.4343(d+x_0)(2\sqrt{\beta c_0})]} \qquad\qquad 5$$

Figure 4.6 shows the evolution of the Hertzian interparticle stress σ^m with the depth of indentation for the case of $E^* = 1$ GPa (Vanorio, et al., 2003), $r = 0.05$ μm and $A = 1$ μm^2 (consistent with Mitchell & Soga, 2005), together with the variation of the electro-chemical repulsive intergranular stress σ^{ec} against the particle distance for the case of $T = 293.15$ K, $c_0 = 20$ mol/m^3 (Peroni & Tarantino, 2005), $\beta = 10^{16}$ m/mol (Bolt, 1956) and $x_0 = 2 \cdot 10^{-10}$ m (Bolt, 1956).
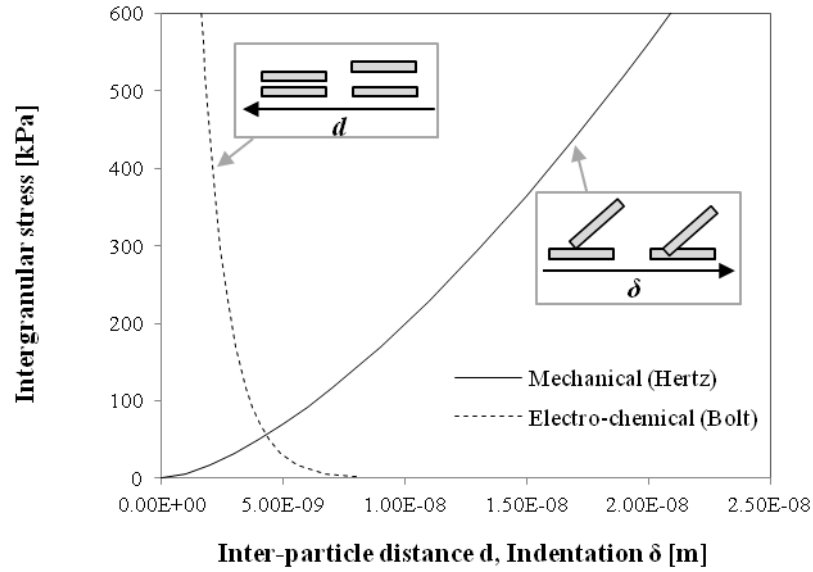
Figure 4.6. Evolution of mechanical inter-particle stress with depth of indentation, and electro-chemical inter-particle stress with inter-particle distance

Figure 4.7 shows the variation of the absolute value of the derivative of σ^m and σ^{ec} with respect to the displacement (depth of indentation for mechanical interaction and distance between particles for electro-chemical interaction) with the intergranular stress. The derivative of the intergranular stress is representative of the 'stiffness' of the interaction between two particles, either mechanical or electro-chemical. The analytical comparison shows that the electro-chemical interaction exhibits a higher stiffness than the mechanical contact at any level of stress. If the velocity of propagation is assumed to depend on the stiffness of the interparticle interaction, a wave propagating through particles interacting only via electro-chemical interactions is expected to travel faster than a wave propagating through particles interacting only via mechanical contacts at the same stress. If both modes of interaction are active, the velocity of propagation of the wave would instead be controlled by the stiffness of the prevailing mode of interaction

(mechanical or electro-chemical) between the particles involved in the propagation. In turn, the prevailing mode of interaction would be controlled by the microstructure.
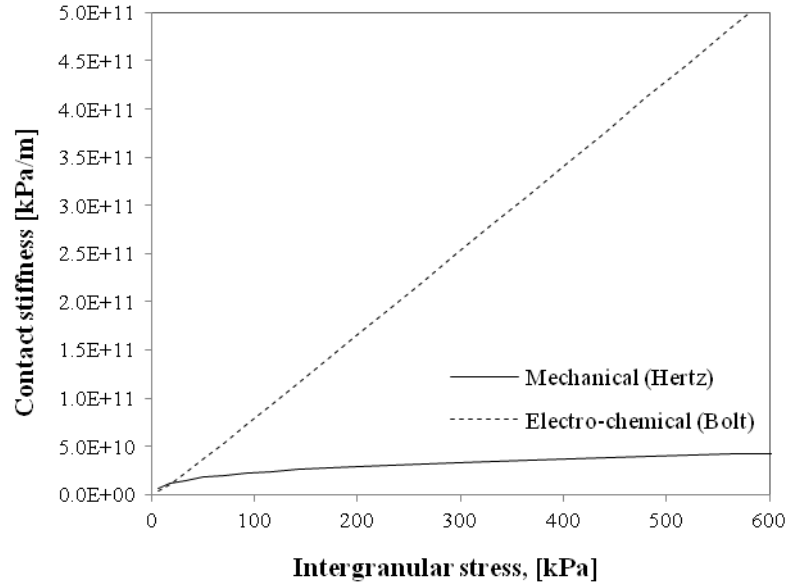
Figure 4.7. Evolution of the stiffness of mechanical and electro-chemical interactions.

Kaolin clay microstructure during 1-D loading can be investigated numerically via DEM simulations according to Pagano et al. (2018). In that work (see Chapter 3), simplified mechanical and electro-chemical interactions were implemented into a DEM model and successfully tested against their ability to reproduce qualitatively the compression behaviour of clay observed experimentally. Two core aspects characterised the DEM model for kaolin clay (*Figure 4.8*):

a) Each kaolin clay particle was designed as a rod-like element (2D analysis) made of spherical sub-particles bonded together. A negative or positive charge was assigned to each sub-sphere in order to mimic the positive or negative charge on the edge and face of kaolin particles (*Figure 4.8a*).

b) A novel contact law was assigned to each contact between sub-spheres. The contact law included both electro-chemical interactions (developing after a threshold

distance between sub-spheres not in contact) and mechanical interactions (developing between overlapping sub-spheres). Piecewise linear functions were chosen in order to reduce the computational burden. Repulsive/attractive interactions between equal/opposite charges were simulated as positive/negative forces respectively (*Figure 4.8b*).
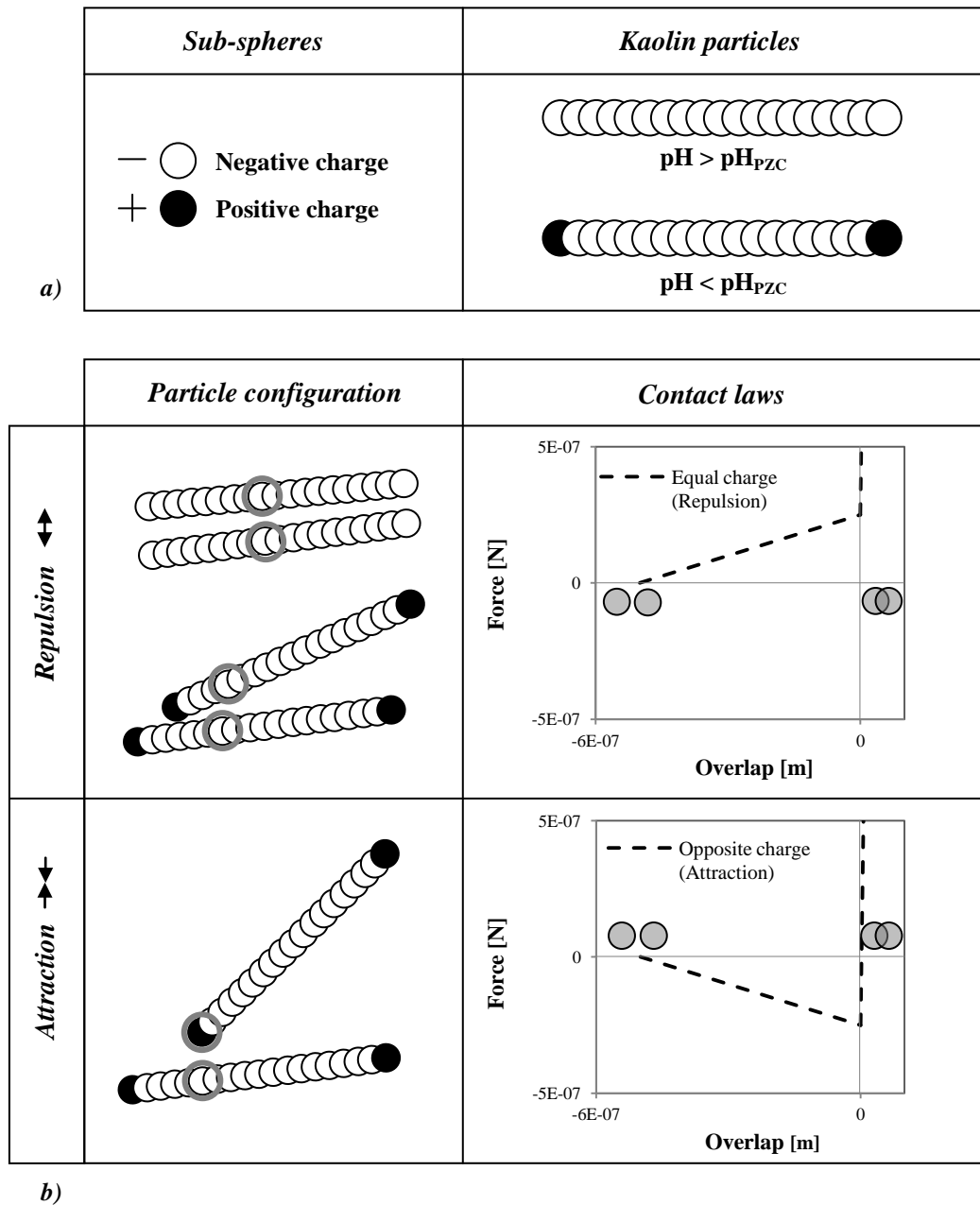
Sub-spheres	*Kaolin particles*
— ◯ **Negative charge** + ● **Positive charge**	$pH > pH_{PZC}$ $pH < pH_{PZC}$

a)

	Particle configuration	*Contact laws*
Repulsion		Equal charge (Repulsion)
Attraction		Opposite charge (Attraction)

b)

Figure 4.8. DEM model for kaolin clay: a) design of clay-like particles; b) contact laws assigned to sub-spheres of clay-like particles in different configurations.

4.4.2. Effect of pH on wave propagation velocity

Figure 4.9 shows the results of DEM simulations mimicking the one-dimensional loading of rod-like kaolin particles with active edge-to-face interaction (corresponding to the case of $pH < pH_{PZC}$) and de-activated edge-to-face interaction (corresponding to the case of $pH > pH_{PZC}$). Pictures of the assemblies were taken at the end of specimen preparation (*Figure 4.9a-b*, low vertical stress) and after 1-D loading to the same vertical stress level (*Figure 4.9c-d*, high stress). The locations of active mechanical interactions are marked as open circles, whereas the locations of active electro-chemical interactions are marked as black crosses.

	Edge-to-face (pH<pH$_{PZC}$, ε=80)	Face-to-face(pH>pH$_{PZC}$,ε=80)
Low stress	*a)*	*b)*
High stress	*c)*	*d)*
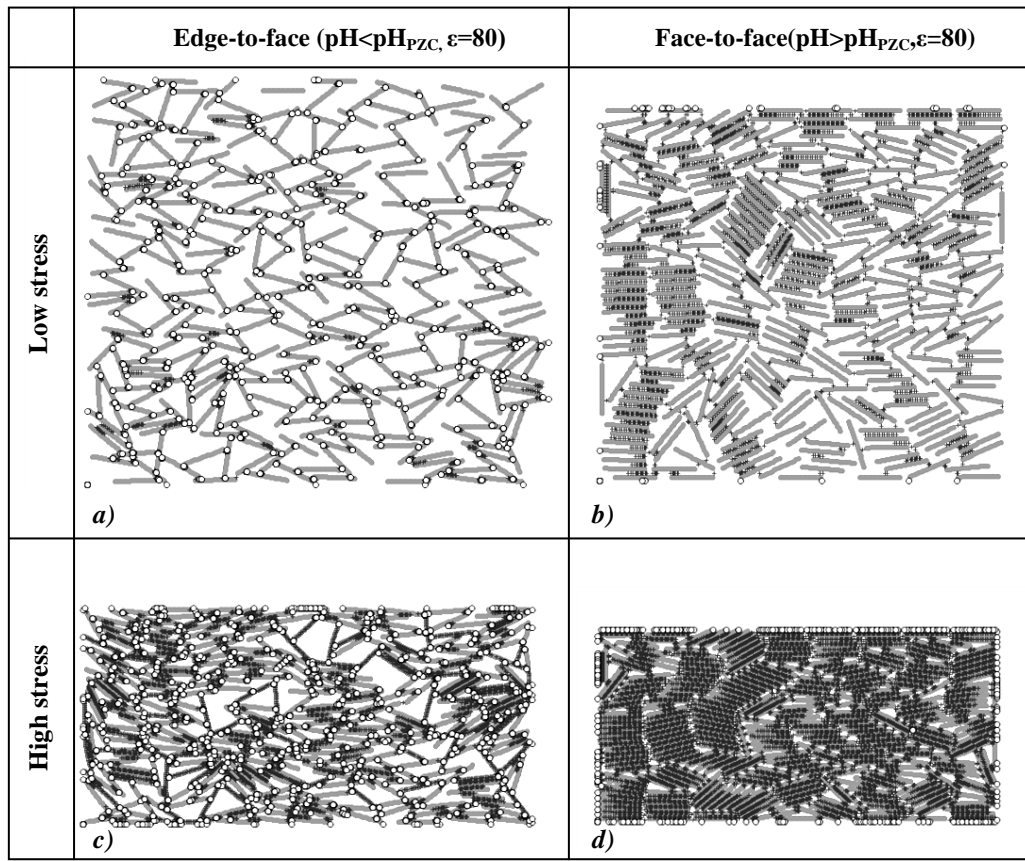
Figure 4.9. DEM configurations mimicking the one-dimensional loading of kaolin particles with active edge-to-face interaction and de-activated edge-to-face interaction at high and low stress

For the case of particles in edge-to-face configuration, the initial microstructure (low vertical stress, *Figure 4.9a*) is characterised by the formation of 'bridges' between two or more particles, giving the assembly an open structure. Porosity is associated with large pores formed by particles 'bridged' via edge-to-face contacts, and small pores present between particles in sub-parallel configuration. The interaction between particles occurs mainly via mechanical contacts (open circles), whereas only a few active electro-chemical interactions (black crosses) are active. As the specimen is compressed (*Figure 4.9c*), particles are brought closer to each other and the number of active electro-chemical interactions increases. Particles interact via both mechanical and electro-chemical

interactions, and some of the edge-to-face contacts characterising the initial microstructure are forced to disengage due to external loading.

On the other hand, particles in face-to-face configuration arrange themselves into closer initial microstructures even at low stress (*Figure 4.9b*), and the porosity of the assembly is only associated with the small pores between sub-parallel particles. Except for particles interacting with the external walls, the interaction is always electro-chemical (black crosses). As the specimen is compressed (*Figure 4.9d*), the particles get closer to each other and the number of active electro-chemical interactions increases in order to counteract the external stress.

The different particle configurations and the associated distribution of mechanical and electro-chemical interactions as shown in *Figure 4.9* can help interpret the experimental results in terms of wave propagation velocities observed in *Figure 4.4b*.

Let us consider first the onset of compression (low stress). For the case of pH < pH_{PZC} (edge-to-face configuration in *Figure 4.9a*) the mechanical interactions dominate, as opposed to the case of pH > pH_{PZC} where only electro-chemical interactions are present. Since the stiffness of the mechanical interaction is lower than the stiffness of the electro-chemical interaction (*Figure 4.7*), the specimen in edge-to-face configuration in *Figure 4.9a* is expected to exhibit lower stiffness. This conclusion is confirmed by the experimental data, since kaolin with acidic pore-water (Specimen III in *Figure 4.4b*) is characterised by a velocity of propagation lower than kaolin with alkaline pore-water (Specimen IV in *Figure 4.4b*).

Let us now consider the case of compressed assemblies (high stress). For the case of pH < pH_{PZC} (edge-to-face configuration), a number of electro-chemical interactions become

active (*Figure 4.9c*). Particles either pivot on their edge-to-face contact, or arrange in sub-parallel configuration following the disengagement of the edge-to face contact. However, the mobilised electro-chemical interaction between non sub-parallel particles appears to be relatively small, as it involves only the portion of the particle face next to the contact. The skeleton made by particles in edge-to-face contact still carries the majority of the external stress as discussed in the next section, where the force chains developing through the assemblies at high stress are discussed in detail. As a result, the specimen is still dominated by the mechanical interactions at the edge-to-face contacts. The velocity of propagation would therefore be expected to remain lower than for the case of de-activated edge-to-face interactions (*Figure 4.9d*). Again, this conclusion is confirmed by the experimental data (higher velocity of propagation was measured in kaolin with alkaline water up to a vertical stress of 590 kPa, as shown in *Figure 4.4b*).

4.4.3. Effect of dielectric permittivity on wave propagation velocity

The second DEM investigation concerns the simulation of 1-D loading of kaolin specimens saturated with fluids having different dielectric permittivity. A change in dielectric permittivity affects quantitatively the repulsion between negatively charged particle faces, either between particles pivoting on their edge-to-face contact or between particles in sub-parallel configuration. In particular, the lower is the dielectric permittivity, the higher is the repulsion generated between the negatively charged particle faces at given inter-particle distance. The quantitative comparison between the inter-particle repulsion forces in air ($\varepsilon = 1$), ethanol ($\varepsilon = 24$), and de-mineralised water ($\varepsilon = 80$) cannot be made in terms of double-layer repulsion since a double-layer does not exist in dry kaolin and, possibly, in kaolin prepared with ethanol. As a first approximation, the repulsive electro-chemical interactions

in air, ethanol, and water were scaled in the DEM model by Pagano et al. (2018) according to the value of their dielectric permittivity. *Figure 4.10* shows the contact laws for water and ethanol describing the interaction between two negatively charged sub-spheres.

Particle configuration	*Contact laws*
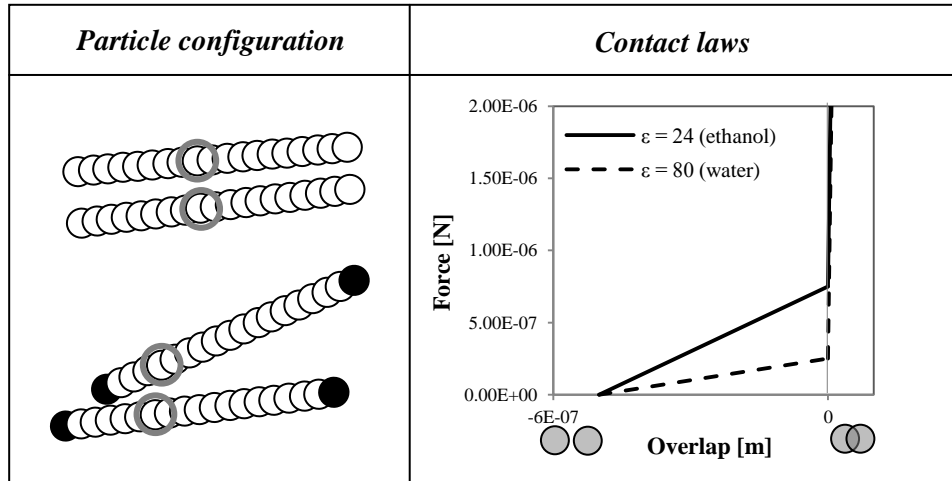
Figure 4.10. Contact laws assigned in the DEM model mimicking different dielectric permittivity of the pore-fluid.

Figure 4.11 shows the results of DEM simulations mimicking high and low dielectric permittivity of the pore-fluid (corresponding, for instance, to the case of de-mineralised water and ethanol respectively). At low vertical stress (*Figure 4.11a-b*), the configurations associated with high and low permittivity are both characterised by the presence of edge-to-face contacts, creating open structures due to the formation of 'bridges' between particles. Although the overall porosity of the two specimens is different (i.e. it is lower for the case of high dielectric permittivity, where the particle-to-particle repulsion is lower), the prevailing mode of interaction is mechanical in both cases, with only a few active electro-chemical interactions (black crosses).

As the assemblies are compressed (high stress), the specimen simulating high dielectric permittivity (e.g. water) contains more sub-parallel particles and, hence, exhibits a lower

porosity (*Figure 4.11c*). On the other hand, the specimen simulating low dielectric permittivity (e.g. ethanol) maintains a more open structure due to the higher repulsion between particles in edge-to-face configuration (*Figure 4.11d*). The two specimens both contain particles in edge-to-face configuration (mechanical contacts, open circles), plus a number of loaded electro-chemical interactions (black crosses).

The different particle configurations in *Figure 4.11* can help interpret the experimental results in terms of wave propagation velocities showed in *Figure 4.4a*. At low stress levels, the prevailing mode of interaction between particles is mechanical in both cases, and the number of mechanical contacts in the two assemblies appears to be comparable. Hence, although one assembly has a higher void ratio than the other, the velocity of propagation would be expected to be the same, as the wave is likely to travel through the same 'network' of mechanical contacts. The experimental data shown in *Figure 4.4a* confirms this behaviour: wave velocities are the same for specimens having air, ethanol, and de-mineralised water as pore-fluid (Specimens I, II and III respectively in *Figure 4.4a*) from the beginning of compression up to a vertical stress of 225 kPa.

At higher levels of stress, both mechanical and electro-chemical interactions are contributing to bear the externals stress. The number of mechanical contacts in the two specimens still seems to be comparable. At the same time, the number of loaded electro-chemical interactions appears to be higher in the specimen with high dielectric permittivity (*Figure 4.11c*). To help understand the relative contribution of the mechanical and electro-chemical interactions to the force transmission mechanisms, the force chains developing at high stress throughout the two assemblies are shown in *Figure 4.11e-f*. 'Loaded' kaolin particles (i.e. particles that transmit a non-zero mechanical force) are highlighted in black, whereas the locations of 'loaded' electro-chemical interactions are shown as grey crosses

(only the inter-particle repulsive forces at least equal to the mechanical force carried by 'loaded' particles are plotted in the figure).

The resulting pattern of black particles and grey crosses shows how the forces through the assemblies are transmitted through mechanically loaded particles, mainly sub-orthogonal, interposed by electro-chemically loaded sub-parallel particles. For the case of high dielectric permittivity (*Figure 4.11e*), the force chains seem to 'by-pass' isolated groups of particles in face-to-face configuration, which contribute little to the transmission of the forces. It seems reasonable to assume that a mechanical wave would propagate via a pattern of interconnected loaded particles and loaded electro-chemical interactions, rather than via separate clusters of particles in face-to-face configuration with weakly loaded electro-chemical interactions. On the other hand, for the case of low dielectric permittivity (*Figure 4.11f*) the force chains are rather uniformly distributed. Almost all the particles are mechanically loaded and interconnected directly, with a few electro-chemically loaded sub-parallel particles interposed between mechanically loaded particles.

The velocity of propagation through the assembly in *Figure 4.11f* would therefore be expected to be higher than that of the assembly in *Figure 4.11e* due to the higher 'density' of force chains, involving the majority of the particles. Once again, the validity of this conclusion is confirmed by the experimental evidence (*Figure 4.4a*): after a threshold value of vertical effective stress is reached (225 kPa), the velocity of propagation is higher for air, ($\varepsilon = 1$), intermediate for ethanol ($\varepsilon = 24$), and lower for de-mineralised water ($\varepsilon = 80$).

	High dielectric permittivity (ε=80)	Low dielectric permittivity (ε=24)
Low stress	a)	b)
High stress	c)	d)
High stress	e) *isolated 'weak' interactions*	f)
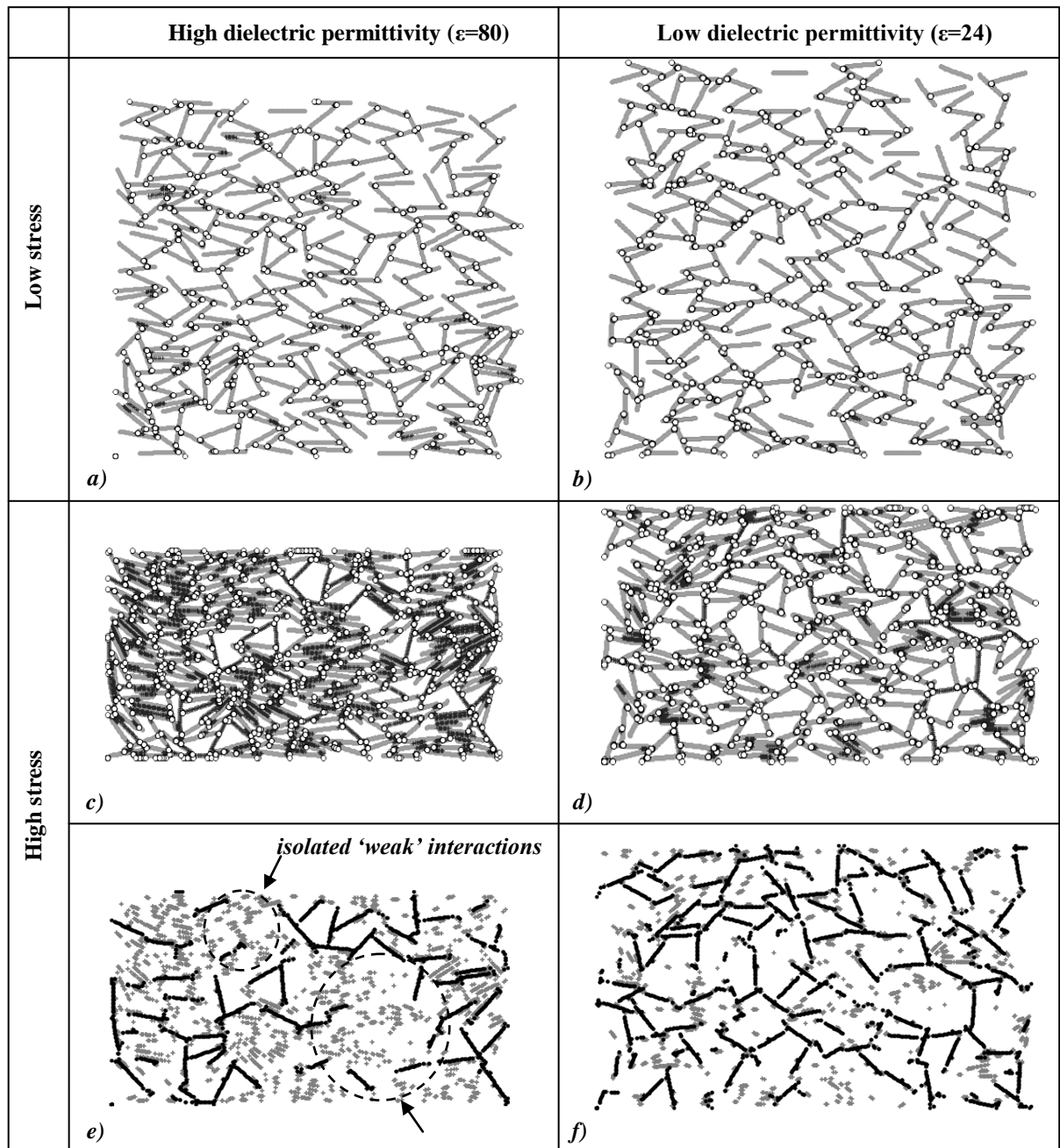
Figure 4.11.DEM configurations for one-dimensional loading of kaolin particles with active EF interaction at low and high dielectric permittivity and stress (a, b, c, d); mechanical and electro-chemical force chains at high stress (e, f).

4.5.   DISCUSSION ON THE 'EFFECTIVE' DENSITY FOR SMALL STRAIN STIFFNESS CALCULATION

The results of the experimental investigation carried out in this study have been presented in terms of the velocity of propagation of shear waves, V_s. The analysis of the experimental data showed consistent variation of V_s with the dielectric permittivity. Such a variation has been interpreted via micro-mechanical considerations based on DEM simulations.

In order to analyse the macroscopic response in terms of soil stiffness, which is the relevant parameter for practical geotechnical applications, the velocity of propagation has to be converted into a stiffness parameter. The shear modulus at very small strain G_0 is conventionally derived from the shear wave propagation velocity as:

$$G_0 = \rho \, V_s^2 \qquad\qquad\qquad 6$$

where ρ is a value ranging between bulk density and dry density depending on the degree of coupling between solid skeleton and pore-fluid (Biot, 1956; Qiu, et al., 2015).

Figure 4.12 shows the results in terms of shear modulus at very small strain G_0 against vertical effective stress. The value of G_0 was calculated according to Equation 6 by considering the bulk density for the specimens saturated with de-mineralised water and ethanol (assuming coupling between the pore-fluid and the solid skeleton) and the dry density for the dry powder.

In contrast to the velocity of propagation, the small strain stiffness does not appear to follow a consistent trend of variation with dielectric permittivity. In particular, the shear modulus at very small strains of Specimen I (dry powder, $\varepsilon = 1$) appears to be lower than the shear modulus at very small strains of Specimen II (saturated with ethanol, $\varepsilon = 24$) and Specimen III (saturated with de-mineralised water, $\varepsilon = 80$) at any level of stress, except for

the last value at about 590 kPa, where G_0 assumes roughly the same value for air and de-mineralised water. One possible explanation for this behaviour is that the values of the density used to convert the velocity of propagation into soil stiffness are not appropriate.
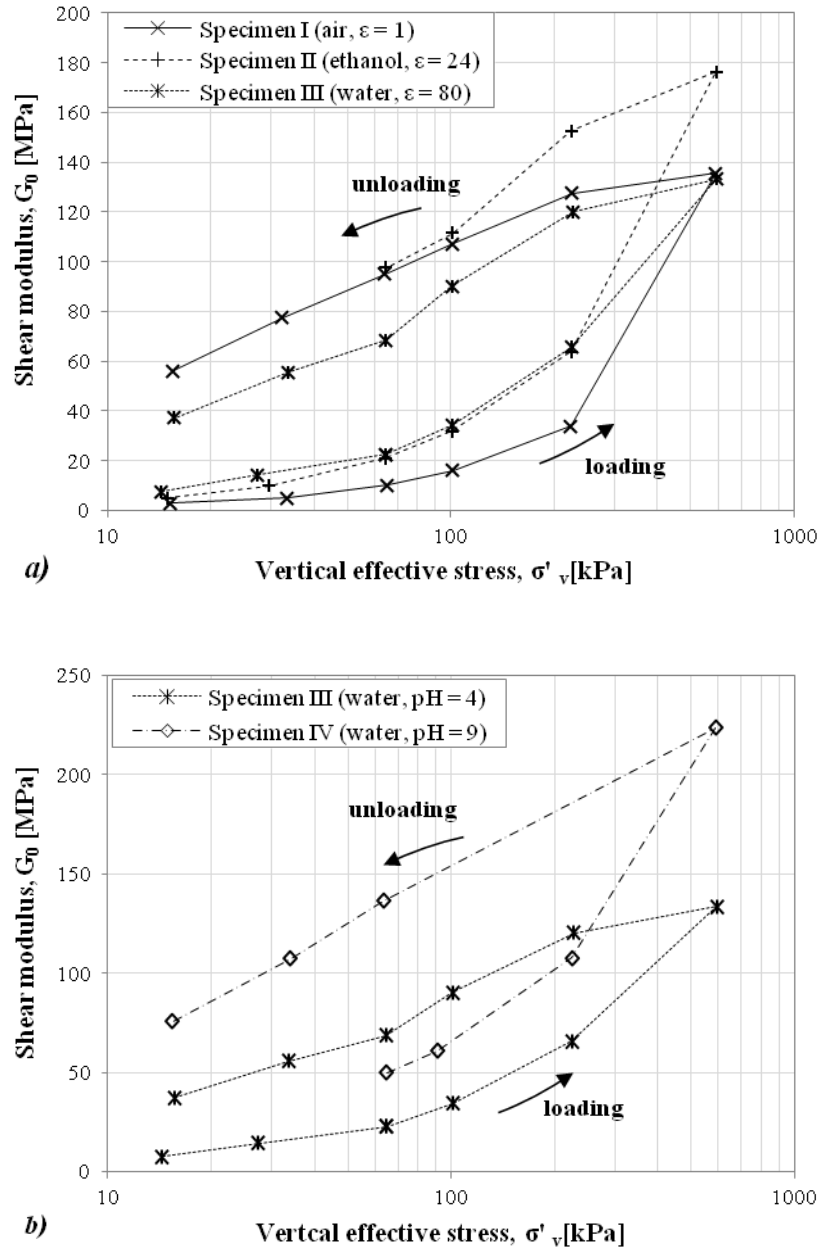
Figure 4.12. Shear modulus of kaolin clay specimens saturated with a) fluids with different dielectric permittivity, and b) fluids at different pH

To corroborate this supposition, a second exercise was carried out. The shear modulus at very small strain of Specimen I, Specimen II and Specimen III was calculated according to the empirical equation proposed by Hardin & Black (1968-1969):

$$G_0 = 1230 \frac{(2.97-e)^2}{1+e} (\sigma')^{0.5} OCR^m \qquad\qquad 7$$

where e is the void ratio of the specimen, σ' is the vertical effective stress, and OCR is the overconsolidation ratio. It is worth noticing that the original relationship proposed by Hardin & Black contains the term p' (mean effective stress) rather than σ'. The vertical effective stress is used in this study since the measurement of the radial stress (necessary for the calculation of the mean effective stress) was not taken during the tests. Nevertheless, the effect of the vertical effective stress and the effect of the mean effective stress on the qualitative variation of the small-strain stiffness are expected to be the same, this justifying the use of the vertical effective stress. The values of G_0 derived from Equation 7 were compared with the ones derived from Equation 6 on the virgin loading path (OCR = 1) as shown in *Figure 4.13*.

a)

b)
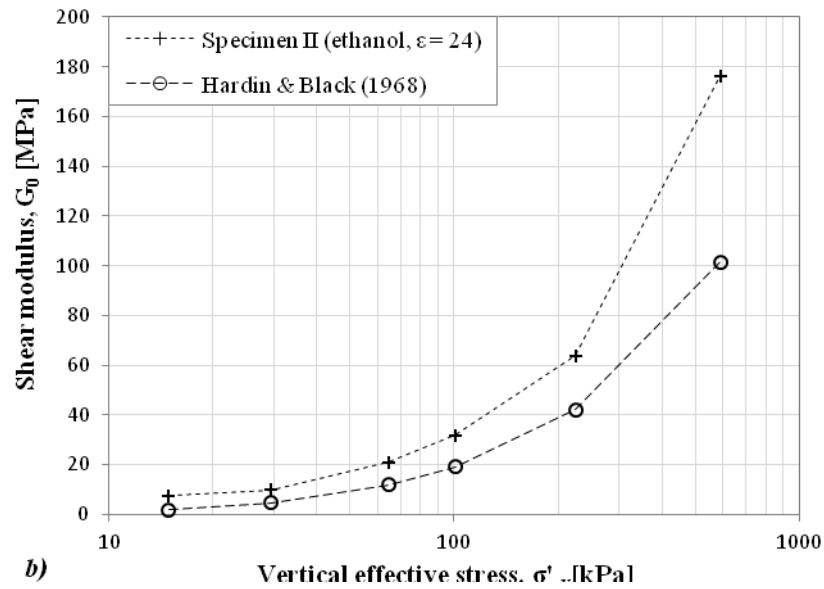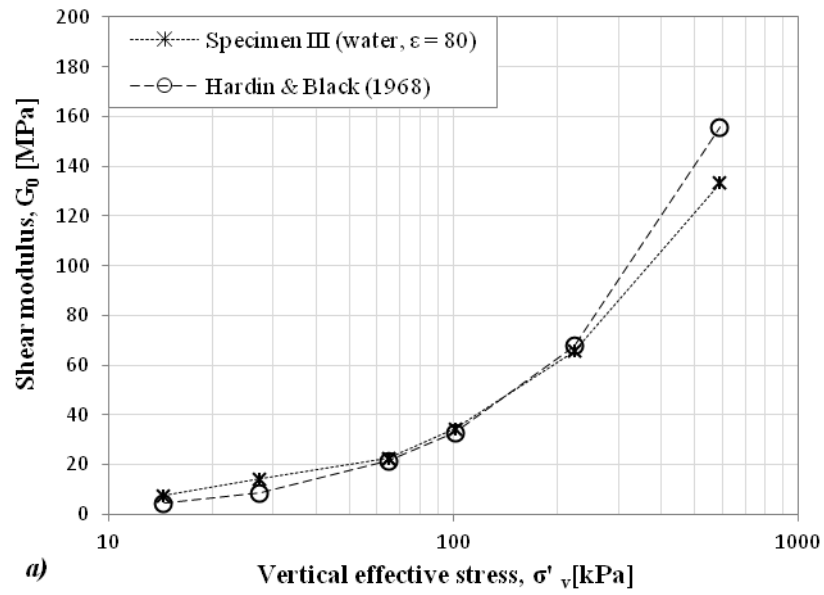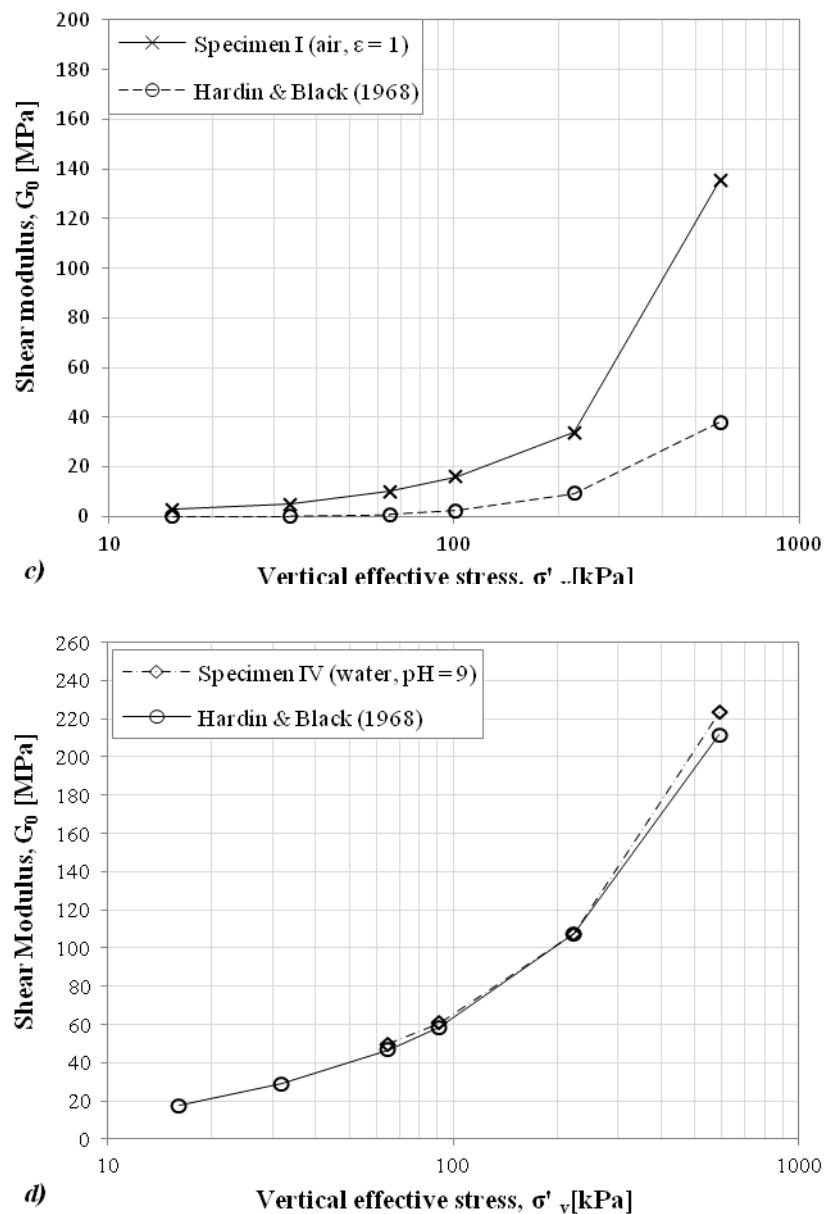
Figure 4.13. Shear modulus of kaolin clay specimens saturated with a) de-mineralised water, b) ethanol, c) air (dry powder), d) alkaline water

As expected, there is an excellent agreement for the case of water (both de-mineralised and alkaline, *Figure 4.13a* and *d*), which is not surprising as the empirical equation was calibrated on a range of water-saturated clayey materials (including kaolinite). This also confirms that the use of the vertical effective stress rather than the mean effective stress

does not significantly affect the prediction of G_0 in the adopted testing conditions. However, there is a discrepancy for the case of ethanol (*Figure 4.13b*) and air (*Figure 4.13c*), which tends to increase with the applied stress. For the case of air (dry powder), the use of an empirical equation calibrated on saturated clay may be questioned. However, the discrepancy in the case of ethanol is less intuitive as the two clay specimens are saturated with fluids with a similar viscosity. Once the different density of ethanol is accounted for, it would be expected that the empirical relation by Hardin & Black would be able to capture the experimental data, which is not the case here. Again, one possible explanation is that the value of density used to convert the velocity of propagation into soil stiffness has not been selected appropriately.

This hypothesis is further explored hereafter. The idea is that, when a mechanical wave propagates through a soil specimen, only a portion of the solids is involved in the dynamic motion caused by the propagation of the wave. Hence, only part of the solid skeleton contributes to the stiffness, as already suggested in the literature. Studies carried out on well graded transitional soils and polydisperse materials showed that the presence of clusters of finer particles may lead to a decrease in soil stiffness, due to the formation of 'weak' force chains made of particles that do not contribute to the stiffness of the macroscopic aggregate (Wichtmann & Triantafyllidis, 2009; Goudarzy, et al., 2016).

The same considerations may apply to the case of the fine-grained soil investigated in this paper. On one hand, the comparison shown in *Figure 4.13* seems to suggest that the empirical relation proposed by Hardin & Black gives a good estimate of the small-strain stiffness for the case of clay saturated with water (*Figure 4.13 a* and *d*), while it significantly underestimates G_0 for the case of dry powder and clay saturated with ethanol (*Figure 4.13 b* and *c*). However, in Section 4.4 it has also been shown that only a portion

of the solid skeleton is actually involved in the propagation of the shear waves, and that the amount of particles contributing to the soil stiffness decreases with increasing dielectric permittivity of the pore-fluid. This supposition suggests that the use of the bulk density for the calculation of G_0 from measured values of shear wave velocities (i.e. using Equation 6) may give an accurate prediction of G_0 only for low values of dielectric permittivity (e.g. air, in which case the bulk density equals the dry density), while it would overestimate the small-strain stiffness for the case of pore-fluids with high dielectric permittivity (e.g. water). This would also imply that the excellent agreement between the values of G_0 obtained using Equation 6 (via the bulk modulus) and Equation 7 (Hardin & Black) for the case of clay saturated with water in *Figure 4.13 a* and *d* is only *fictitious*, as the empirical relation proposed by Hardin & Black was indeed originally derived by interpreting the experimental results using the bulk density (which may not be representative of the portion of the solid skeleton contributing to the soil stiffness, especially for the case of clay saturated with water). As a result, the use of Equation 7 would not only lead to the underestimation of G_0 for the case of air and ethanol as already mentioned, but would also significantly overestimate the small-strain stiffness of clay saturated with water, despite the apparent excellent match in *Figure 4.13 a* and *d*.

It can be concluded that the use of existing empirical relationships may not be appropriate for the cases where the soil microstructure and its evolution are expected to affect significantly the soil stiffness. Similarly, experimental data cannot be used to derive soil stiffness directly from Equation 6, but have to be appropriately reinterpreted. The soil density used for the calculation of the small strain stiffness in Equation 6 should take into account the portion of solids (and associated pore-fluid) involved in the dynamic motion caused by the propagation of the waves. This value of density, which may be referred to as

an 'effective' soil density, would equal the bulk density if all particles contribute to force transmission, and would be lower than the bulk density if some particles cease to contribute to the force transmission. Hence, the 'effective' soil density could be characterised by a scaling factor α equal or less than unity, accounting for the fraction of particles involved in the dynamic motion during wave propagation:

$$\rho_{eff} = \alpha \cdot \rho_{bulk} \qquad\qquad 8$$

The 'corrected' small strain stiffness would then be calculated as:

$$G_0^* = \rho_{eff} \, V_s^2 \qquad\qquad 9$$

The scaling factor α can be tentatively back-calculated for the kaolin clay specimens tested in this study. The term α was assumed to be a function of both the vertical effective stress σ_v' and the dielectric permittivity of the pore-fluid ε:

$$\alpha = \alpha(\sigma_v', \varepsilon) \qquad\qquad 10$$

The term α was assumed to be equal to 1 at zero vertical effective stress irrespective of the dielectric permittivity, since the whole solid skeleton contributes to the transmission of the forces at low stress as would be inferred from the DEM configurations in *Figure 4.11a-b*. For a given ε, the term α was then assumed to decrease with increasing vertical effective stress, as an increasing portion of solids appears to cease to contribute to force transmission upon loading according to *Figure 4.11a-c*. For a given σ_v', the term α was assumed to decrease with increasing dielectric permittivity, since the amount of particles involved in the force transmission appears to be lower for higher values of ε (*Figure 4.11c-d* and *e-f*).

To quantify the function $\alpha = \alpha(\sigma_v', \varepsilon)$, two more assumptions were made. The small strain stiffness calculated for the case of dry powder using the dry density ($G_0 = \rho_{dry}\, V_s^2$) was assumed to be an accurate prediction of the real soil stiffness as discussed earlier (i.e. $\alpha = 1$ for $\varepsilon = 1$ regardless of the vertical stress). This is in line with the particle configurations shown in *Figure 4.11* for low dielectric permittivity, where almost the entire soil skeleton appears to contribute to the stiffness even at high stress levels. Furthermore, the values of G_0 for the case of kaolin with ethanol and kaolin with de-mineralised water were assumed to be equal to the values of G_0 for dry powder before the threshold effective stress (225 kPa), in line with the measured shear wave velocities. On these bases, the following expression was obtained for α:

$$\alpha = 25^{(-0.01\,\sigma_v')} + \frac{1 - 25^{(-0.01\,\sigma_v')}}{-0.0001789\,(\varepsilon - 1)^2 + 0.0247672\,(\varepsilon - 1) + 1} \qquad \textit{11}$$

The scale factor α fitted in the range 0-225 kPa was then used to extrapolate the very small strain stiffness for kaolin saturated with water and ethanol outside this range using Equation 9.

Figure 4.14 and *Figure 4.15* show the evolution of α and G_0^{*} respectively against vertical effective stress during loading for the case of $\varepsilon = 1$, $\varepsilon = 24$, and $\varepsilon = 80$. The use of the term α for the correction of G_0 led to small strain stiffness values consistent with the variation of the dielectric permittivity, in line with the experimental observations on the shear wave velocities. If the interpretation shown in *Figure 4.14* is correct, the use of bulk density in Equation 6 would lead to an overestimation of the small strain stiffness of up to 50% ($\alpha \sim 0.5$). This is clearly speculation at this stage and would require further experimental

evidence (e.g. static measurements of soil stiffness at very small strain) to corroborate the underlying assumptions.

Finally, it is worth mentioning that the expression of α in Equation 11 does not apply to the case of kaolin with de-activated edge-to-face interactions (pH > pH$_{PZC}$), as the entire soil skeleton is involved in the propagation of mechanical waves when all the particles are in face-to-face configuration. Also, Equation 11 would only be valid within the range of vertical effective stress explored in this study. Indeed, the fraction of particles contributing to the stiffness of the specimen is expected to increase after reaching a minimum, as the number of particles involved in the dynamic motion is expected to increase gradually once the vertical stress becomes high enough to bring the majority of the particles into face-to-face configuration.
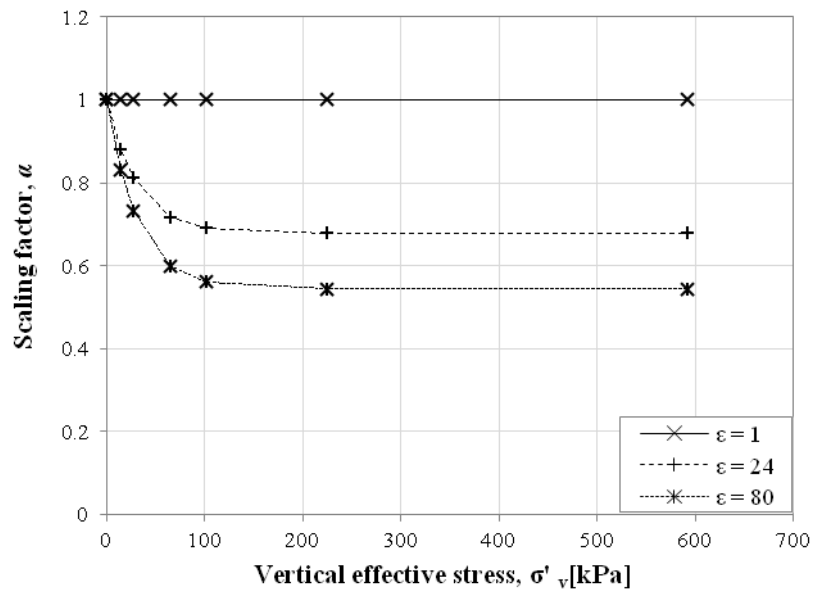
Figure 4.14. Evolution of the bulk density scaling factor with vertical effective stress at different dielectric permittivity.
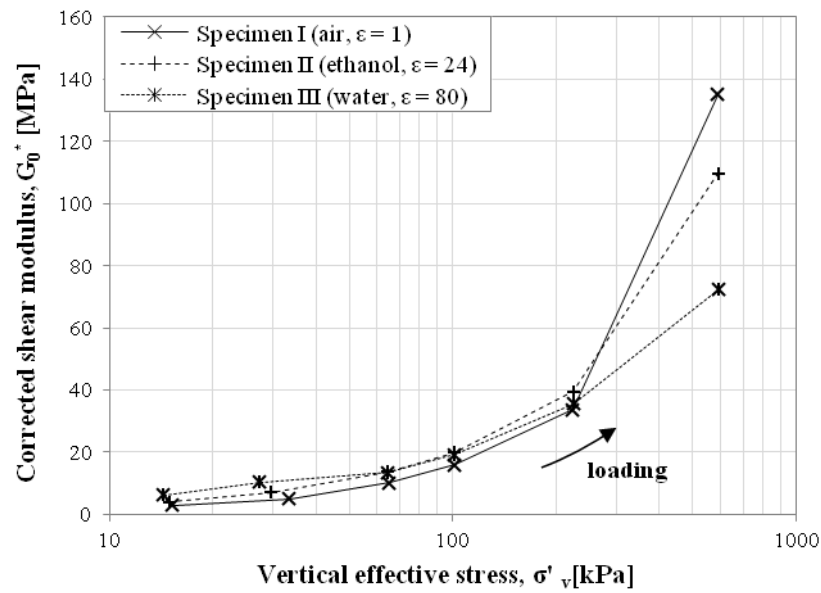
Figure 4.15. Corrected shear modulus of kaolin clay specimens saturated with fluids with different dielectric permittivity

4.6. CONCLUSIONS

This paper has presented a micromechanical interpretation of the propagation of mechanical shear waves in kaolin clay specimens subjected to one-dimensional loading. Different clay microstructures were investigated experimentally by preparing specimens with pore-fluids having different pH and dielectric permittivity. The pore-fluids having different permittivity (de-mineralised water, ethanol, and air) and different pH (de-mineralised water and alkaline water) led to experimental results in terms of wave propagation velocity that were not intuitive.

The observed response was interpreted by considering i) the different stiffness of mechanical and electro-chemical particle interactions and ii) the mechanical and electro-chemical force chains as inferred from DEM simulations. The micromechanical interpretation led to the conclusion that the velocity of propagation of mechanical shear

waves depends on the nature of the dominating inter-particle interaction and on the amount of particles contributing to the transmission of forces throughout the specimen. For the same force chain density, electro-chemical force transmission appears to lead to higher shear wave velocities than mechanical transmission. For different force chain density, assemblies characterised by uniformly distributed force chains appear to be associated with higher shear wave velocities than assemblies with poorly distributed force chains. In other words, only the portion of solids contributing to the force transmission would be involved in the dynamic motion caused by wave propagation.

Accordingly, the use of the bulk density for the calculation of soil stiffness at very small strain, G_0, was discussed. An 'effective' density was assumed to control the small strain stiffness, in turn associated with the fraction of solids involved in the propagation of shear waves. A scaling factor for the bulk density was then back-calculated from the experimental data. The correction of the small strain stiffness values based on the 'effective' density allowed the data for water, ethanol and air to regain consistency.

5. CONCLUSIONS

The aim of this thesis was to investigate experimentally the macroscopic response of unsaturated granular materials and saturated clayey geomaterials at very small strains, and to provide appropriate theoretical and numerical tools for the micromechanical interpretation/simulation of such responses.

To this end, the main goals were to:

1. Develop a micro-scale based model able to link the very small strain stiffness G_0 of unsaturated granular materials observed experimentally to the varying intergranular stress during drying-wetting cycles.

2. Develop a DEM framework (based upon the results of indirect experimental observations) suitable for the simulation of clay particles, that takes into account the presence of both mechanical and electro-chemical interactions between clay particles.

3. Provide a micromechanical interpretation of the phenomena occurring at the particle scale during the propagation of mechanical shear waves in dry and saturated clay observed experimentally, based upon the results of DEM simulations.

The conclusions drawn in this work regarding each of the aforementioned goals are described separately in the following sections.

5.1. MICROSCALE-BASED MODEL FOR G0 IN UNSATURATED GRANULAR MATERIALS

A simple conceptual model for the small strain shear modulus of unsaturated granular soils based on a micro-mechanical approach was derived in **Chapter 2**. The model requires the knowledge of the water retention characteristics of the soil, and it is based on two parameters that can be easily calibrated against the small strain stiffness measured at saturation and at residual state. The performance of the model was first assessed against the results of the experimental investigation carried out in this study on an unsaturated sand specimen. The model was able to capture (both at a qualitative and quantitative level) the higher stiffness observed experimentally along a wetting path that the 'average skeleton stress' (intended here as the product between suction and degree of saturation) fails to predict.

The model was used to elucidate the mechanisms controlling the evolution of the shear modulus at very small strains during drying-wetting cycles. In particular, it has been shown that the breadth of the water retention curve and the intensity of the intergranular stress due to the presence of the menisci have an effect on G_0. The combination of these effects can lead to the different patterns of G_0 during hydraulic hysteresis observed in the literature: when the intergranular stress at the meniscus contacts is higher than the intergranular stress at the saturated contacts and/or the water retention curves develop over a relatively narrow suction range, soil is stiffer during wetting, and the variation of G_0 is monotonic for both drying and wetting paths; when the intergranular stress at meniscus contacts becomes smaller than the one at saturated contacts and/or the water retention curves develop over a relatively large suction range, the soil becomes stiffer during drying, and the variation of G_0 is non-monotonic.

5.2. DEM FRAMEWORK FOR THE SIMULATION OF NON-ACTIVE CLAY

The lack of appropriate tools for the interpretation and simulation of the microscopic mechanisms occurring in clayey geomaterials has been addressed in **Chapter 3**. A numerical DEM framework for the simulation of assemblies of clay-like particles was first introduced on the basis of indirect experimental evidence, and then used to validate a conceptual micro-mechanical model that describes the reversible and non-reversible interparticle mechanisms occurring in non-active clays.

The proposed DEM framework addressed two main aspects of the simulation of clayey geomaterials. First, the non-spherical shape of clay particles was accounted for by creating rod-shaped particles made of bonded spherical units. Secondly, the basic linear-elastic contact laws conventionally used to simulate granular materials were modified by adding attractive and repulsive long-range forces, able to simulate the electro-chemical interactions driven by the positive/negative charge characterising the surface of clay particles.

Some aspects of the compression behaviour of kaolin clay observed by Pedrotti and Tarantino (2017) were considered, including the effect of different pore-fluid chemistries (different pH and dielectric permittivity). An alkaline pore-fluid was simulated by assigning a homogeneous negative charge to the spheres forming the rods, resulting in the development of repulsive long-range forces. An acidic pore-fluid was instead simulated by assigning a negative charge to the inner spheres of the rods and a positive charge to the end spheres, resulting in the formation of edge-to-face contacts. The effect of different dielectric permittivity of the pore-fluid was simulated by changing the magnitude of the attractive/repulsive electro-chemical forces.

A very good agreement was observed between the experimental data and the results of four sets of simulations based on the calibration of the parameter defining the slope of the electro-chemical interaction (i.e. the stiffness of the Coulombian interaction for different pore-fluids). In particular, the DEM framework was able to reproduce at a qualitative level both a) the dependency of the slope of the unloading-reloading compression curves on the pre-consolidation stress, and b) the compression behaviour upon virgin loading and along unloading-reloading paths. The ability to successfully reproduce clay behaviour at a qualitative level based on a simple calibration procedure shows promising potential for the proposed DEM framework.

5.3. MICROMECHANICAL INTERPRETATION OF WAVE PROPAGATION IN NON-ACTIVE CLAY

The effect of different clay microstructures (obtained experimentally by preparing specimens with pore-fluids having different pH and dielectric permittivity) was explored further by looking at the velocity of the propagation of mechanical shear waves during one-dimensional loading (**Chapter 4**). The observed response was interpreted by considering i) the quantitative comparison of the mechanical and electro-chemical interactions developing between two clay particles, and ii) the examination of the mechanical and electro-chemical force chains as inferred from the DEM simulations presented in **Chapter 3**.

The DEM framework represented a valuable tool for the micromechanical interpretation presented in this study. The particle scale mechanisms occurring within the simulated specimens suggested that the velocity of propagation of mechanical shear waves is strongly dependent not only on the nature of the interaction between particles (mechanical or

electro-chemical), but also on the amount of particles contributing to the force transmission. If the force chains are not uniformly distributed throughout the specimen, only the portion of solids contributing to the force transmission would be involved in the dynamic motion caused by wave propagation.

The results of the micromechanical analysis implicitly suggested that the use of the bulk density for the calculation of soil stiffness at very small strain, G_0, may not be appropriate if large portions of the soil skeleton do not contribute to the force transmission. The inconsistency of the trend of variation of G_0 inferred from the experimental data and their comparison with the small strain stiffness calculated from existing empirical models seemed to confirm this supposition. Therefore, an 'effective' soil density was introduced, and it was back-calculated from the experimental data by applying a scaling factor to the bulk density.

6. RECOMMENDATIONS FOR FUTURE WORK

6.1. SMALL STRAIN STIFFNESS IN UNSATURATED SOILS

The microscale-based model presented in **Chapter 2** seems to capture the soil response observed experimentally well, but has been validated only on the basis of the results of the experimental investigation carried out in this study. Although a lot of experimental investigations of the small strain stiffness of unsaturated soils have been carried out in the past years, most of the data that can be found in the literature are not suitable for the application of the proposed model. Some of the studies only focus on the effect of suction and degree of saturation along either a drying or a wetting path, which does not allow the effect of hydraulic hysteresis on soil stiffness to be explored. Other studies explore the water retention behaviour of the tested specimens over a range of saturation that does not extend to the residual condition. The small strain stiffness corresponding to the residual degree of saturation needs to be inferred experimentally in order to calibrate the model parameters.

It would therefore be interesting to carry out extensive experimental investigations on different types of soils (both course-grained and fine-grained soils) in order to validate the model over a wider range of experimental data. This would of course require the use of different (and more complicated) techniques for deriving the water retention behaviour of the specimens, as the hanging water column method is only suitable for soil specimens having relatively low suction air entry values. The validation of the model over a wider range of experimental data would also allow possible limitations of the model that couldn't be indentified in the present work to be found.

6.2. DEM SIMULATION OF CLAYEY GEOMATERIALS

As mentioned in **Chapter 3**, the DEM framework presented in this study for modelling clayey geomaterials is indeed characterised by a number of limitations. Since the aim of the DEM framework was to explore the potential of the newly designed contact laws for capturing the main features of the macroscopic response of non-active clay, the model had to be kept simple. In particular, the number of model parameters had to be kept to a minimum in order to simplify the calibration procedure. With this in mind, the aim of the present study has been successfully achieved.

However, further analyses would be required to improve the DEM framework for modelling clayey geomaterials. Firstly, the creation of hexagonal-shaped particles moving in a 3-D space and the use of polydisperse size-distributions would account for geometrical effects that could not be considered in the analyses carried out in this study. This would require the use of powerful computing machinery as the number of particles in the domain would increase dramatically.

Secondly, more realistic constitutive relations could be implemented in the DEM model, such as the Hertzian contact law for the mechanical interactions and the functions describing the DLVO theory for the electro-chemical interactions. Once again, this would significantly weigh down the computational procedures.

With these additions to the DEM model it is expected that a quantitative prediction of the macroscopic behaviour of clayey materials (not only during compression, but also during shearing) could be achieved.

6.3.   SMALL STRAIN STIFFNESS IN CLAYEY GEOMATERIALS

The micromechanical interpretation of the propagation of mechanical shear waves in kaolin clay specimens subjected to one-dimensional loading (**Chapter 4**) led to the conclusion that the velocity of propagation of shear waves depends on the nature of the dominating inter-particle interaction and on the amount of particles contributing to the transmission of forces throughout the specimen. In turn, it was speculated that the use of the bulk density for the calculation of soil stiffness at very small strain, G_0, may not be appropriate if large portions of the soil skeleton do not contribute to the force transmission.

This assumption could be corroborated by further experimental evidence. The values of G_0 obtained from the majority of laboratory (and field) tests, including the bender element technique, are not measured directly. When using dynamic methods, the small strain stiffness is inferred by the velocity of propagation of mechanical waves, or by the resonance frequency of the specimen, via the soil density. If the relationship used to derive the stiffness from these quantities is not correct, there is no way to infer a reliable value of soil stiffness. However, the use of different techniques for the local measurement of the shear strains would allow for the direct evaluation of the stiffness, and would therefore lead to more accurate values of G_0.

Furthermore, the conclusions drawn in this study could also be confirmed by performing further DEM analyses. The DEM framework presented in **Chapter 3** was used in this study only as a tool to investigate the force transmission mechanisms during the one-dimensional compression of clay-like particle aggregates. However, the same DEM model could be used to investigate the dynamic response of clay-like particle aggregates during the propagation of an input disturbance. This approach was not pursued in this

study as the simulation of a mechanical disturbance would have required the use of larger

virtual specimens, thus increasing the computational burden significantly.

REFERENCES

Alramah, B., Alshibli, K., Fratta, D. & Trautwein, S., 2008. A suction-control apparatus for the measurement of P and S-wave velocity in soils. *Geotech. Test. J. ,* 31(1), p. 1–12.

Anandarajah, A., 2000. Numerical simulation of one-dimensional behaviour of a kaolinite. *Géotechnique,* 50(5), pp. 509-519.

Anandarajah, A. & Amarasinghe, P. M., 2012. Discrete-element study of the swelling behaviour of Na-montmorillonite. *Géotechnique, http://dx.doi.org/10.1680/geot.12.P.012.*

Anandarajah, A. & Chen, J., 1997. Van der Waals attractive force between clay particles in water and contaminants. *Soils and foundations,* 37(2), pp. 27-37.

Andò, E. et al., 2012a. Experimental micomechanics: grain-scale observation of sand deformation. *Géotechnique,* Lett. 2(3), pp. 107-112.

Andò, E. et al., 2012b. Grain-scale experimental investigation of localised dformation in sand: a discrete particle tracking approach. *Acta Geotechnica,* 7(1), pp. 1-13.

Arroyo, M., Wood, D. M. & Greening, P. D., 2003. Source near field effects and pulse tests in soil samples. *Geotechnique,* 53(3), pp. 337-345.

Arulnathan, R., Boulanger, R. W. & Riemer, M. F., s.d. Analysis of bender element tests. *Geotech. Test. J,* 21(2), p. 120–131.

Asslan, M. & Wuttke, F., 2012. Wave Velocity Change and Small-Strain Stiffness in Unsaturated Soils: Experimental Investigation. *In: Mancuso C., Jommi C., D'Onza F. (eds) Unsaturated Soils: Research and Applications. Springer, Berlin, Heidelberg.*

Atkinson, J. H., 2000. Non-linear soil stiffness in routine design. *Géotechnique,* 50(5), pp. 487-508.

Biot, M. A., 1956. Theory of propagation of elastic waves in a fluid-saturated porous solid. I. Low-frequency range. *The Journal of the Acoustical Society of America,* 28(2), pp. 168-178.

Biot, M. A., 1956. Theory of propagation of elastic waves in a fluid-saturated porous solid. II.Higher frequency range. *The Journal of the Acoustical Society of America ,* 28(179).

Bishop, A. W., 1959. The principle of effective stress. *Tek. Ukeblad,* Volume 39, p. 859–863.

Blewett, J., Blewett, I. J. & Woodward, P. K., 2000. Phase and amplitude responses associated with the measurement of shear-wave velocity in sand by bender elements. *Canadian Geotechnical Journal,* Volume 37, pp. 1348-1357.

Bolt, G., 1956. Physico-chemical analysis of the compressibility of pure clays. *Géotechnique,* 6(2), p. 86–93.

Bolton, M. D., Nakata, Y. & Cheng, Y. P., 2008. Micro- and macro-mechanical behaviour of DEM crushable materials. *Géotechnique,* 58(6), pp. 471-480.

Boso, M., Tarantino, A. & Mongiovì, L., 2005. Shear strength behaviour of a reconstituted clayey silt. *Unsaturated soils - Mancuso & Tarantino (eds) - 2005 Taylor & Francis Group, London,* pp. 9-14.

Brignoli, E. G. M., Gotti, M. & Stokoe, K. H. I., 1996. Measurement of shear waves in laboratory specimens by means of piezoelectric transducers. *Geotech. Test. J ,* 19(4), p. 384–397.

Carroll, S. A. & Walther, J. V., 1990. Kaolinite dissolution at 25, 60 and 80°C. *Am. J. Sci,* 290(7), p. 797–810.

Cavarretta, I., Coop, M. R. & O' Sullivan, C., 2010. The influence of particle characteristics on the behaviour of coarse grained soils. *Géotechnique,* 60(6), pp. 413-423.

Chang, C. S. & Liao, C. L., 1994. Estimates of elastic modulus for media of randomly packed granules. *Appl. Mech. Rev. 47, S197–S206.*

Cheng, Y. P., Nakata, Y. & Bolton, M. D., 2003. Discrete element simulation of crushable soil. *Géotechnique,* 53(7), p. 633–641.

Clayton, C. R. I., 2011. Stiffness at small strain: research and practice. *Géotechnique,* 61(1), p. 5–37.

Clayton, C. R. I. & Heymann, G., 2001. Stiffness of geomaterials at very small strains. *Géotechnique,* 51(3), p. 245–255.

Clayton, C. R. I., Matthews, M. C. & Simons, N. E., 1995b. Site investigation.

Cleary, P. W. & Hoyer, D., 2000. Centrifugai mill charge motion and power draw: comparison of DEM predictions with experiment. *Int. J. Min. Proc,* Volume 59, pp. 131-148.

Cundall, P. A. & Strack, O. D. L., 1979. A discrete numerical model for granular assemblies. *Géotechnique,* 29(1), p. 47–65.

Derjaguin, B. & Landau, L., 1941. Theory of the stability of strongly charged lyophobic sols and of the adhesion of strongly charged particles in solutions of electrolytes. *Acta Physicochimica URSS,* 14(6), p. 633–662..

Digby, P. J., 1981. The effective moduli of porous granular rock. *J. Appl. Mech. ,* Volume 48, p. 803–808.

Dong, Y. & Lu, N., 2016. Correlation between small-strain shear modulus and suction stress in capillary regime under zero total stress conditions. *Journal of Geotechnical and Geoenvironmental Engineering, 10.1061/(ASCE)GT.1943-5606.*

Duffy, J. & Mindlin, R. D., 1957. Stress-strain relations and vibrations of granular media. . *J. Appl. Mech.ASME,* 24(4), pp. 585-593.

Dyer, M., Jamiolkowski, M. & Lancellotta, R., 1986. Experimental soil engineering and models for geomechanics. *Proc. 2nd Int. Symp. on Numer. Models Geomech., Ghent,* p. 873–906.

Dyvik, R. & Madshus, C., 1985. Lab measurements of Gmax using bender element. *Proc., ASCE Convention on Advances in the Art of Testing Soils under Cyclic Conditions,* p. 186–196.

Fernandez, A. L., 2000. Tomographic imaging the state of stress. *PhD thesis Civil Engineering, Georgia Institute of Technology, Atlanta.*

Fisher, R. A., 1926. On the capillary forces in an ideal soil; correction on formulae given by W. B. Haines. *Journal of Agricultural Science,* Volume 16, pp. 492-505.

Goudarzy, M., König, D. & Schanz, Z., 2016. Small strain stiffness of granula rmaterials containing fines. *Soils and Foundations,* 56(5), p. 756–764.

Gouy, G., 1910. Constitution of the electric charge at the surface of an electrolyte. *J. Physics,* 9(4), p. 457–467.

Greening, P. D. & Nash, D. F. T., 2004. Frequency domain determination of G0 using bender elements. *Geotechnical Testing Journal,* 72(3), p. 1–7.

Guo, N. & Zhao, J., 2012. The signature of shear-induced anisotropy in granular media. *Computers and Geotechnics,* Volume 47, pp. 1-15.

Hardin, B. O., 1978. The Nature of Stress Stain Behavior of Soils. *Earthquake Engineering and Soil Dynamics, ASCE,* pp. 3-90.

Hardin, B. O. & Black, W. L., 1968. Vibration modulus of normally consolidated clay. *Journal of the Soil Mechanics and Foundations Division, ASCE,* 94(SM2), pp. 353-369.

Hardin, B. O. & Black, W. L., 1969. Closure to: Vibration modulus of normally consolidated clay. *Journal of the Soil Mechanics and Foundations Division, ASCE,* 95(SM6), pp. 1531-1539.

Hardin, B. O. & Drnevich, V. P., 1972. Shear modulus and damping in soils: design equations and curves. *Journal of the Soil Mechanics and Foundations Division, ASCE,* 98(SM7), pp. 667-692.

Hardin, B. O. & Richart, F. E., 1963. Elastic wave velocities in granular soils. *Journal of Soil Mechanics and Foundations Division, ASCE,* 89(SM1), pp. 33-65.

Huertas, F. J., Chou, L. & Wollast, R., 1998. Mechanism of kaolinite dissolution at room temperature and pressure: Part 1. Surface speciation. *Geochimica et Cosmochimica Acta,* 62(3), p. 417–431.

Iwasaki, T. & Tatsuoka, F., 1977. Effects of grain size and grading on dynamic shear moduli of sand. *Soils and Foundations,* 17(3), pp. 19-35.

Iwasaki, T., Tatsuoka, F., Tokida, K. & Yasuda, S., 1978. A practical method for assessing soil liquefaction potential based on case studies at various sites in Japan. *Proc., 2nd Int. Conf. on Microzonation, San Francisco,* p. 885−896.

Iwashita, K. & Oda, M., 1997. Rolling resistance at contacts in simulation of shear band development by DEM. *Journal of Engineering Mechanics,* 124(3), p. 285–292.

Jommi, C., 2000. Remarks on the constitutive modelling of unsaturated soils. *Experimental evidence and theoretical approaches in unsaturated soils (eds A. Tarantino and C. Mancuso). Rotterdam: Balkema,* pp. 139-153.

Jovicic, V. & Coop, M. R., 1997. Interpretation of bender element tests. *Géotechnique,* 47(3), p. 875.

Jovicic, V., Coop, M. R. & Simic, M., 1996. Objective criteria fordetermining Gmax from bender element tests. *Geotechnique,* 46(2), p. 357–362.

Kawaguchi, T., Mitachi, T. & Shibuya, S., 2001. Evaluation of shea rwave travel time in laboratory bender element test. *Proc., 15th Int.Conf. on Soil Mechanics and Geotechanics Engineering ,* p. 155–158.

Kawamoto, R., Andò, E., Viggiani, G. & Andrade, J. E., 2018. All you need is shape: Predicting shear banding in sand with LS-DEM. *Journal of the Mechanics and Physics of Solids,* Volume 111, pp. 375-392.

Khosravi, A. & McCartney, J. S., 2011. Resonant column test for unsaturated soils with suction-saturation control. *Geotechnical Testing Journal,* 36(6), pp. 1-10.

Khosravi, A. & McCartney, J. S., 2012. Impact of hydraulic hysteresis on the small-strain shear modulus of low plasticity soils. *Journal of Geotechnical and Geoenvironmental Engineering, 10.1061/(ASCE)GT.1943-5606,* p. 1326–1333.

Khosravi, A. et al., 2016. Characterizing the variation of small strain shear modulus for silt and sand during hydraulic hysteresis. *Proc. 3rd European Conference on Unsaturated Soils "E-UNSAT 2016" - E3S Web Conferences,* Volume 9.

Kokusho, T. & Esashi, Y., 1981. Cyclic triaxial test on sands and course materials. *In: Proceedings of the 10th international conference on soil mechanics and foundation engineering, Stockholm,* Volume 1, pp. 673-676.

Kruyt, N. P., 2010. Three-dimensional lattice-based dispersion relations for granular materials. *AIP Conference Proceedings,* Volume 1227.

Kruyt, N. P. & Rothenburg, L., 1998. Statistical theories for the elastic moduli of two-dimensional assemblies of granular materials. *International Journal of Engineering Science,* Volume 36, pp. 1127-1142.

Labra, C., Rojek, J. & Oñate, E., 2008. Labra, C., Rojek, J., Oñate, E. et al.. *Acta Geotechnica. https://doi.org/10.1007/s11440-008-0071-2.*

Langston, P. A., Al-Awamleh, M. A., Fraige, F. Y. & Asmar, B. N., 2004. Distinct element modelling of non-spherical frictionless particle flow. *Chemical Engineering Science ,* Volume 59, pp. 425-435 .

Lee, J. & Santamarina, J. C., 2005. Bender Elements: performance and signal interpretation. *Journal of Geotechnical and Geoenvironmental Engineering,* 131(9), pp. 1063-1070.

Leong, E. C., Yeo, S. H. & Rahardjo, H., 2005. Measuring shear wave velocity using bender elements. *Geotechnical Testing Journal,* 28(5), pp. 488-498.

Liao, C. -L. & Chang, T. -C., 1997. A generalized constitutive relation for a randomly packed particle assembly. *Computers and Geotechnics ,* 20(3/4), pp. 345-363.

Lings, M. & Greening, P., 2001. A novel bender/extender element for soil testing. *Géotechnique,* 51(8), p. 713–717.

Luding, S., 2005. Anisotropy in cohesive, frictional granular media. *Journal of Physics Condensed Matter,* 17(24), p. S2623–S2640.

Luding, S., 2008. Cohesive, frictional powders: contact models for tension. *Granular Matter10: 235. https://doi.org/10.1007/s10035-008-0099-x.*

Lu, N. & Likos, W. J., 2006. Suction stress characteristic curve for unsaturated. *J. Geotech. Geoenviron. Eng. ,* Volume 132, p. 131–142.

Magnanimo, V. et al., 2008. Characterizing the shear and bulk moduli of an idealized granular material. *Europhysics Letters,* 81(3).

Makse, H. A., Gland, N., Johnson, D. L. & Schwartz, L., 2004. Granular packings: Nonlinear elasticity, sound propagation, and collective relaxation dynamics. *Physical Review E,* 70(6).

Mancuso, C., Vassallo, R. & d'Onofrio, A., 2002. Small strain behaviour of a silty sand in controlled-suction resonant column-torsional shear tests. *Canadian Geotechnical Journal,* 39(1), pp. 22-31.

Marinho, F. A. M., Chandler, R. J. & Crilly, M. S., 1995. Stiffness measurements on an unsaturated high plasticity clay using bender elements. *Unsaturated soils. Proc. 1st International Conference on Unsaturated Soils, UNSAT 95, Paris, France, 6-8 September 1995. A.A. Balkema, Rotterdam,* Volume 1, pp. 535-539.

Matasovic, M. & Vucetic, M., 1995. Generalized cyclic degradation-pore pressure generation model for clays. *Journal of Geotechnical Engineering,* 121(1), pp. 33-42.

Mendoza, C. E., Colmenares, J. E. & Merchàn, V. E., 2005. Stiffness of an unsaturated compacted clayey soil at very small strains. *Proc., Int. Symp. on Advanced Experimental Unsaturated Soil Mechanics, ASCE, Reston, VA,* pp. 199-204.

Mindlin, R. D., 1949. Compliance of Elastic Bodies in Contact. *Journal of Applied Mechanics,* Volume 16, pp. 259-268.

Mitchell, J. & Soga, K., 2005. *Fundamentals of soil behavior.* Hoboken, NJ, USA: John Wiley and Sons Inc.

Moore, C. A. & Mitchell, J. K., 1974. Electromagnetic forces and soil strength. *Géotechnique,* 24(4), pp. 627-640 .

Mouraille, O., 2009. *PhD thesis: Sound propagation in dry granular materials: discrete element simultions, theory, and experiments.* Enschede: s.n.

Mouraille, O., 2009. Sound propagation in dry granular materials : discrete element simulations, theory, and experiments. *PhD thesis.*

Ng, C. W. W. & Xu, J., 2012. Effects of current suction ratio and recent suction history on small-strain behaviour of an unsaturated soil. *Canadian Geotechnical Journal,* Volume 49, pp. 226-243.

Ng, C. W. W., Xu, J. & Yung, S. Y., 2009. Effects of imbibition drainage and stress ratio on anisotropic stiffness of an unsaturated soil at very small strains. *Canadian Geotechnical Journal,* 46(9), pp. 1062-1076.

O' Sullivan, C., Bray, J. D. & Cui, L., 2006. Experimental validation of particle-based discrete element methods. *GeoCongress 2006, https://doi.org/10.1061/40803(187)5.*

O'Donovan, J. et al., 2016 . Micromechanics of seismic wave propagation in granular materials. *Granular Matter. 18: 56, https://doi.org/10.1007/s10035-015-0599-4.*

O'Donovan, J., O'Sullivan, C. & Marketos, G., 2012. Two-dimensional discrete element modelling of bender element tests on an idealised granular material. *Granular matter,* 14(6), p. 733–747.

O'Donovan, J. & O'Sullivan, C., 2012. Two-dimensional discrete element modelling of bender element tests on an idealised granular material. *Granular matter,* Volume 14, pp. 733-747.

Oh, W. T. & Vanapalli, S. K., 2014. Semi-empirical model for estimating the small-strain shear modulus of unsaturated non-plastic sandy soils. *Geotechnical and Geological Engineering,* 32(2), pp. 259-271.

Olson, R. E. & Mesri, G., 1970. Mechanisms controlling the compressibility of clays. *J. Am. Soc. Civ. Engrs. 96, SM6,* pp. 1853-1878.

Pedrotti, M. & Tarantino, A., 2017. An experimental investigation into the micromechanics of non-active clays. *Géotechnique. http://dx.doi.org/10.1680/jgeot.16.P.245.*

Peroni, N. & Tarantino, A., 2005. *Measurement of osmotic suction using the squeezing technique. In: Schanz T. (eds) Unsaturated Soils: Experimental Studies. Springer Proceedings in Physics, vol 93.* s.l.:Springer, Berlin, Heidelberg.

Picornell, M. & Nazarian, S., 1998. Effects of soil suction on the low-strain shear modulus of soils. *In Proceedings of the Second International Conference on Unsaturated Soil, Beijing, China,* Volume 2, p. 102–107.

Prange, B., 1981. Resonant column testing of railroad ballast. *In: Proceedings of the 10th international conference on soil mechanics and foundation engineering, Stockholm,* Volume 1.

Qian, X., Gray, D. H. & Woods, R. D., 1993. Voids and granulometry: effects on shear modulus of unsaturated sands. *Journal of Geotechnical Engineering,* 119(2), pp. 295-314.

Qiu, T. et al., 2015. Effective soil density for small-strain shear waves in saturated granular materials. *J. Geotech. Geoenviron. Eng,* 141(9).

Radjai, F. & Wolf, D. E., 1998. Features of static pressure in dense. *Granular Matter,* Issue 11, p. 3–8.

Radjai, F., Wolf, D. E., Jean, M. & Moreau, J. -J., 1998. Bimodal character of stress transmission in granular packings. *Phys. Rev. Lett.,* 80(1), p. 61–64.

Ramberg, W. & Osgood, W. R., 1943. Description of stress-strain curves by three parameters. *Technical Note. Washington, D.C., USA: National Advisory Committee for Aeronautics,* Issue 902.

Rampello, S., Viggiani, G. & Amorost, A., 1997. Small-strain stiffness of reconstitued clay compressed along constant triaxial effective stress ratio path. *Géotechnique,* 47(3), pp. 475-489.

Roy, S., Singh, A., Luding, S. & Weinhart, T., 2016. Micro-Macro Transition and Simplified Contact Models for wet granular materials. *DOI10.1007/s40571-015-0061-8.*

Sanchez-Salinero, I., Rosset, J. M. & Stokoe, K., 1986. Analytical studies of body wave propagation and attenuation. *Rep. N° GR-86-15, Univ. of Texas, Austin, Tex.*

Santamarina, J. C. & Cascante, G., 1996. Stress anisotropy and wave propagation: A micromechanical view. *Can. Geotech. J.,* 33(5), p. 770–782.

Santamarina, J. C. & Fam, M. A., 1997. Interpretation of bender element tests - discussion. *Géotechnique,* 47(4), p. 873–875.

Sawangsuriya, A., Edil, T. B. & Bosscher, P. J., 2009. Modulus-suction moisture relationship for compacted soils in post compaction state. *Journal of Geotechnical and Geoenvironmental Engineering, 10.1061/(ASCE)GT.1943-5606.0000108,* p. 1390–1403.

Senthilmurugan, T. & Ilamparuthi, K., 2005. Study of compaction characteristics and strength through ultrasonic methods. *Proc. of Geo-Frontiers Conference, Austin, ASCE, Geotechnical Special Publication no. 130,* pp. 1-12.

Shirley, D. J. & Hampton, L. D., 1978. Shear wave measurements in laboratory sediments. *Journal of Acoustic Society of America,* 63(2), p. 607–613.

Silbert, L. E. et al., 2001. Granular flow down an inclined plane: Bagnold scaling and rheology. *Physical Review E,* 64(051302).

Sorensen, K. K., Baudet, B. A. & Simpson, B., 2010. Influence of strain rate and acceleration on the behaviour of reconstituted clays at small strains. *Géotechnique,* 60(10), pp. 751-763.

Sposito, G., 1984. *The surface chemistry of soils.* New York, NY,USA: Oxford University Press.

Stokoe, K. H. et al., 1995. Effects of various parameters on the stiffness and damping of soils at small to medium strains. *Pre-failure Deformation of Geomaterials, Balkema, Rotterdam,* Volume 2, pp. 785-816.

Takkabutr, P., 2006. Experimental Investigations on small-strain stiffness properties of partially saturated soils via resonant column and bender element testing. *PhD Dissertation, University of Texas at Arlington.*

Thornton, C., Yin, K. K. & Adams, M. J., 1996. Numerical simulation of the impact fracture and fragmentation of agglomerates. *J. Phys. D: Appl. Phys,* Volume 29, p. 424–435.

Tunuguntla, D. R., Thornton, A. R. & Weinhart, T., 2015. From discrete elements to continuum fields: Extension to bidisperse systems. *Comp. Part. Mech., DOI 10.1007/s40571-015-0087-y.*

van Genuchten, M., 1980. A closed-form equation for predicting the hydraulic conductivity of unsaturated soils. *Soil Sci. Soc. Am. J. ,* Volume 44, p. 892–898.

Vanorio, T., Prasad, M. & Nur, A., 2003. Elastic properties of dry clay mineral aggregates, suspensions and sandstones. *Geophys. J. Int.,* Volume 155, p. 319–326.

Verwey, E. J. W., Overbeek, J. T. G. & Van Nes, K., 1948. *Theory of the stability of lyophobic colloids: the interaction of sol particles having an electric double layer.* New York, NY, USA: Elsevier.

Viana da Fonseca, A., Ferreira, C. & Fahey, M., 2009. A framework for interpreting bender element tests, combining time-domain and frequency-domain methods. *Geotechnical Testing Journal,* 32(2), pp. 1-17.

Viggiani, G. & Atkinson, J. H., 1995a. Interpretation of bender element tests. *Géotechnique,* 45(1), pp. 149-154.

Viggiani, G. & Atkinson, J. H., 1995b. Stiffness of fine grained soils at very small strains. *Géotechnique,* 45(2), pp. 249-265.

Waltonn, K., 1987. The effective elastic moduli of a random packing of spheres. *Journal of the Mech. Phys. Solids,* Volume 35, p. 213–226.

Weidinger, D. M., Ge, L. & Stephenson, R. W., 2009. Ultrasonic pulse velocity tests on compacted soil. *Characterization, Modeling, and Performance of Geomaterials, Hunan, ASCE, Geotechnical Special Publication, no. 189,* pp. 150-155.

Wichtmann, T. & Triantafyllidis, T., 2009. Influence of the grain-size distribution curve of quartz sand on the small strain shear modulus Gmax. *J. Geotech. Geoenviron. Eng,* 135(10), pp. 1404-1418.

Willet, C. D., Adams, M. J., Johnson, S. A. & Seville, J. P. K., 2000. Capillary bridges between two spherical bodies. *Langmuir.*

Wong, K. S., Mašín, D. & Ng, C. W. W., 2014. Modelling of shear stiffness of unsaturated fine grained soils at very small strains. *Computers and Geotechnics,* Volume 56, pp. 28-39.

Yamashita, S. et al., 2009. Interpretation of international parallel test on the measurement of Gmax using bender elements. *Soils and Foundations,* 49(4), p. 631–650.

Yao, M. & Anandarajah, A., 2003. Three-Dimensional Discrete Element Method of analysis of clay. *J. Eng. Mech,* Volume 129, pp. 585-596.

‘Particle-scale mechanisms controlling the response of granular and clayey geomaterials at very small strains’

LIST OF FIGURES AND TABLES

'Particle-scale mechanisms controlling the response of granular and clayey geomaterials at very small strains'

7. APPENDIX A– PREPARATION OF BENDER ELEMENTS IN A MODIFIED TRIAXIAL CELL APPARATUS

In this study, the Bender Element (BE) technique was adopted in order to measure the velocity of propagation of mechanical shear waves through sand and kaolin specimens. BEs were constructed and embedded in the pedestal and top cap of a standard triaxial cell apparatus (maximum specimen diameter 100 mm). The procedure for the preparation and installation of the sensors is described in details. The steps for the preparation procedure include:

i) preparation of rubber moulds for BE coating;

ii) preparation of rubber moulds for BE insertion in plastic casings;

iii) 3D-printing of plastic casings for BE embedding in the top cap and base pedestal;

iv) BE coating;

v) BE wiring, shielding and grounding and re-coating (if applicable);

vi) BE insertion in plastic casings and embedding in the top cap and base pedestal.

7.1. RUBBER MOULDS FOR BE COATING

Since BE sensors are designed to be used in the presence of water (i.e. within saturated or unsaturated soil specimens), a covering water-proof layer has to be provided in order to prevent the water from getting in contact with the sensors and the whole electrical circuit. In this study, the coating procedure (see Section 7.4) was carried out within purposely designed rubber moulds, which could be easily removed and disposed of after use.

Figure A-1 shows the steps followed for the creation of the rubber moulds. A three-piece metal casing was manufactured in order to accommodate the rubber during its curing

process and give the required shape to the rubber moulds once cured (Figure A-1a,1b). A two-part RTV silicon rubber (Polycraft HT-3120 RTV High Temperature Silicone) was used to create suitable moulds for the coating procedure. For each mould, 10 grams of red silicone base were poured in a plastic cup and mixed with 1 gram of curing agent (mix ratio 10:1), in order to obtain a fluid mixture. The mixture was then poured in the three-piece metal casing (Figure A-1c), which had been previously put together and sealed with the aid of grease in order to prevent the leakage of liquid rubber through the junction surfaces. The liquid rubber was left to settle and cure for at least 8 hours.Once cured, the hardened rubber was de-moulded by dismantling the metal casing (Figure A-1d, 1e, 1f), which could then be re-used for the preparation of other moulds.
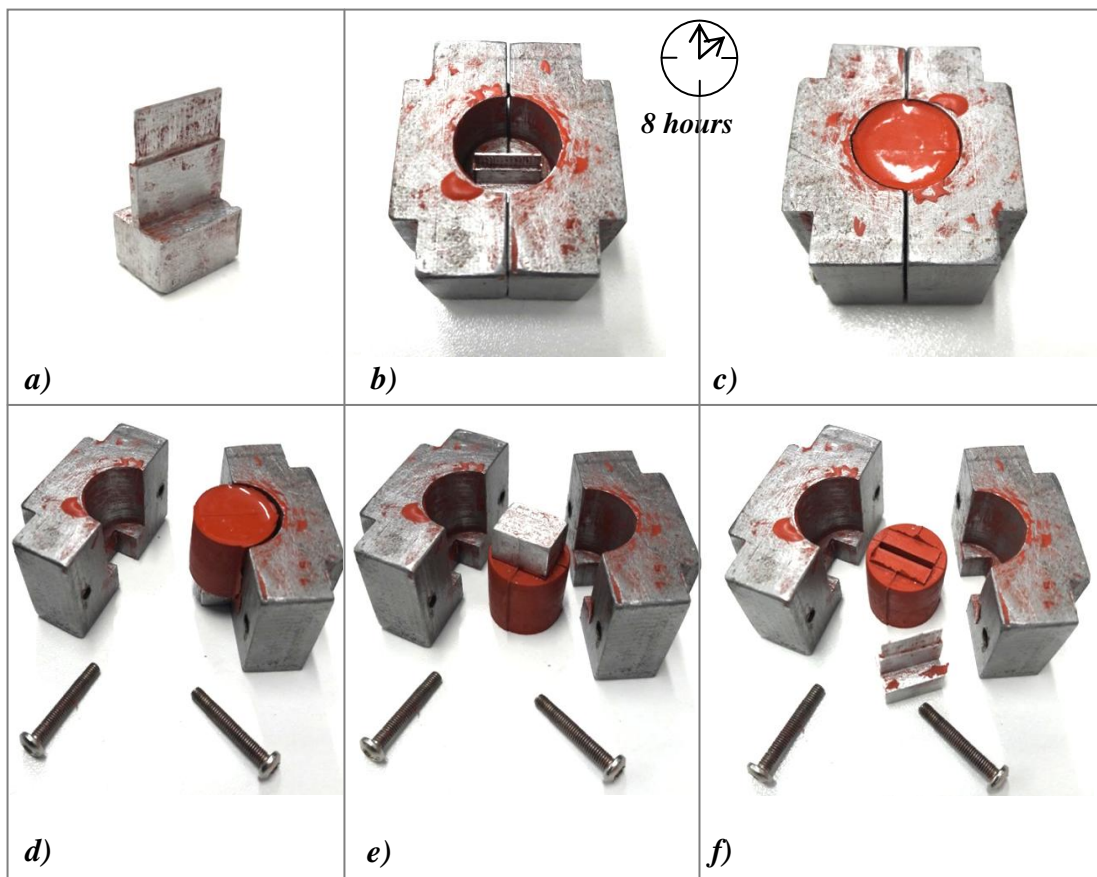
Figure A-1: Preparation of rubber moulds for BE coating

7.2.   RUBBER MOULDS FOR BE INSERTION IN PLASTIC CASINGS

Using a similar procedure, rubber moulds for the embedment of the BE into 3D-printed plastic casings were casted using the same silicon rubber and a two-piece metal casing. The liquid rubber-curing agent mixture was prepared and poured in the metal casing and allowed to settle and harden for at least 8 hours. Figure A-2a, 2b show the metal cast used to give the required shape to the rubber mould. Figure A-2c, 2d show the process of de-moulding and the rubber mould at the end of curing respectively.

8 hours
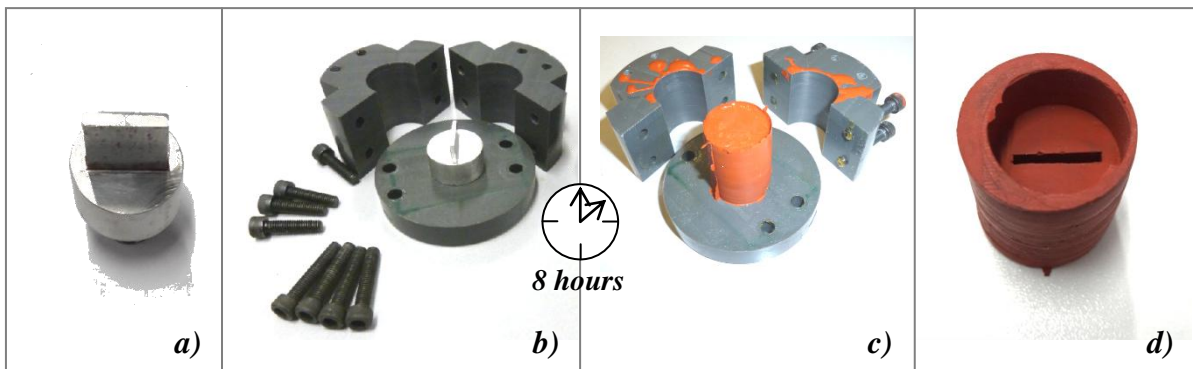
Figure A-2: Metal cast and rubber mould for BE insertion in plastic casings

7.3.   3D-PRINT OF PLASTIC CASINGS FOR BE SUPPORT

Plastic casings for the support of the BE sensors and their insertion in the triaxial cell pedestal and top cap were designed and manufactured using a Ultimaker[2] 3D printer. Autocad 3D drawings of the casings were imported in the Ultimaker software Cura and printed using PLA (polyactic acid) filaments.

Figure A-3: Ultimaker^2 3D printer and 3D-printed PLA casings

7.4. BE COATING WITH EPOXY CASTING RESIN

As previously mentioned in Section 7.1, BE need to be covered with a thin layer of water-proof coating in order to avoid electrical issues (e.g. depolarization of the piezoelectric elements, short circuit). In this study, water-proofing of the sensors was achieved by covering the upper half of the sensitive piezoelectric elements with a thin layer (about 0.5 mm thickness) of a transparent, low viscosity epoxy resin (Araldite DBF Resin + Aradur Hardener HY956). The elements were coated with the aid of the rubber moulds described in Section 7.1. The coating procedure is shown in Figure A-4.

Figure A-4a and b show a parallel BE (prior coating) and the rubber mould respectively. The sensor was inserted into the rubber mould (Figure A-4c) with its upper edge facing the top of the mould, in order to coat only the half of the piezoelectric element that isn't meant for wiring. For each sensor, 5 grams of epoxy resin were poured in a plastic cup and mixed with 1 gram of curing agent (mix ration 10:2), in order to obtain a liquid mixture. The mixture was then slowly poured into the small gap between the rubber and the sensor with the aid of a needle. This procedure had to be carried out slowly and carefully in order to avoid the creation of air bubbles within the epoxy and at the sensor-rubber interface, these

potentially leading to ineffective water-proofing. Once epoxy had reached and covered the upper edge of the sensor, the mixture was left to settle and cure for at least 12 hours.

After 12 hours, the rubber mould was carefully cut in half with a knife in order to retrieve the sensor (Figure A-4d). A water-proof layer of hardened epoxy around the upper half of the sensor was obtained (Figure A-4e).

Figure A-4f shows both a series BE and a parallel BE before and after coating.
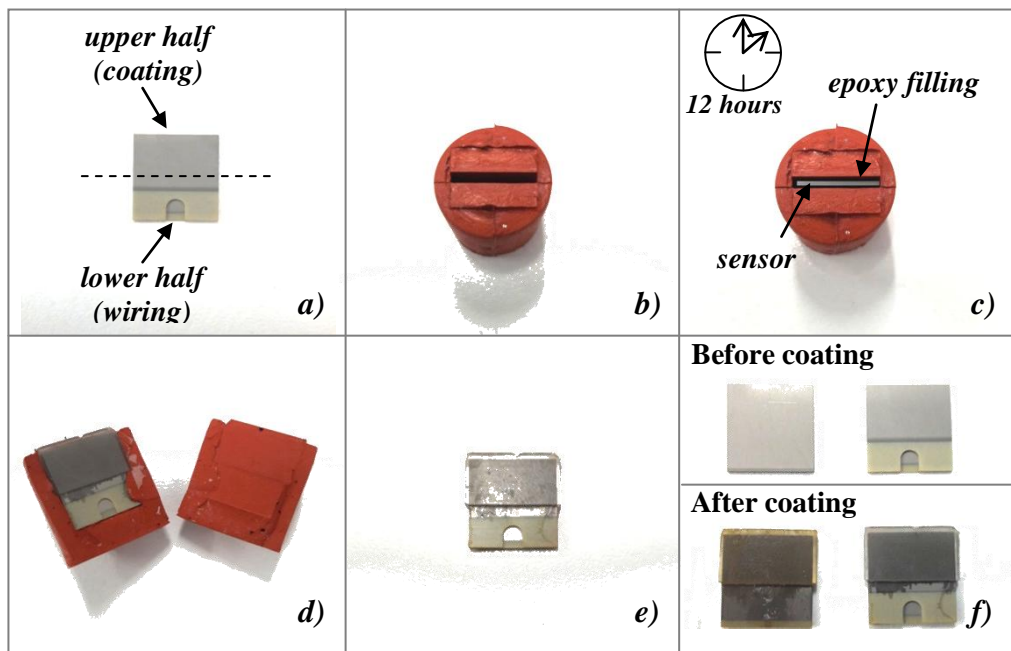
Figure A-4: Coating procedure with epoxy resin

7.5. BE WIRING AND SHIELDING/GROUNDING

After coating, both series and parallel BE had to be wired to a function generator and an oscilloscope in order to transmit (parallel BE, used as a source) and receive (series BE, used as a receiver) electrical signals. In order to minimise the electrical noise and, therefore, be able to detect the weak signal carried by the BE, a coaxial cable (RG174) was used to connect the sensors to the function generator and the oscilloscope. The wiring procedure differs for the series BE and the parallel BE. Also, for the series BE, an

additional grounding procedure and a re-coating stage have to be carried out before the insertion of the sensor into the PLA casings.

- **Wiring of the parallel (source) BE**

Parallel BE are purposely manufactured to allow the correct wiring procedure. In this case, both the metal shim (inner layer of the piezoelectric element) and the electrodes (outer front and back layers of the piezoelectric element) of the BE have to be soldered to the coaxial cable. Figure A-5 shows the steps followed for the wiring procedure of the parallel sensor. First of all, the outer jacket of the coaxial cable was cut to expose its inner components (metal shield, insulating layer and copper conductor). About 3 mm of the insulating layer were trimmed with the aid of a wire stripper in order to expose the inner conductor, while the surrounding metal shield was divided in two parts and twisted (Figure A-5a). Beforing soldering, the coaxial calble was put through the PLA casing and the corresponding o-ring (Figure A-5b), and through the designated groove in the triaxial cell pedestal.

Figure A-5c shows the areas intended for the electrical wiring of a parallel BE. At the front, a small portion of the inner metal shim is conveniently exposed in order to allow soldering it to the copper conductor of the coaxial cable, while the remaining non-coated outer surface (electrode) is meant to be soldered to the shield. At the back, the whole non-coated surface is suitable for soldering to the second portion of the shield.

A soldering iron and a lead-free (95.5/4.0/0.5-Sn/Ag/Cu) soldering wire were used for the electrical connection of the coaxial cable to the piezoelectric sensor. Before connecting the sensor to the cable, the tip of the conductor and the tip of the two portions of the shield were slightly covered with melted solder metal as well as the areas of the sensor intended

for soldering, this easing the wiring process. During soldering, a maximum temperature of 300 °C was adopted for melting the solder wire, in order to prevent depolarisation of the piezoelectric elements by approching their Curie temperature (320 – 350 °C). For the same reason, the soldering process was carried out as quickly as possible, with the tip of the soldering iron never touching the sensor's surface for more than a few seconds at a time. When soldering, the conductor and the shield were never let to get in contact to prevent short circuit. Figure A-5d shows a parallel BE after wiring.
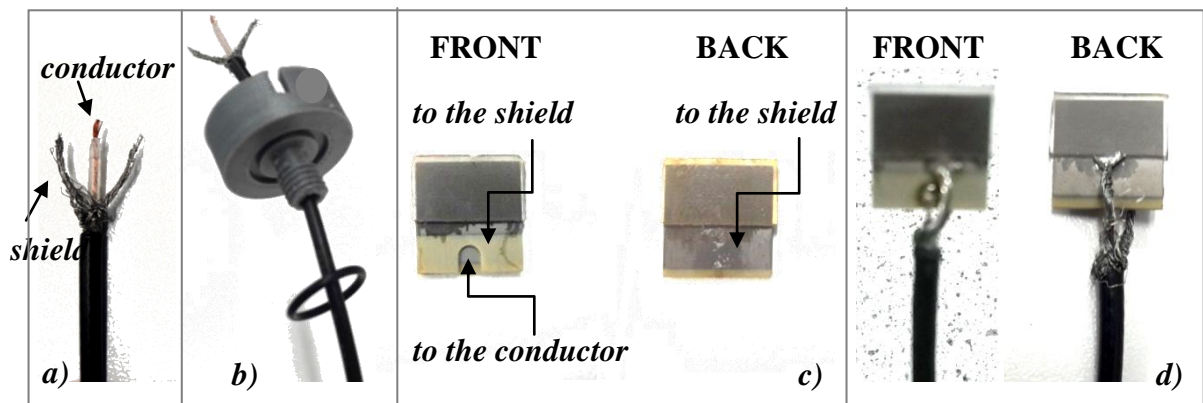
Figure A-5: Parallel BE wiring procedure

- **Wiring and shielding/grounding of the series (receiver) BE**

The wiring process of a series BE is slightly easier, as only the outer electrodes of the sensor have to be soldered to the coaxial cable. For this reason, the metal shim of the series BE is not exposed. Figure A-6 shows the wiring procedure for a series BE. After passing the coaxial cable through the PLA casing and o-ring (Figure A-6b) and through the top cap groove, the conductor and the shield of the coaxial cable could be soldered to the outer layers (electrodes) at the front and at the back of the sensor (Figure A-6c). The same soldering procedure for the parallel BE was carried out for the series BE.

After soldering, an additional step had to be perfomed in order to avoid undesired phenomena like cross-talk effect or excessive back-ground noise affecting the detection of

the BE electric signals. This was achieved by shielding and grounding the piezoelectric elements. The coated upper half of the sensor was covered with a thin layer of silver conductive paint, as well as the tip of the coaxial cable shield soldered to the sensor (Figure A-6d): in this way, any excess charges deposited on the surface of the sensor could migrate to the silver paint coating, where they couldn't produce any electric disturbance affecting the sensor (i.e. the silver paint acted a Faraday cage, shielding the sensor from electromagnetic interferences). Also, by extending the layer of paint to the shield, all the excess charges travelling towards the silver paint could be removed from the upper part of the sensor and tranferred to the shield of the coaxial cable, in turn connected to the ground.
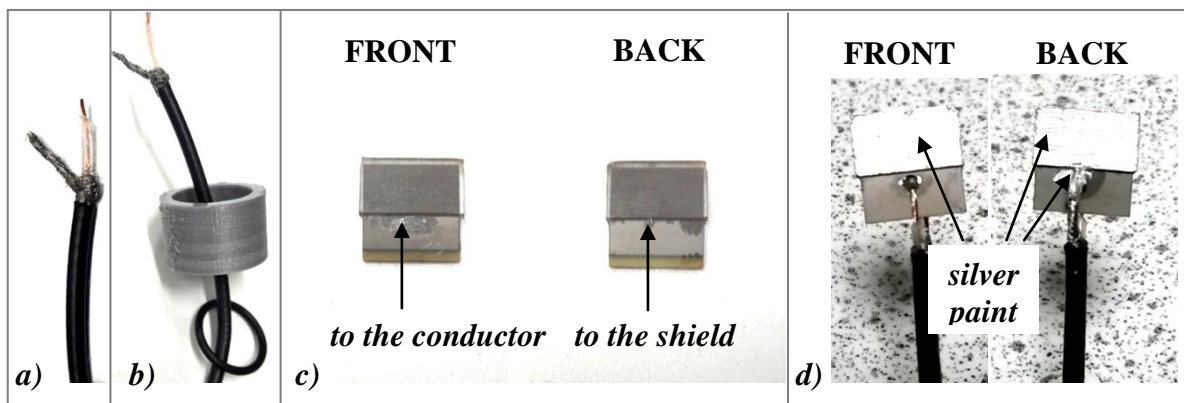
Figure A-6: Series BE wiring procedure

The shielding and grounding process had to be performed for the series BE only as parallel BE sensors are self-grounded.

After shielding and grounding, the upper half of the sensor, now covered with epoxy and silver paint, had to be re-coated with epoxy in order to water-proof its surface once again. This was achieved by simply brushing some liquid epoxy + curing agent mixture on the painted surface of the sensor. The last impermeable layer was made as thin as possible, in order to let the sensor free to bend and create an electric signal.

7.6.   BE INSERTION IN PLASTIC CASINGS AND EMBEDDING IN THE TOP CAP AND BASE PEDESTAL

The final step in the preparation of functional BEs, suitable for the measurement of shear wave velocities through soil specimens during triaxial tests, is the insertion of the wired and coated sensors into the 3D-printed PLA casings, which can then be fastened to the triaxial cell pedestal and top cap.

Figure A-7 shows the procedure carried out for the insertion of the sensor in the casing with the aid of the rubber mould previously casted and described in Section 1.2. The upper part of the sensor was inserted into the designated gap within the rubber mould, this preventing additional epoxy from reaching the coated half of the sensor (Figure A-7b – stage 1). The rubber mould was then filled with liquid epoxy, completely submerging the remaining portion of the BE and the soldered area (Figure A-7b – stage 2). At this stage, it was made sure once again that the conductor and the shield of the coaxial cable were not in contact, as this would certainly cause a short circuit.

The PLA casing was then pushed into the rubber mould (Figure A-7c). Excess epoxy displaced after the insertion of the casing filled the gap between the jacket of the coaxial cable and hole in the casing's thread, this providing a full water-proof protection to the whole electric system of the sensors. The liquid epoxy+curing agent mixture was left to cure for at least 12 hours.

Atfter curing, the hardened epoxy was able to hold in place the sensor into the PLA casing and to prevent the ingress of water, even under pressure. Finally, the casing was fastened to the pedestal (source BE, parallel) or top cap (receiver BE, series) of the triaxial cell, as shown in Figure A-7d.
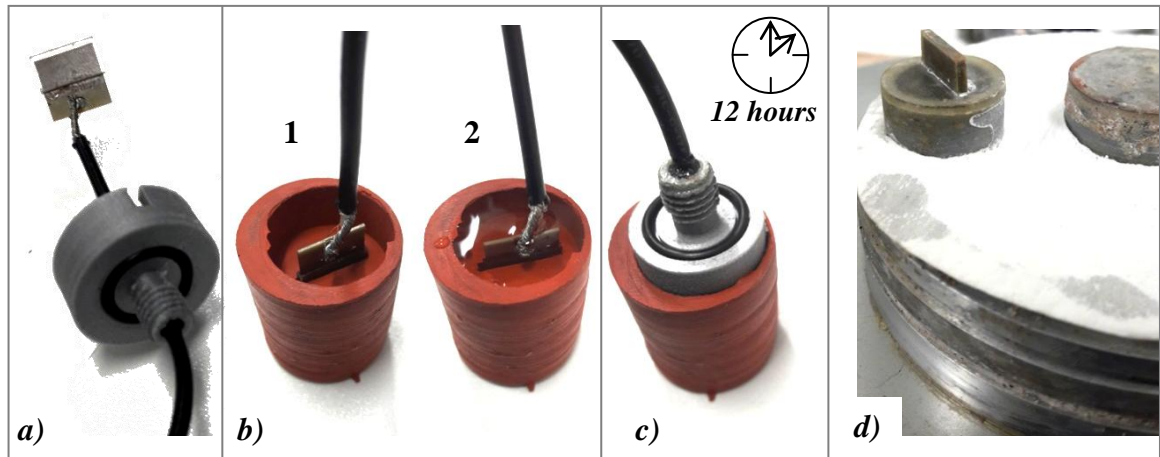
Figure A-7: BE insertion in PLA casings and embedding in the top cap/base pedestal

8. APPENDIX B – PRELIMINARY AND ADDITIONAL SIMULATIONS USING MERCURY DPM

8.1. CONTACT MODEL CHECK

The following simulations were performed using two spherical particles. Two opposite values of initial velocity were applied to the particles in order to observe the force and elastic energy response of the particles for a range of δ values, changing from negative to positive. The effect of the following parameters in the δ < 0 range was investigated:

- Repulsive/attractive stiffness k_{Coul} for Coulombian interaction;

- Threshold overlap (referred to as F_{range});

The term 'Repulsion' refers to the case where both particles are negatively (or positively) charged. The term 'Attraction' refers to the case where particles have opposite charges.

8.1.1. Effect of Coulombian stiffness

Seven cases were considered, namely No_charge (particles were not assigned a charge, i.e. their interaction was only mechanical), Repulsion k_10, k_20 and k_30 (both particles were assigned a positive charge, the same threshold overlap but different values of k_{Coul}), and Attraction k_10, k_20 and k_30 (particles were assigned opposite charges, the same threshold overlap but different values of k_{Coul}). The type of contact model selected for the analysis in MercuryDPM is reported in *Table B1*, together with the corresponding values of stiffness at the mechanical contact k, friction coefficient μ, maximum repulsive/attractive force at $\delta = 0$ $F_{Coul,max}$, and threshold overlap F_{range}. The value of k_{Coul} corresponding to each case can be derived as the ratio $F_{Coul,max}/F_{range}$.

	Contact Model (species)	k (δ>0)	mu	$F_{COUL,MAX}$ (at δ=0)	$F_{RANGE,COUL}$
No_charge	LinearViscoelasticFrictionSpecies	1E+06	1.0	-	-

Repulsion_k_10	LinearViscoelasticFrictionChargedBondedSpecies	1E+06	1.0	10.0	1.0
Repulsion_k_20	LinearViscoelasticFrictionChargedBondedSpecies	1E+06	1.0	20.0	1.0
Repulsion_k_30	LinearViscoelasticFrictionChargedBondedSpecies	1E+06	1.0	30.0	1.0
Attraction_k_10	LinearViscoelasticFrictionChargedBondedSpecies	1E+06	1.0	-10.0	1.0
Attraction_k_20	LinearViscoelasticFrictionChargedBondedSpecies	1E+06	1.0	-20.0	1.0
Attraction_k_30	LinearViscoelasticFrictionChargedBondedSpecies	1E+06	1.0	-30.0	1.0

Table B1. Selected input parameters in MercuryDPM for analysing the effect of k_{Coul}.

The effect of the Coulombian stiffness for attractive and repulsive particles in shown in *Figure B1* and *B2*. *Figure B1 a* and *b* show the constitutive relationship at the contact resulting from the selected input parameters for the case of attractive and repulsive particles. Higher Coulombian stiffness corresponds to higher repulsive (or attractive) force at the same overlap.

The effect of k_{Coul} on the elastic energy response for non-charged particles, attractive particles and repulsive particles is shown in *Figure B2 a* and *b*. As expected, the elastic energy developing in time between each pair of spheres is initially equal to zero for $\delta <$ F_{range}. After the threshold overlap is exceeded and particles are forced to get closer to each other, the elastic energy increases (repulsive particles) or decreases (attractive particles) non-linearly with time (while it remains equal to zero for non-charged particles), with an increasing rate with increasing k_{Coul}. The elastic energy curves experience a sudden and steep increase as soon as particles get in contact (collision, $\delta = 0$) and overlap ($\delta > 0$) for non-charged, attractive and repulsive particles. The repulsive force arising between each pair of particles after collision results in the decrease of elastic energy with time following the same path as before collision, corresponding to the movement of particles in opposite directions.

'Particle-scale mechanisms controlling the response of granular and clayey geomaterials at very small strains'
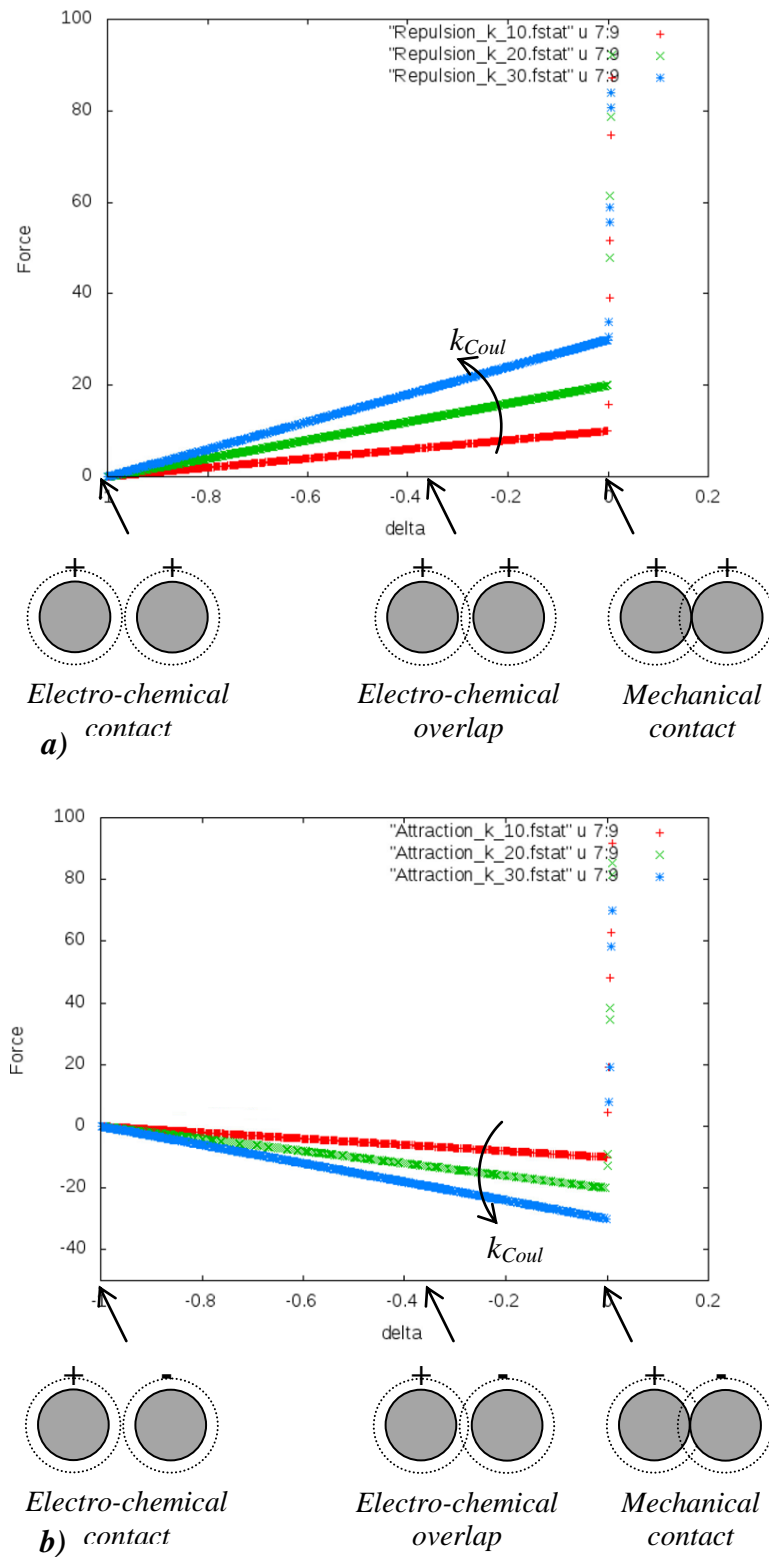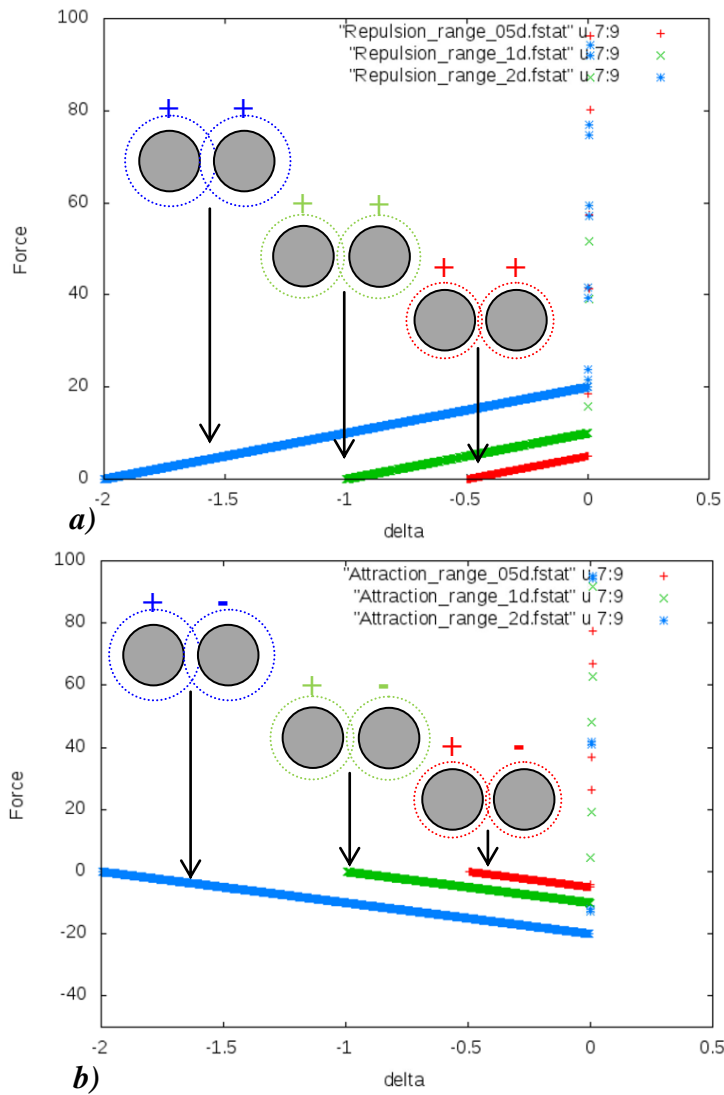

Figure B1. Constitutive relationship at the contact (contact law) for a) repulsive and b) attractive particles.
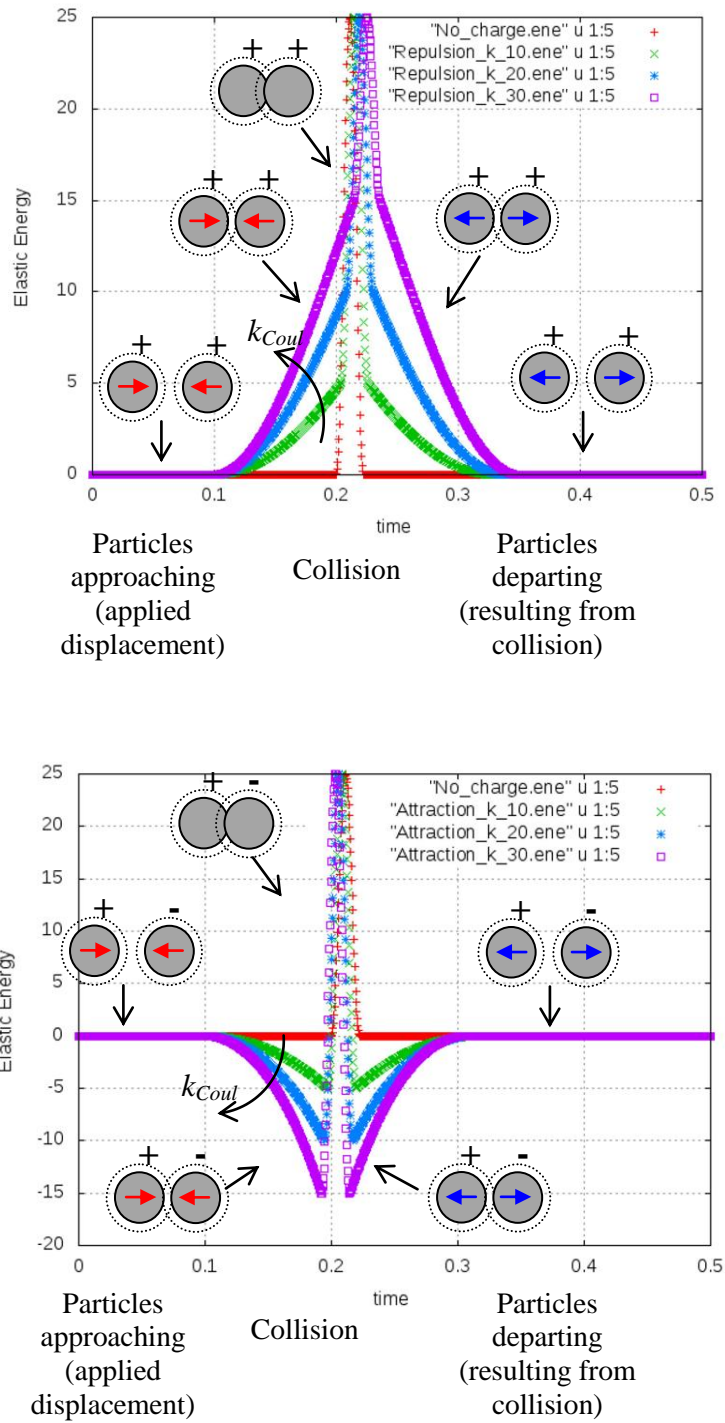
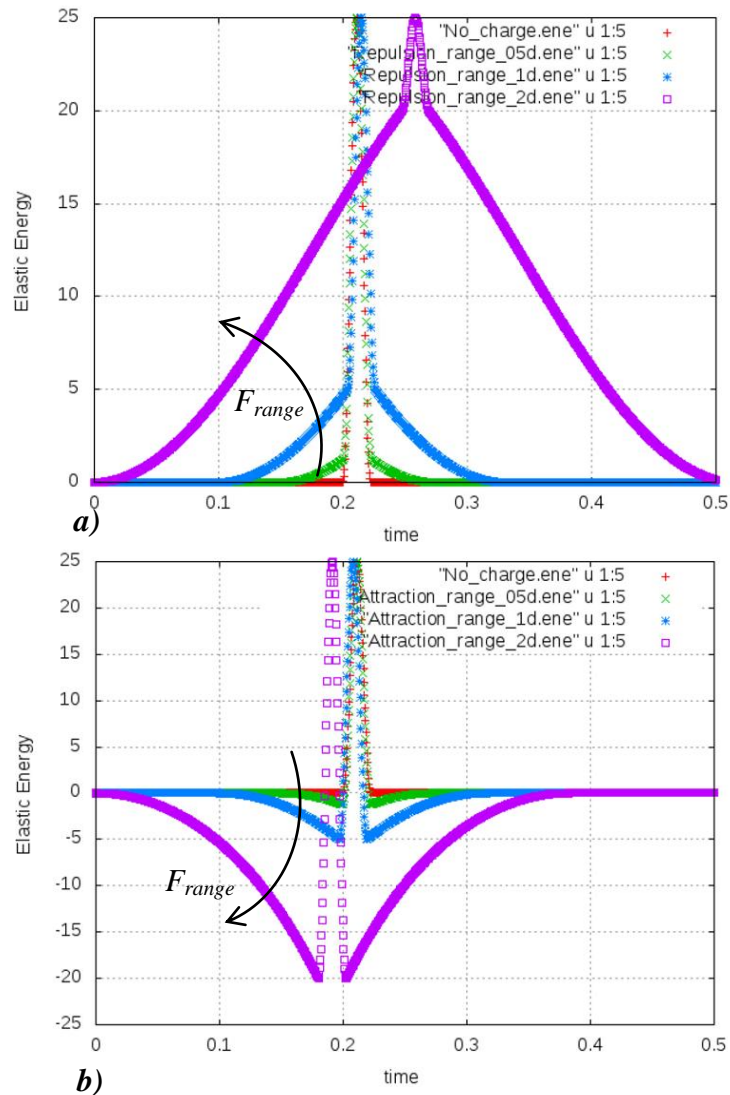Figure B2. Elastic energy versus time for a) repulsive and b) attractive particles.

8.1.2. **Effect of threshold overlap**

Another set of seven simulations were performed to explore the effect of the threshold overlap F_{range} on the elastic energy response of a system of two particles having the same Coulombian stiffness, k_{Coul}. The following cases were analysed (*Table B2*): non-charged particles (No_charge), repulsive particles with values of the threshold overlap equal to ½ of the radius, the radius and twice the radius (Repulsive_range_05d, Repulsive_range_1d, Repulsive_range_2d respectively), and attractive particles with values of the threshold overlap equal to ½ of the radius, the radius and twice the radius (Attractive_range_05d, Attractive_range_1d, Attractive_range_2d respectively).

	Contact Model (species)	k (δ>0)	mu	$F_{COUL,MAX}$ (at δ=0)	$F_{RANGE, COUL}$
No_charge	LinearViscoelasticFriction Species	1E+06	1.0	-	-

Repulsion_range_05d	LinearViscoelasticFriction ChargedBondedSpecies	1E+06	1.0	5.0	0.5
Repulsion_range_1d	LinearViscoelasticFriction ChargedBondedSpecies	1E+06	1.0	10.0	1.0
Repulsion_range_2d	LinearViscoelasticFriction ChargedBondedSpecies	1E+06	1.0	20.0	2.0
Attraction_range_05d	LinearViscoelasticFriction ChargedBondedSpecies	1E+06	1.0	-5.0	0.5
Attraction_range_1d	LinearViscoelasticFriction ChargedBondedSpecies	1E+06	1.0	-10.0	1.0
Attraction_range_2d	LinearViscoelasticFriction ChargedBondedSpecies	1E+06	1.0	-20.0	2.0

Table B2. Selected input parameters in MercuryDPM for analysing the effect of F_{range}.

The results are shown in *Figure B3* and *B4*. *Figure B3 a* and *b* show the constitutive relationship at the contact resulting from the selected input parameters. As a result of the

selected parameters, the slope of the constitutive relationships for the three pairs of repulsive particles and for the three pairs of attractive particles are equal, as the Coulombian stiffness values are equal.

Figure B4 a and *b* show the elastic energy versus time response for the case of repulsive and attractive particles. The qualitative evolution of the elastic energy is the same as the one observed in the previous case (*Figure B2 a* and *b*). However, the effect of the threshold overlap is clearly visible: the elastic energy starts to increase/decrease sooner in time for the case of particles with higher value of F_{range}, for both repulsive and attractive particles. The different responses are therefore shifted in time, as particles having a higher value of the threshold overlap will start interacting sooner than particles with lower values of the threshold overlap. It is also worth noticing that the time when the mechanical contact (collision) is achieved is significantly higher for repulsive particles with higher threshold overlap, and lower for attractive particles with higher threshold overlap. In the first case, this is due to fact that the repulsive electro-chemical force developing after the threshold overlap is exceeded is opposed to the applied initial velocity, causing the particles to slow down. In the second case, this is due to the fact that the attractive force developing after the threshold overlap is exceeded has the same sign as the applied initial velocity, causing the particles to speed up. The same effect (although less significant) could be noticed in Figure B2, as an effect of the different Coulombian stiffness rather than different threshold overlap.

It is also interesting to notice that, even if the Coulombian stiffness is the same for the three pairs of repulsive particles and the three pairs of attractive particles, the slope of the elastic energy curves is higher for particles with higher threshold overlap, as a result of the higher absolute value of force achieved for the same overlap.

It can therefore be concluded that the effect of 'stiffening' of the electro-chemical interaction can be simulated either by changing the slope of the contact law (constant F_{range}, variable k_{Coul}) or, similarly, by changing the threshold overlap for parallel contact laws (constant k_{Coul}, variable F_{range}).

Figure B3. Constitutive relationship at the contact (contact law) for a) repulsive and b) attractive particles.

Figure B4. Elastic energy versus time for a) repulsive and b) attractive particles.

8.2. ISOTROPIC COMPRESSION, RELAXATION AND 1D COMPRESSION OF SPHERICAL REPULSIVE PARTICLES

Following the contact model check, a number of preliminary simulations were performed using specimens of **400 repulsive spherical particles** (all negatively charged) in a 3D cubic domain with periodic boundaries, having different values of Coulombian stiffness. A specimen of 400 non-charged particles was also tested in order to compare the results.

Each simulation consisted in an initial isotropic compression, followed by a specimen relaxation (after a 'solid' condition is reached) and a 1D compression in the z-direction. The input parameters for each simulation are shown in *Table B3*.

	Contact Model (species)	k ($\delta>0$)	mu	$F_{COUL,MAX}$ (at $\delta=0$)	$F_{RANGE,COUL}$
Spheres_Preparation	LinearViscoelasticFriction Species	1E+06	0.3	-	-
Spheres_Preparation R2	LinearViscoelasticFriction ChargedBondedSpecies	1E+06	0.3	10.0	1.0
Spheres_Preparation R3	LinearViscoelasticFriction ChargedBondedSpecies	1E+06	0.3	100.0	1.0
Spheres_Preparation R4	LinearViscoelasticFriction ChargedBondedSpecies	1E+06	0.3	500.0	1.0

Table B3. Selected input parameters in MercuryDPM for four specimens of 400 particles.

8.2.1. Specimen homogeneity

In order to guarantee the homogeneity of the specimen, the simulations were performed using periodic boundaries rather than infinite walls. However, using the aforementioned boundary condition still led to localised aggregations of particles on three of the six boundaries. The simulations were hence performed using a constant strain rate during preparation. The effect of strain rate on the specimen preparation is shown in *Figure B5*.
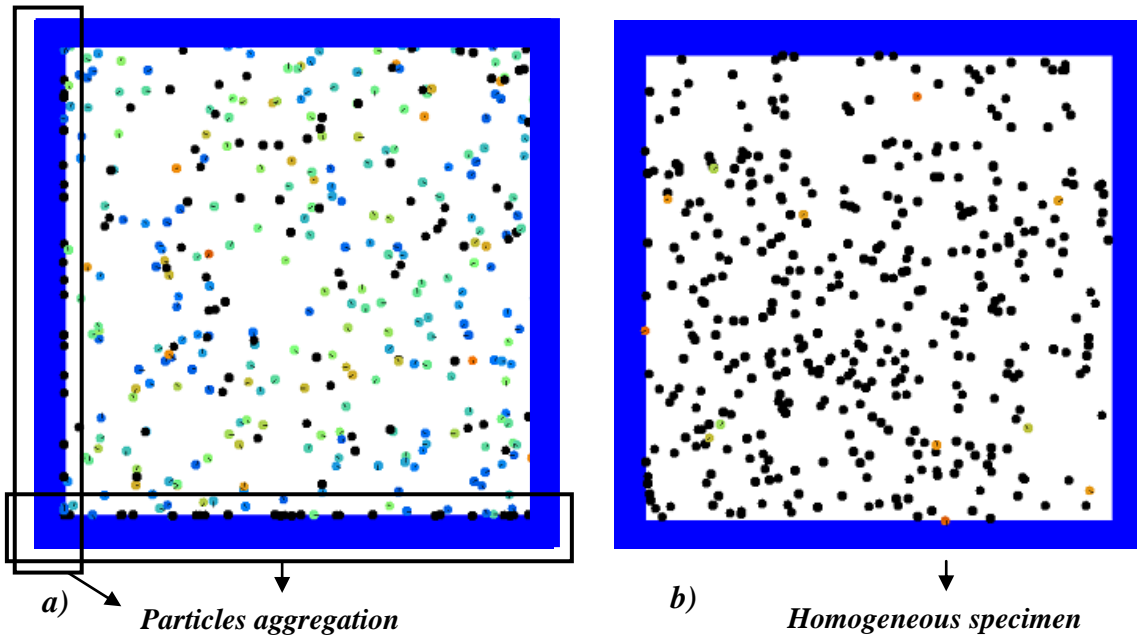
Figure B5. Specimen preparation. a) No strain rate, and b) With strain rate.

8.2.2. Identification of the gas/solid transition

The gas/solid transition can be easily identified for the case of non-charged particles by looking at the evolution in time of one or more macroscopic variables within the assembly. The most common approach for the identification of the gas/solid transition consists of monitoring the coordination number: once the coordination number exceeds a certain value (usually 5-6), the specimen can be considered as a 'solid' specimen. The same approach cannot be applied to the case of charged particles, as the gas/solid transition may be achieved before particles get in contact. Hence, a different criterion for the identification of the gas/solid transition has to be found.

When an aggregate of particles is in a gas state, although the elastic energy within the assembly might have reached a value greater than zero during the isotropic compression, its value decays as soon as the relaxation takes place, due to the instability of the contacts

created between particles. The specimen can be considered 'solid' when the elastic energy remains almost constant during relaxation, i.e. as soon as the specimen becomes able to bear an applied load.

Figure B6 shows the evolution of the elastic energy with time for the case of non-charged particles. The specimen was isotropically compressed up to different values of elastic energy before relaxation (corresponding to the different curves in *Figure B6 a*), and the behaviour of the specimen during free relaxation was observed. After a certain threshold, relaxation did not affect the elastic energy, due to the presence of stable contacts created between particles. Since it is advisable to be far enough from the gas/solid transition state before starting the proper test, a value of elastic energy equal to ≈16000 was chosen as gas/solid transition value, corresponding to a coordination number equal to ≈ 5.5 (*Figure B6 b*).
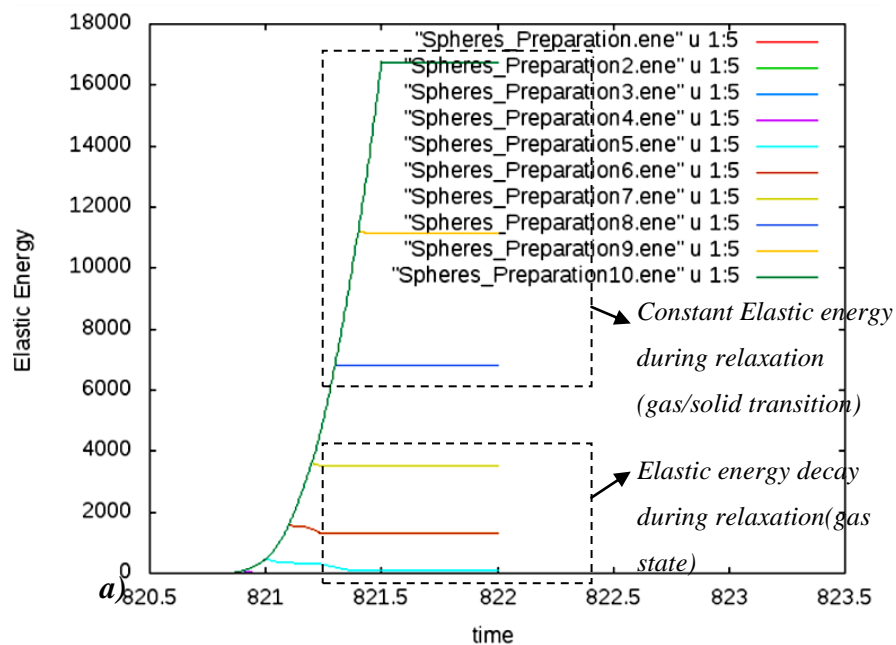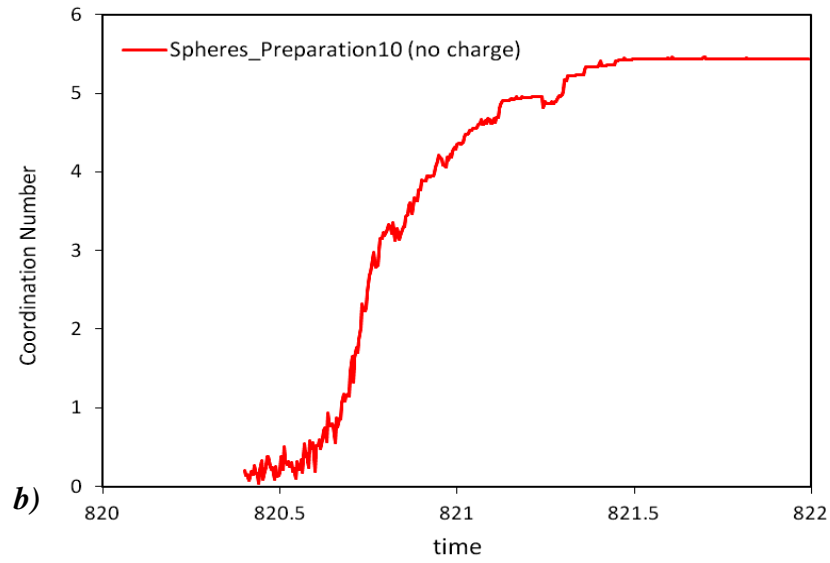
Figure B6. Gas-solid transition for non-charged particles: a) elastic energy, and b) coordination number versus time.

Figure B7 shows the coordination number versus time for both charged and non-charged particles. It is clear that the coordination number cannot be a distinctive value in the identification of the gas/solid transition state as its trend is not affected by k_{Coul} (the curves corresponding to different values of k_{Coul} are the same before relaxation). However, since the charged particles start to interact in the $\delta<0$ range, the solid condition for non-charged particles will surely correspond to a solid condition for charged particles. For this reason, the relaxation and 1D compression were started after an elastic energy target value of ≈16000 was reached, as shown in *Figure B8*.
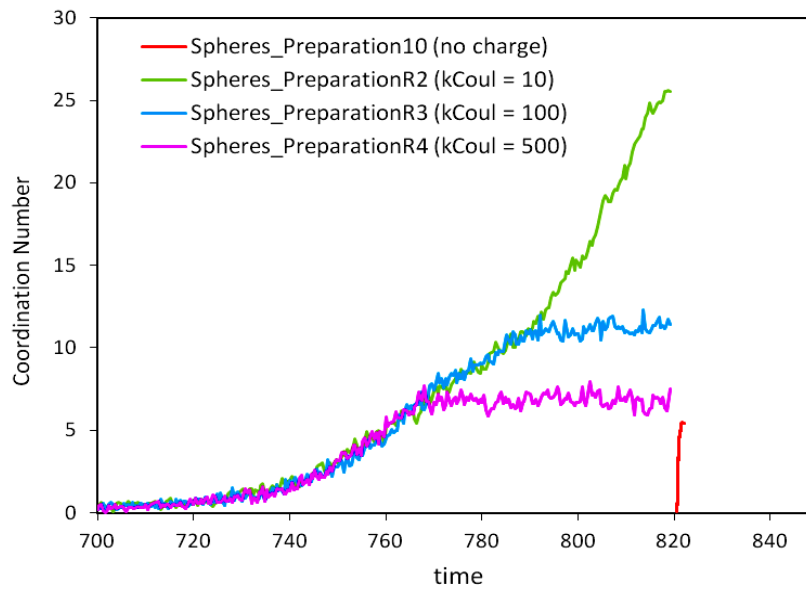
Figure B7. Evolution of the coordination number for charged and non-charged particles.
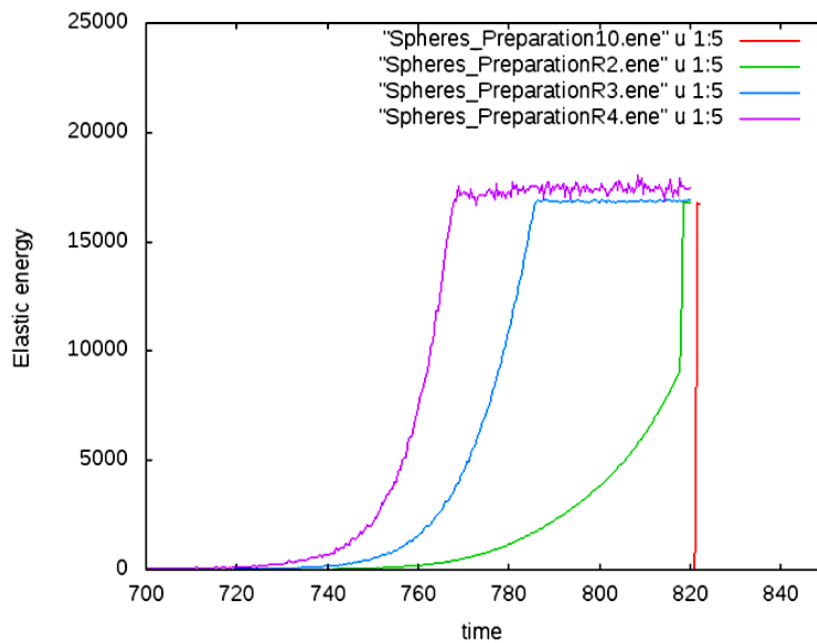
Figure B8. Elastic energy for charged and non-charged particles during preparation and relaxation.

8.2.3. **1D compression**

A 1D compression in the z-direction was performed after relaxation. As expected, there is a clear difference in the elastic energy response, depending on the magnitude of k_{Coul}. In the void ratio versus elastic energy graph (*Figure B9*), it is clear how the extent of the repulsion affects both the sample configuration and the energetic response during the 1D compression.
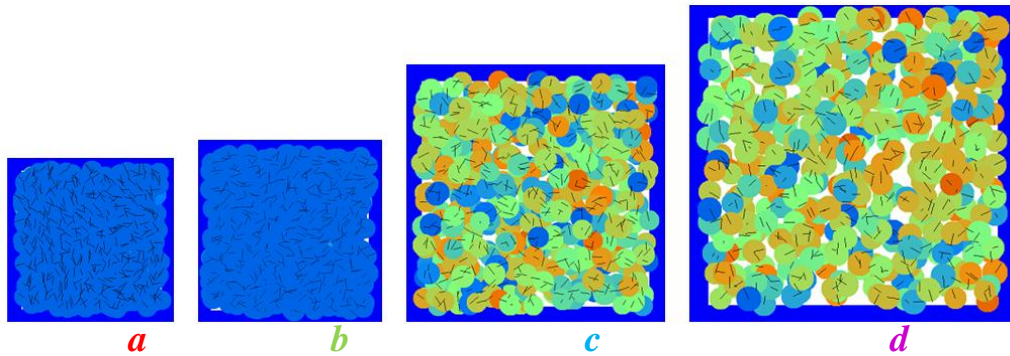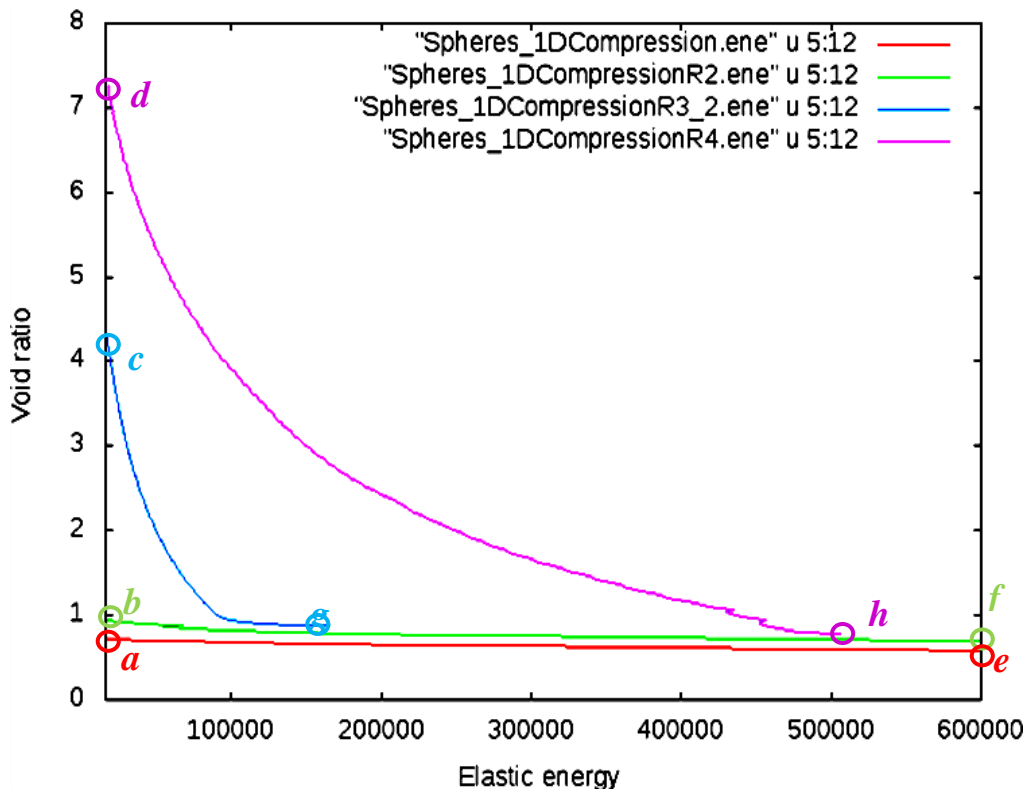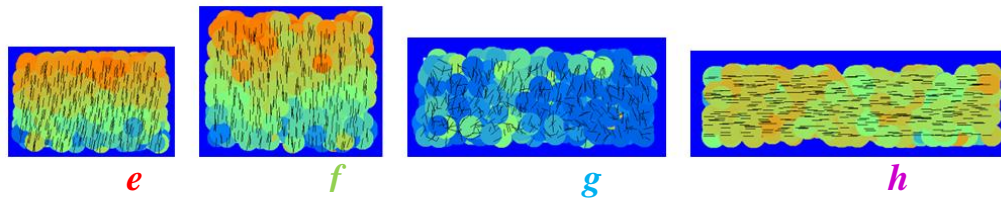
Figure B9. Void ratio versus elastic energy and specimen configurations during 1D compression.

8.3.   SENSITIVITY ANALYSES

Once the response of single spherical particles and aggregates of spherical particles was explored, a number of simulations were performed on rod-shaped particles (as extensively described in **Chapter 3**). The simulations presented in **Chapter 3** followed a number of additional simulations performed on similar specimens of rod-shaped particles, aimed at analysing the effect of different model parameters on the one dimensional compression response of the virtual specimens. In the following sections, the sensitivity analyses carried out prior to the final simulations are presented.

8.3.1. Effect of friction coefficient

Although the friction coefficient has been kept constant in the simulations presented in **Chapter 3**, its value has a significant effect on the compression behaviour of the virtual specimens.

Figure B10 shows the results of different simulations performed on virtual specimens having the same values of k, k_{Coul} and F_{range}, but different values of friction coefficient μ. The friction coefficient has a significant effect on the slope of the compression curve: the higher the friction coefficient, the lower the compressibility of the virtual specimen. It can be noticed that for very high values of μ (i.e. $\mu=100$), the response of the specimen

becomes non-monotonic. Sudden discontinuities in the compression curve are visible upon loading resulting from the fact that, after the shear resistance at the contacts is exceeded for a certain value of vertical stress, the whole configuration becomes unstable and particles re-arrange towards new equilibrium configurations characterised by the same void ratio, but lower vertical stress.

This is the reason why, although the response of the virtual specimens with high values of μ appears to be much closer to the response of the specimens tested experimentally at a quantitative level, a low, conventional value of μ was selected (μ=0.3) in the analyses presented in **Chapter 3**.

- k_{Coul}=**400, F_{range} = r =0.5, F_{max} =200**
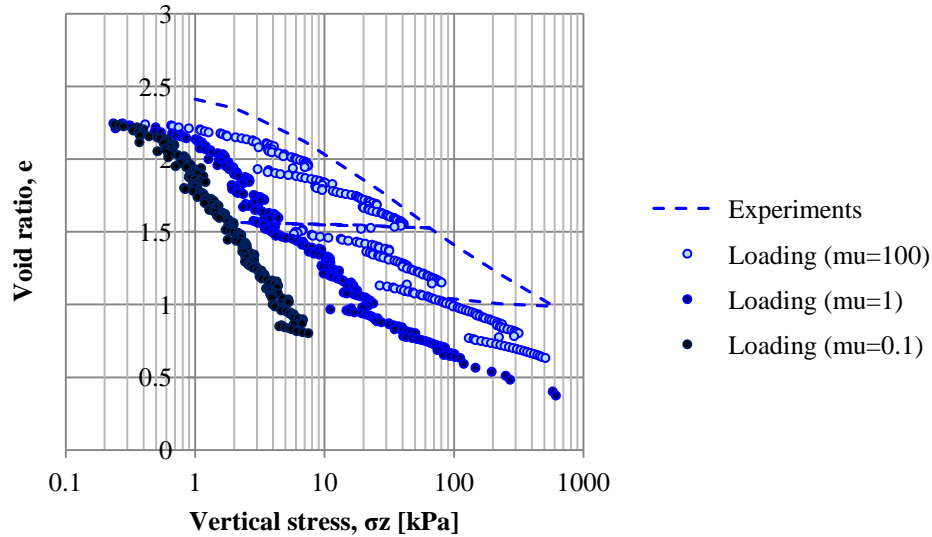
Figure B10. Effect of friction coefficient μ during 1D compression.

8.3.2. Effect of force range (threshold overlap)

Although the threshold overlap in the simulations presented in **Chapter 3** was kept constant for different values of pH and dielectric permittivity, a number of additional simulations were carried out by changing the value of the threshold overlap. Different combinations can be attempted in order to assess the effect of the threshold overlap on the compressibility of the virtual specimens, i.e. by changing k_{Coul} while keeping F_{max} constant, or by changing F_{max} while keeping k_{Coul} constant. The two combinations have been explored in additional simulations, whose results are presented hereafter.

Changing k_{Coul}, constant F_{max}

The effect of changing k_{Coul} while keeping a constant F_{max} is not clear. There isn't a consistent trend in the variation of the initial void ratio and of the compressibility of the specimen with the different threshold overlap values (*Figure B11 a, b, c, d*). However, a clear difference can be seen in the internal particle configurations (*Figure B11 e, f, g*): particles tend to keep a higher distance between each other for higher values of F_{range}.

- *a) k_{Coul}=400, μ =100, F_{range} =r=0.5, F_{max} =200*
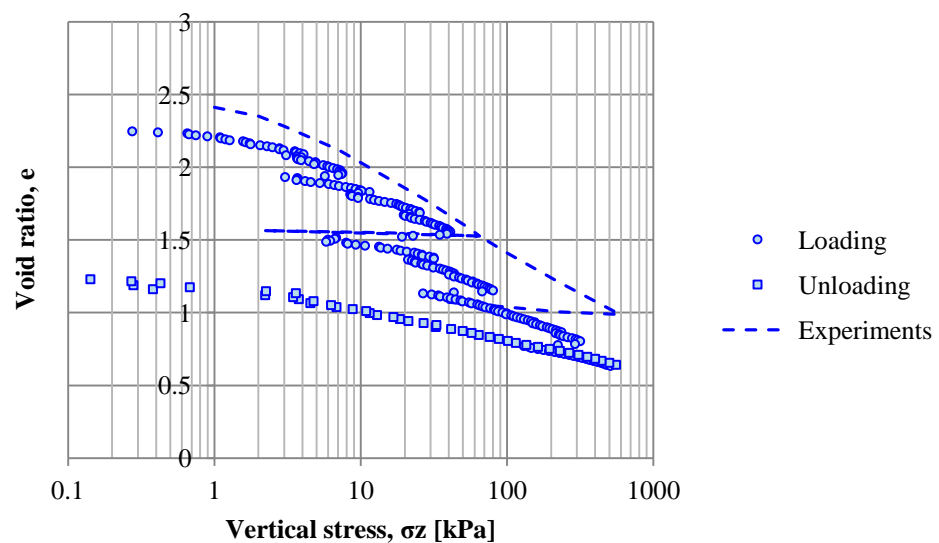
- *b) k_{Coul}=**200**, μ =100, F_{range} =**2r=1.0**, F_{max} =200*
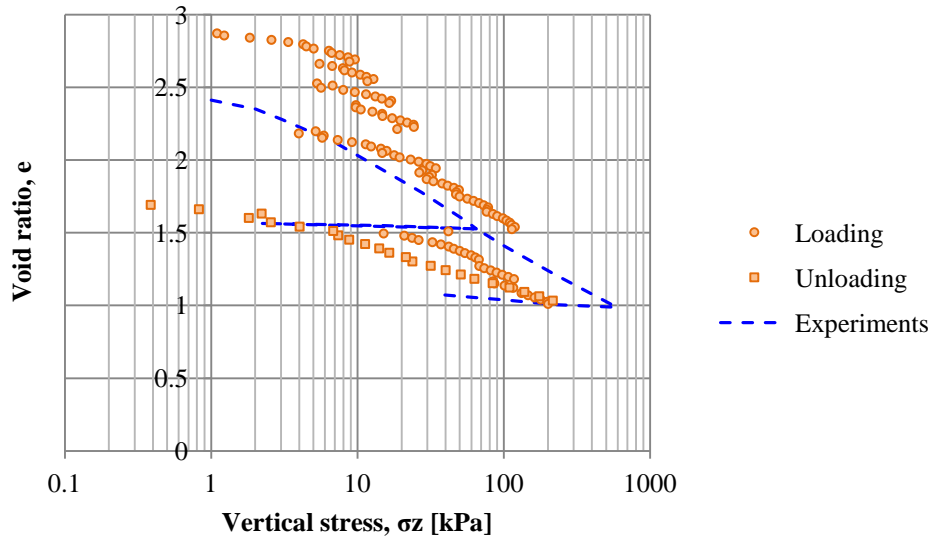
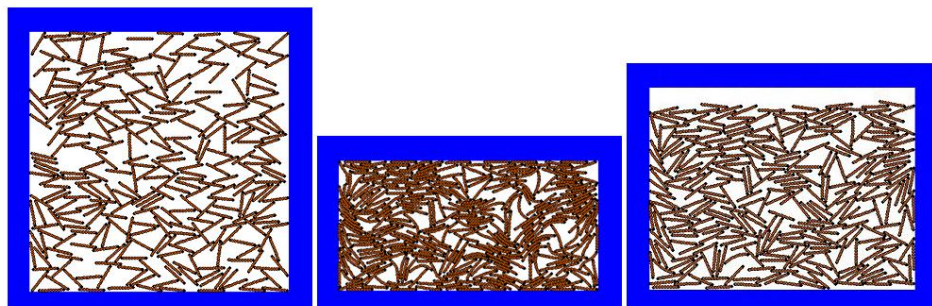- *c) k_{Coul}=**133.3**, μ =100, F_{range} =**3r=1.5**, F_{max} =200*
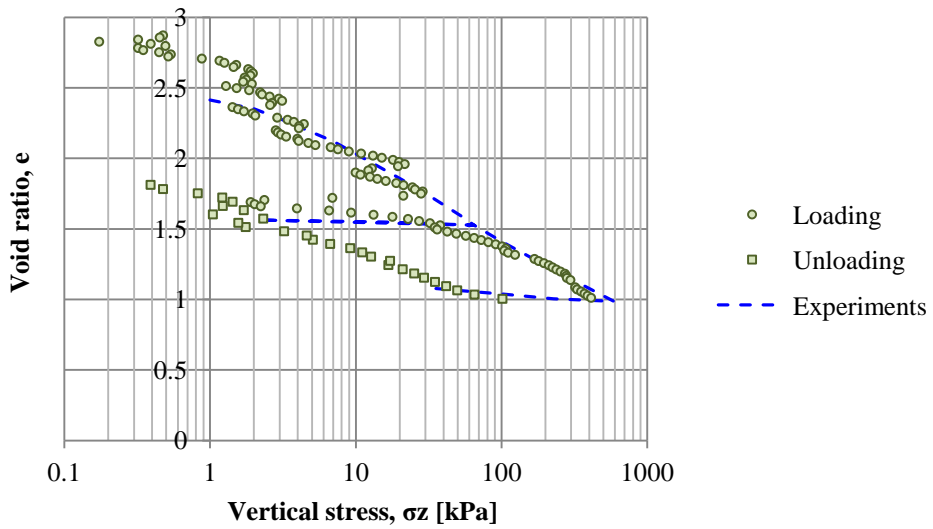
- *d) Comparison*

'Particle-scale mechanisms controlling the response of granular and clayey geomaterials at very small strains'
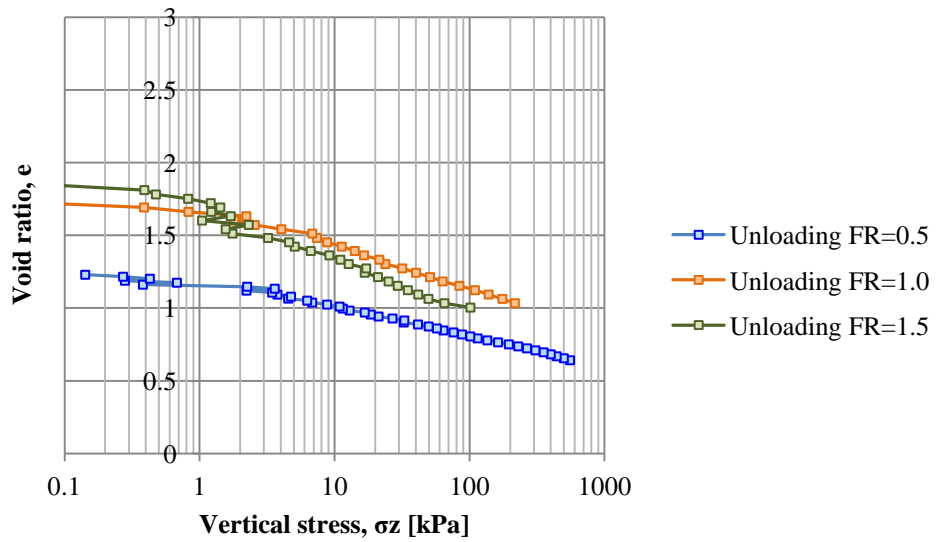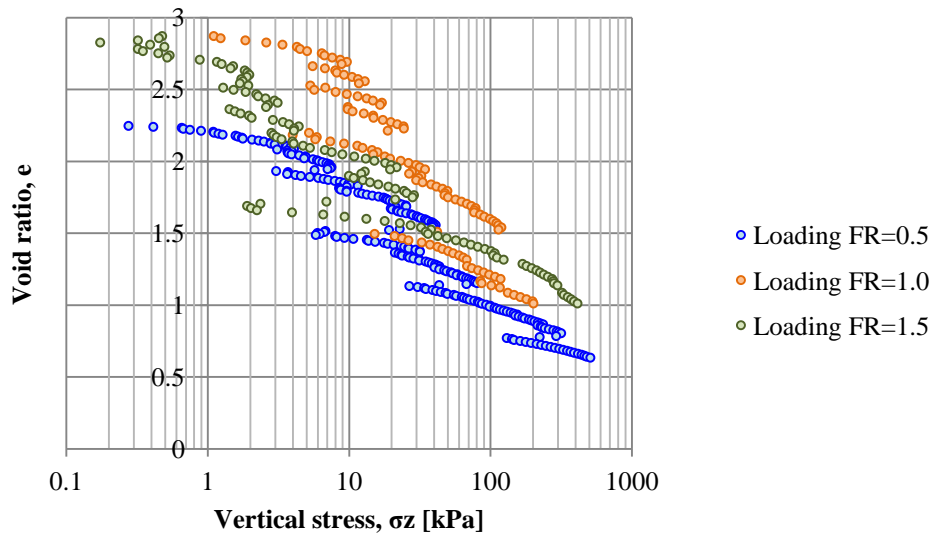
- Particle configurations
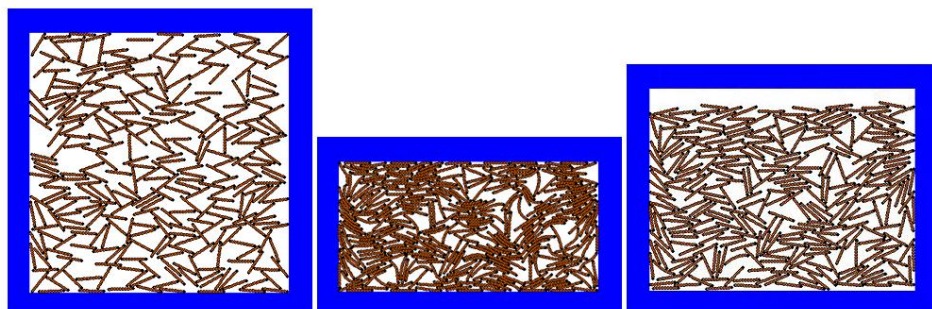
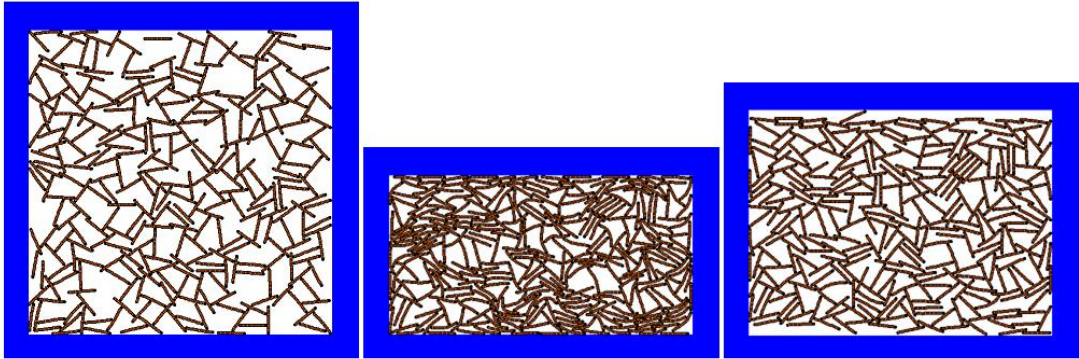*e) F_{range} =r=0.5 (Initial, Loading, Unloading)*

f) F_{range} =2r=1.0 (Initial, Loading, Unloading)
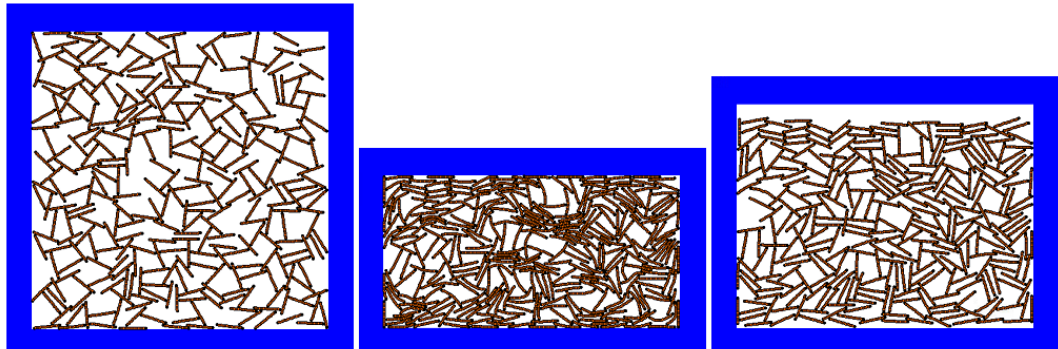
g) F_{range} =3r=1.5 (Initial, Loading, Unloading)
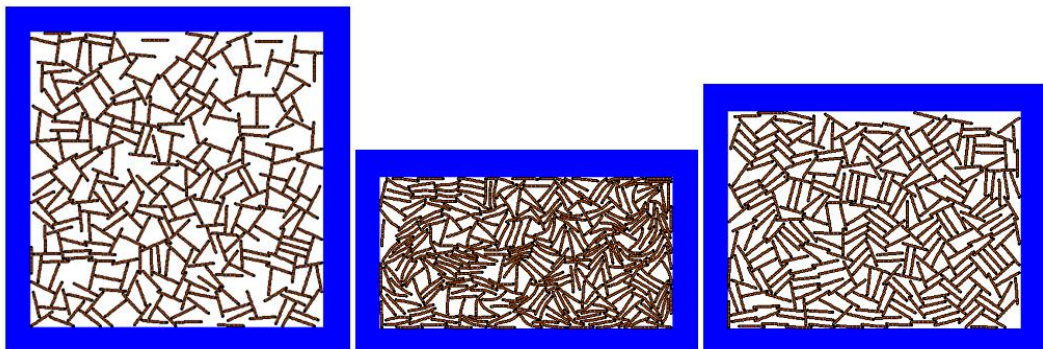
Figure B11. Effect of F_{range} during 1D compression and unloading (changing F_{max})

Changing F_{max} ,constant k_{Coul}

As for the previous case, the effect of changing F_{max} while keeping a constant k_{Coul} is not clear. There isn't a consistent trend in the variation of the initial void ratio and of the compressibility of the specimen with the different threshold overlap values (*Figure B12 a, b, c, d*). However, a clear difference can be seen in the internal particle configurations

(*Figure B12 e, f, g*): particles tend to keep a higher distance between each other for higher values of F_{range}.

- *a) k_{Coul}=400, μ =100, F_{range} =r=0.5, F_{max} =200*
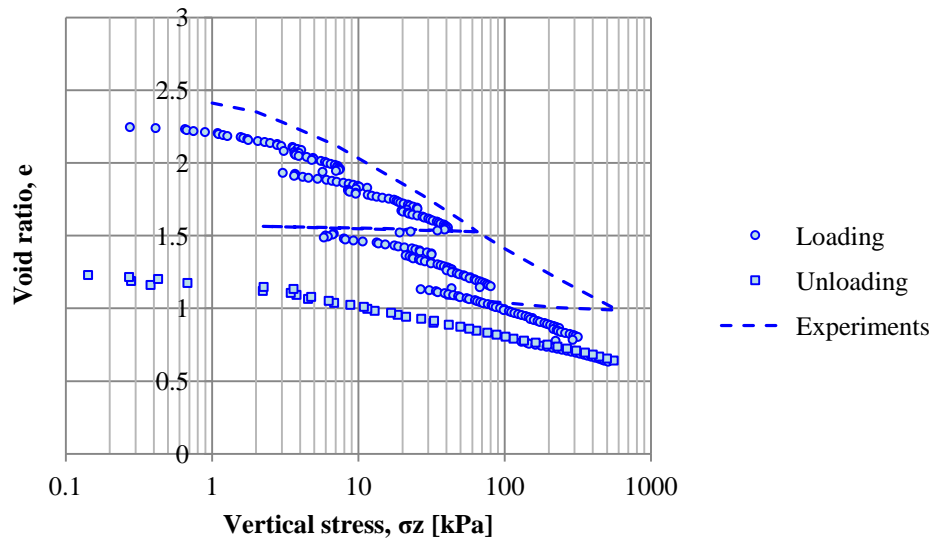
- *b) k_{Coul}=400, μ =100, F_{range} =2r=1.0, F_{max} =400*
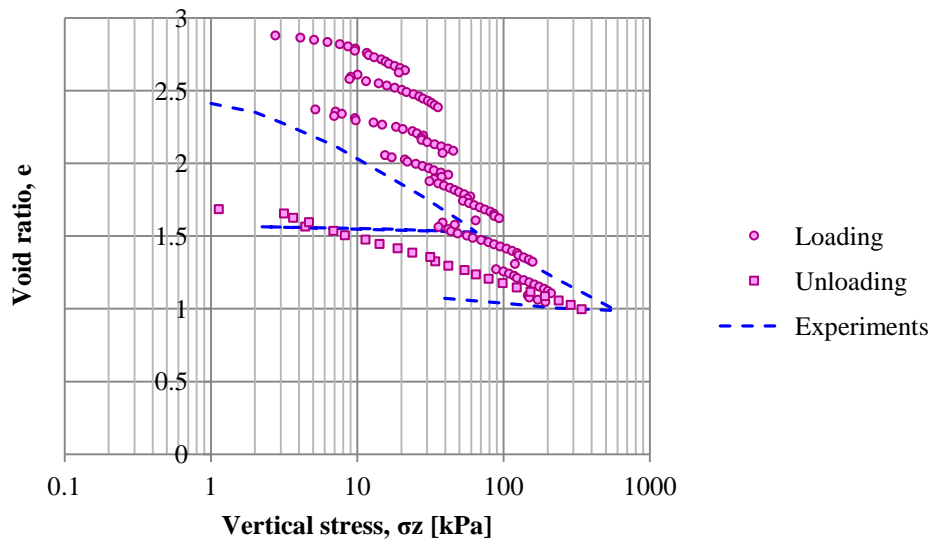
- *c) k_{Coul}=400, μ =100, F_{range} =3r=1.5, F_{max} =600*
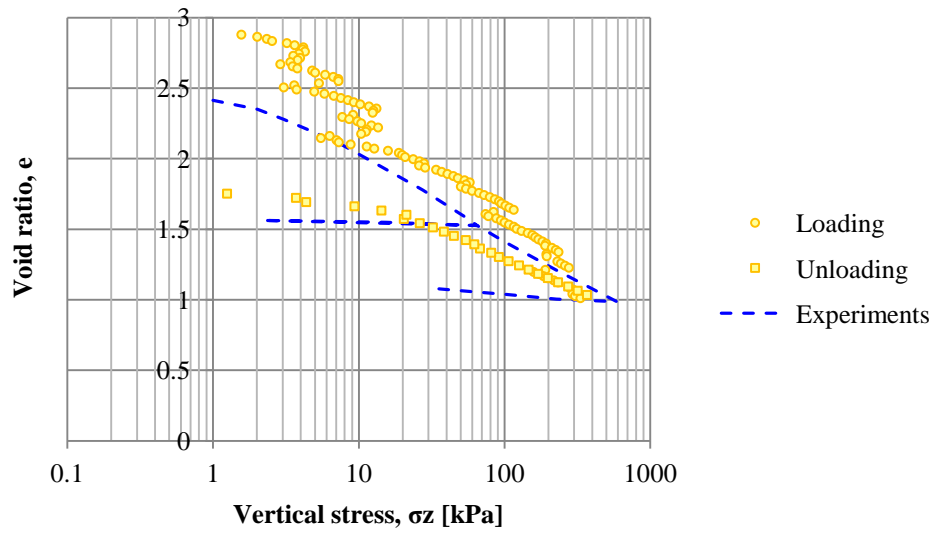
'Particle-scale mechanisms controlling the response of granular and clayey geomaterials at very small strains'

- *d) Comparison (Loading)*

- Particle configurations

e) F_range =r=0.5 (Initial, Loading, Unloading)

f) F_{range} =2r=1.0 (Initial, Loading, Unloading)

g) F_{range} =3r=1.5 (Initial, Loading, Unloading)

Figure B12. Effect of F_{range} during 1D compression and unloading (changing k_{Coul})

Effect of particle size distribution

An attempt was made to reproduce a polydisperse particle size distribution of the virtual specimen, in order to assess the effect of polydispersity on the compressibility behaviour. To this end, the results of simulations performed on a monodisperse specimen and a polydisperse specimen (Fuller-type particle size distribution) with the same contact law parameters were compared. Although the slope of the compression curves seems to be unaffected by the presence of particles with different sizes within the specimen,

polydispersity appears to reduce the 'jumps' in the void ratio-versus-vertical stress plot. This is probably due to the fact that, when an instability within the specimen is created after the shear resistance at the contacts is exceeded, the vertical stress does not jump back to small values as the small particles filling the voids between larger particles offer an additional resistance.

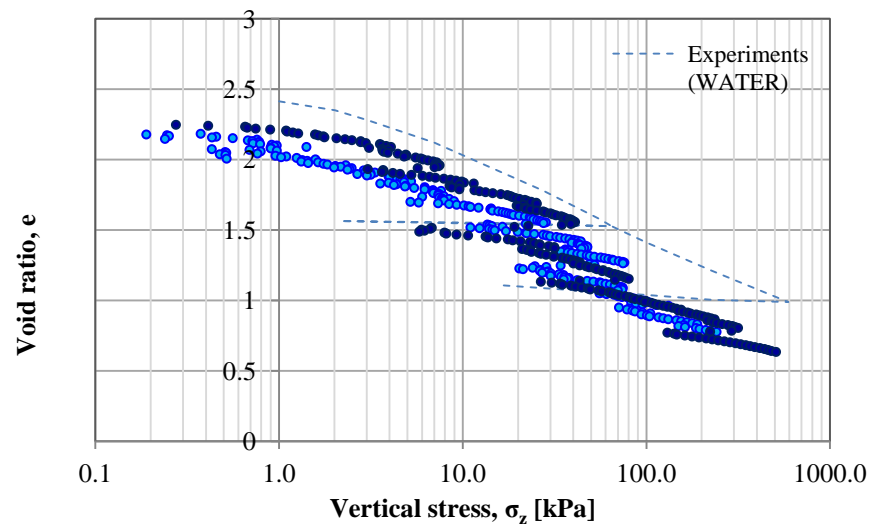- *a) k_{Coul}=100, μ =100, F_{range} =r, **monodisperse***
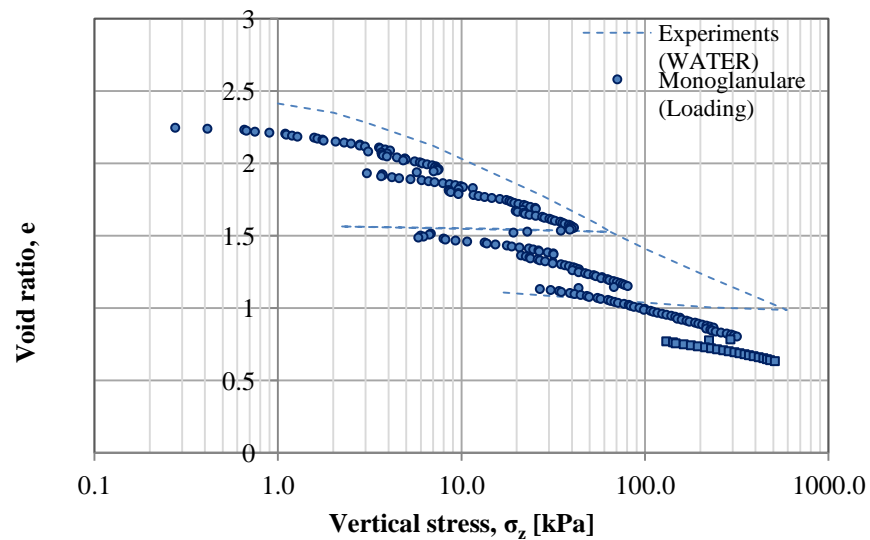
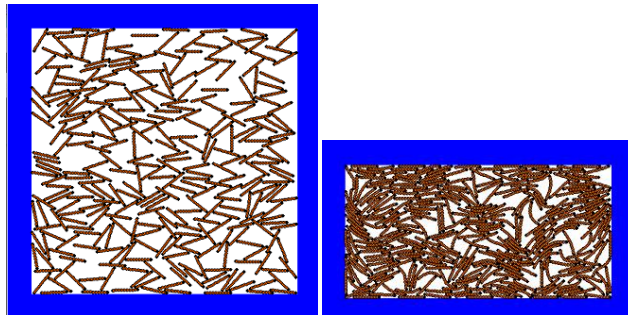- *b) k_{Coul}=100, mu=100, F_{range} =r, **polydisperse (Fuller PSD)***
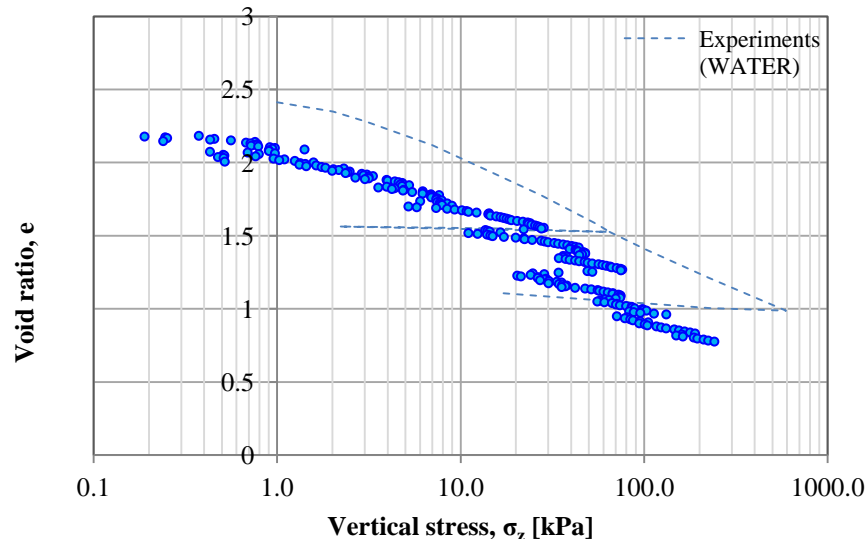
- *c) Comparison **monodisperse/Fuller PSD** (loading)*

'Particle-scale mechanisms controlling the response of granular and clayey geomaterials at very small strains'

- Particle configurations

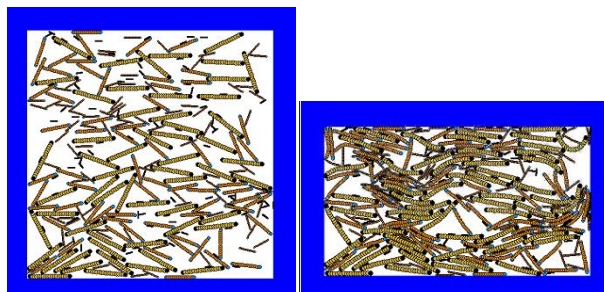*d) MONODISPERSE*

e) FULLER PSD

Figure B13. Effect of polydispersity during 1D compression

'Particle-scale mechanisms controlling the response of granular and clayey geomaterials at very small strains'